# Inference of Stratospheric Temperature and Water Vapor Structure from Limb Radiance Profiles

By

Thomas B. McKee

Department of Atmospheric Science
Colorado State University
Fort Collins, Colorado

Colorado State University

Department of Atmospheric Science

Paper No. 178

# INFERENCE OF STRATOSPHERIC TEMPERATURE AND WATER VAPOR STRUCTURE FROM LIMB RADIANCE PROFILES

by

Thomas B. McKee

This report was prepared with support from
The National Science Foundation
Grant No. GA-18783 and
The Air Force Cambridge Research Laboratories
Contract F-19628-70-C-0035

Project Leader: Stephen K. Cox

Department of Atmospheric Science
Colorado State University
Fort Collins, Colorado

February 1972

Atmospheric Science Paper No. 178

ABSTRACT OF DISSERTATION

INFERENCE OF STRATOSPHERIC TEMPERATURE AND WATER VAPOR STRUCTURE FROM LIMB RADIANCE PROFILES

Techniques to infer stratospheric temperature and water vapor mixing ratio structure as a function of pressure from a satellite using limb radiance profiles are presented. The techniques have eliminated the need for precise pointing information and require only the easily obtained vertical scan rate. Example radiance profiles were calculated for the 615 $cm^{-1}$ to 715 $cm^{-1}$ spectral interval of carbon dioxide and the 205 $cm^{-1}$ to 295 $cm^{-1}$ spectral interval of water vapor. The sensitivity of inferred temperature and water vapor structure to realistic values of scale, bias, and random radiance errors are shown and found not to be excessive.

The propagation of errors due to horizontal temperature gradients and random radiance errors through temperature inference and hydrostatic integration into calculations of geostrophic wind and wind shear were investigated for a stratospheric structure typical of winter with a large low pressure system centered at the north pole. The horizontal temperature gradients produced temperature errors up to about 4° K for a gradient of 1.1 °K $deg.^{-1}$ and increased the lapse rate between 10mb and 5mb. Resulting errors in the wind field were less than 10 per cent of the wind; wind

ACKNOWLEDGEMENTS

The author wishes to express his sincere thanks to Dr. Stephen Cox for his counsel and encouragement during this research effort. Dr. William Marlatt's advice during the early phases of the research is appreciated. Thanks also to the members of the doctoral committee for their interest and criticism in my continuing education. A special note of appreciation to my wife, Lee, for her steadfast encouragement through the years of study.

This research was supported in part by the National Science Foundation under Grant GA-18783 and the Air Force Cambridge Research Laboratories under Contract Number F-19628-70-C-0035.

Dr. Russell Walker of the Air Force Cambridge Research Laboratories kindly provided his experimental radiance profiles which allowed the examples in Chapter IV. Mr. Richard Davis of the National Aeronautics and Space Administration contributed the theoretical radiances used for the horizontal temperature gradient analysis in Appendix B.

TABLE OF CONTENTS

LIST OF TABLES

LIST OF FIGURES

LIST OF FIGURES--Continued

## LIST OF SYMBOLS

| | |
|---|---|
| $A_1$ | constant in transmittance curve fit |
| $A_2$ | constant in transmittance curve fit |
| $B_1$ | constant in transmittance curve fit |
| $B_2$ | constant in transmittance curve fit |
| $C_o$ | constant in transmittance curve fit |
| $C_1$ | constant in transmittance curve fit |
| $C_2$ | constant in transmittance curve fit |
| $C_3$ | constant in transmittance curve fit |
| $D_1$ | first radiation constant, erg $cm^2$ $sec^{-1}$ $sr^{-1}$ |
| $D_2$ | second radiation constant, cm°K |
| f | Coriolus term, $sec^{-1}$ |
| $J_\nu$ | source function, W $m^{-2}$ $sr^{-1}$ cm |
| $k_\nu$ | spectral absorption coefficient, cm |
| m | molecular weight, gm $mole^{-1}$ |
| N | radiance, W $m^{-2}$ $sr^{-1}$ cm |
| $N_\nu$ | spectral radiance, W $m^{-2}$ $sr^{-1}$ cm |
| $N_{B_\nu}$ | spectral radiance from a black body, W $m^{-2}$ $sr^{-1}$ cm |
| p | pressure, mb |
| $p_e$ | effective pressure (eq. 2.3), mb |
| p | tangent pressure, mb |
| r | radius of earth, km |
| R | gas constant of air, erg $gm^{-1}$ $°K^{-1}$ |
| s | distance along line of sight, km |

| | |
|---|---|
| $T$ | temperature, °K |
| $T_e$ | effective temperature (eq. A.3), °K |
| $u$ | optical depth, cm |
| $u^*$ | reduced optical depth, cm |
| $w$ | mixing ratio, n.d. |
| $x$ | natural logarithm of the product of optical depth and effective pressure, n.d. |
| $y$ | north-south distance, cm |
| $z$ | altitude, km |
| $Z$ | tangent height, km |
| $\alpha$ | half width, $cm^{-1}$ |
| $\alpha_D$ | Doppler half width, $cm^{-1}$ |
| $\gamma$ | lapse rate, $Kkm^{-1}$ |
| $\delta$ | small spectral interval, $cm^{-1}$ |
| $\Delta$ | finite difference |
| $\theta$ | nadir, angle, deg. |
| $\nu$ | wave number, $cm^{-1}$ |
| $\bar{\nu}$ | line center, $cm^{-1}$ |
| $\rho$ | density, gm $cm^{-3}$ |
| $\tau$ | transmittance, n.d. |
| $\tau_\nu$ | spectral transmittance, n.d. |
| $\phi$ | latitude, deg. |
| $\Phi$ | relative spectral response, n.d. |
| $\Omega$ | angular velocity of earth, $sec^{-1}$ |

Subscripts

| | |
|---|---|
| a | average |
| c | carbon dioxide |
| h | water vapor |
| i, i-1 | arbitrary values |
| l | lower limit |
| m | measured |
| o | initial value |
| s | standard conditions |
| u | upper limit |
| 1,2,3,4, | points along line of sight |

# CHAPTER I

## INTRODUCTION

Man's activity on the earth's surface and in the atmosphere is requiring a greater knowledge of the upper atmosphere. Needs of the aerospace community have led to the description of several "standard" atmospheres (Environmental Science Services Administration, et al., 1966) incorporating variations with latitude and season. Balloonborne radiosondes are used extensively to measure temperature, pressure, and wind every twelve hours from a surface pressure near 1000 mb to pressures near 10 mb. The meteorological rocket network provides three times weekly but much more widely spaced measurement of temperature, height, and wind to higher altitudes with pressures of 1 mb or 0.1 mb. These measurement programs have permitted a gross description of the atmosphere above the tropopause which has resulted in an increased knowledge of the structure of the stratosphere.

A rather complete summary of stratospheric structure and circulation deduced from radiosonde and rocketsonde data has been given by Webb (1966) and Webb (1969). Large scale temperature structure is characterized by a tropical tropopause near 16 km to 17 km which is higher and colder than the tropopause near 8 km to 10 km in high latitudes. At

approximately 24 km the temperature gradient with latitude is very small and is a result of a near isothermal layer from 10 km to 24 km in extreme latitudes which is thinner toward the equator where temperature decreases up to 16 km or 17 km then increases above. Temperature generally increases with latitude from the tropopause up to 24 km which provides a negative wind shear with height through the thermal wind to reduce strong west winds at mid-latitudes and produce a minimum wind near the 24 km region. Above 30 km the temperature increases with height up to a maximum at the stratopause near 50 km or 1 mb. Temperature decreases toward the pole in the winter hemisphere yielding an increasing west wind with height which has a maximum at the stratopause. Winds of 80 m $sec^{-1}$ are not uncommon. In the summer hemisphere the temperature gradient weakens or even reverses to produce easterly winds. Sudden or explosive stratospheric warmings have been investigated since Sherhag (1952) first observed one. The complete three dimensional structure of a warming has not yet been observed due to limitations of the rocket network distribution. Numerical models have been used to simulate the stratosphere (Manabe and Hunt, 1968 and Clark, 1970) which indicate the energy for warmings originates in the troposphere. Smaller scale effects such as diurnal temperature changes are not as well known since rocket measurements of over 10° C change near 50 km (Beyers and Miers, 1965) do not agree with theoretical prediction of less than 5° C (Lindzen, 1967) as shown by Gille (1968).

The concentration and distribution of the trace constituents ozone and water vapor have been of considerable interest to scientists for many years. A review of the information available defining the distribution of these gases has been given by Reiter (1971). Ozone mixing ratio has been used as a conservative property of motion in the lower stratosphere for motion studies many times; consequently more is known about ozone concentrations than water vapor. Considerable doubt remained concerning the amount of water vapor in the stratosphere until recent years. Most mixing ratios deduced from radiation measurements indicate a dry stratosphere (Neporent et al., 1967, Kuhn and Cox, 1967, Murcray et al., 1969, and Pick and Houghtan, 1969), and more recent direct measurements of Sissenwine et al. (1968) and Mastenbrook (1968) agree. Mixing ratios of 2μg/g to 3μg/g are typical. Very little is known yet of seasonal variation around the world. The work of Sissenwine et al. (1968) indicates a seasonal trend with lowest mixing ratios in spring and highest mixing ratios in late summer at least at Chico, California. Latitudinal variations are not yet well established.

Further advances in the understanding of stratospheric phenomena would be hastened with a much wider base of observations. Observation of the earth's atmosphere from satellites offers a unique opportunity to monitor the atmosphere globally. Most progress to date has been made in the interpretation of thermal emissions from the gases in the

atmosphere. Calculation of the outgoing spectral radiance at the top of the atmosphere demands a knowledge of the vertical distribution of temperature, pressure, gas mixing ratio, and the absorption characteristics of the gas. The inverse problem of measuring the outgoing radiance in narrow spectral intervals, of assuming a mixing ratio of a gas, and of determining the vertical temperature structure has been ably attacked by Kaplan (1958), King (1963), King (1964), Wark and Fleming (1966), Twomey (1966), Smith (1967), Chahine (1968), and Rodgers (1970). All of the above have used carbon dioxide as the emitting gas and most the 15μ bands of $CO_2$. This work has led to the experiments on the Nimbus satellites and successful retrieval of temperature profiles as shown by Wark (1970).

The related problem of assuming a vertical temperature structure and infering the distribution of a radiatively active gas such as water vapor (Yamamoto and Tanaka, 1966, Conrath, 1969, and Smith, 1970) and ozone (Prabhakara et al., 1970, Russel, 1970) is more difficult since these gases have large changes in mixing ratio with height.

Theoretical methods used for the above work of temperature and gas inference have considered the atmosphere as plane parallel and have been intended primarily to probe the troposphere. The exceptions are the ozone inference and one experiment on Nimbus (Houghton, 1970) which probe the stratosphere while viewing in the nadir direction. Russell

(1970) also included a discussion of limb inference which is discussed next.

Another approach to probing the atmosphere with primary emphasis on the stratosphere is apparent. An instrument with a small optical field of view could scan across the limb of the earth. Such an instrument would instantaneously receive radiation from the atmosphere and from only a relatively narrow layer in height. Advantages of viewing the atmosphere tangentially are that large optical depths of gases at low pressures and small mixing ratios are available for emission and good vertical resolution is achievable. One disadvantage is that the spherical nature of the atmosphere must be accounted for. Calculations of limb radiance profiles have been reported by Kondratiev and Yakushevskaya (1963), Hanel et al. (1963), Wark et al. (1964), Bates et al. (1967), and Burn et al. (1967). Techniques have been developed to infer temperature (McKee et al., 1969a, House and Ohring, 1969 and Burn and Uplinger, 1970), water vapor mixing ratio (McKee et al., 1969b and House and Ohring, 1969), and ozone (Russell, 1970) from limb radiance scans. Unfortunately, all have assumed a precise knowledge of the exact angular orientation of the radiance measuring instrument relative to the solid earth. Measurement of such angular pointing is possible but prohibitively complex and costly.

This paper presents the development of theoretical techniques to infer stratospheric temperature and water vapor structure as a function of pressure from limb scan

radiance data without requiring precise pointing information. Temperature inference is developed for thermal emission from uniformly mixed carbon dioxide in the 15μ region. Water vapor inference is developed for the rotational band at wave lengths longer than 20μ. The technique for inferring temperature is applied to experimental radiance data and compared with available radiosonde and rocketsonde data. Propagation of errors due to horizontal temperature gradients and random radiance errors through the temperature inference and into calculated quantities such as height, geostrophic wind, and wind shear are discussed.

# CHAPTER II

## LIMB RADIANCE

Theoretical computations of limb radiance are made from the numerical evaluation of the integral form of the equation of radiative transfer. A derivation of the integral form of the transfer equation is presented and followed by a brief description of the numerical evaluation of the equation. Examples of limb radiance due to emission from carbon dioxide and water vapor are included.

The fundamental equation of radiative transfer usually referred to as the Schwartzchild equation is (Goody, 1964)

$$dN_\nu = -k_\nu \rho (J_\nu - N_\nu) ds \tag{2.1}$$

where the path, s, is measured positive in a direction opposite to the flow of radiation. The monochromatic transmittance of the gas is given by

$$\tau_\nu = e^{-\int k_\nu \rho ds} . \tag{2.2}$$

Consequently,

$$\frac{1}{\tau_\nu} \frac{\partial \tau_\nu}{\partial s} = -k_\nu \rho \; ; \tag{2.3}$$

thus the equation of transfer is written

$$\tau_\nu dN_\nu = (J_\nu - N_\nu) \frac{\partial \tau_\nu}{\partial s} ds \tag{2.4}$$

or

$$\tau_\nu dN_\nu + N_\nu \frac{\partial \tau_\nu}{\partial s} ds = J_\nu \frac{\partial \tau_\nu}{\partial s} ds \ . \qquad (2.5)$$

Transmittance is a unique single valued function along the path which provides

$$d\tau_\nu = \frac{\partial \tau_\nu}{\partial s} ds \ . \qquad (2.6)$$

Substitution of equation (2.6) into equation (2.5) produces

$$d(\tau_\nu N_\nu) = J_\nu \frac{\partial \tau_\nu}{\partial s} ds \ . \qquad (2.7)$$

Integration of equation (2.7) along the path from s=o to s=s gives the spectral radiance

$$N_\nu(o) = N_\nu(s)\tau_\nu(s) - \int_{s=o}^{s=s} J_\nu \frac{\partial \tau_\nu}{\partial s} ds \qquad (2.8)$$

since the value of $\tau_\nu$ at s=o is always unity. The radiance over a finite spectral interval is then

$$N = \int N_\nu(s)\tau_\nu(s) d\nu - \int\int_{\nu s} J_\nu \frac{\partial \tau_\nu}{\partial s} ds d\nu \ . \qquad (2.9)$$

Equation (2.9) is the integral form of the transfer equation and is composed of two terms. The first term is a boundary term of the radiance emitted at the boundary depleted by the transmittance through the gas. The second term is the contribution to the radiance from the gas along the path.

The geometry for which equation (2.9) must be evaluated for limb radiance is shown in Figure 2.1. The atmosphere is assumed to be spherically stratified. A line of sight from an observer through the atmosphere is uniquely specified by the altitude where the radius vector from the center of the earth forms a right angle with the line of sight. This

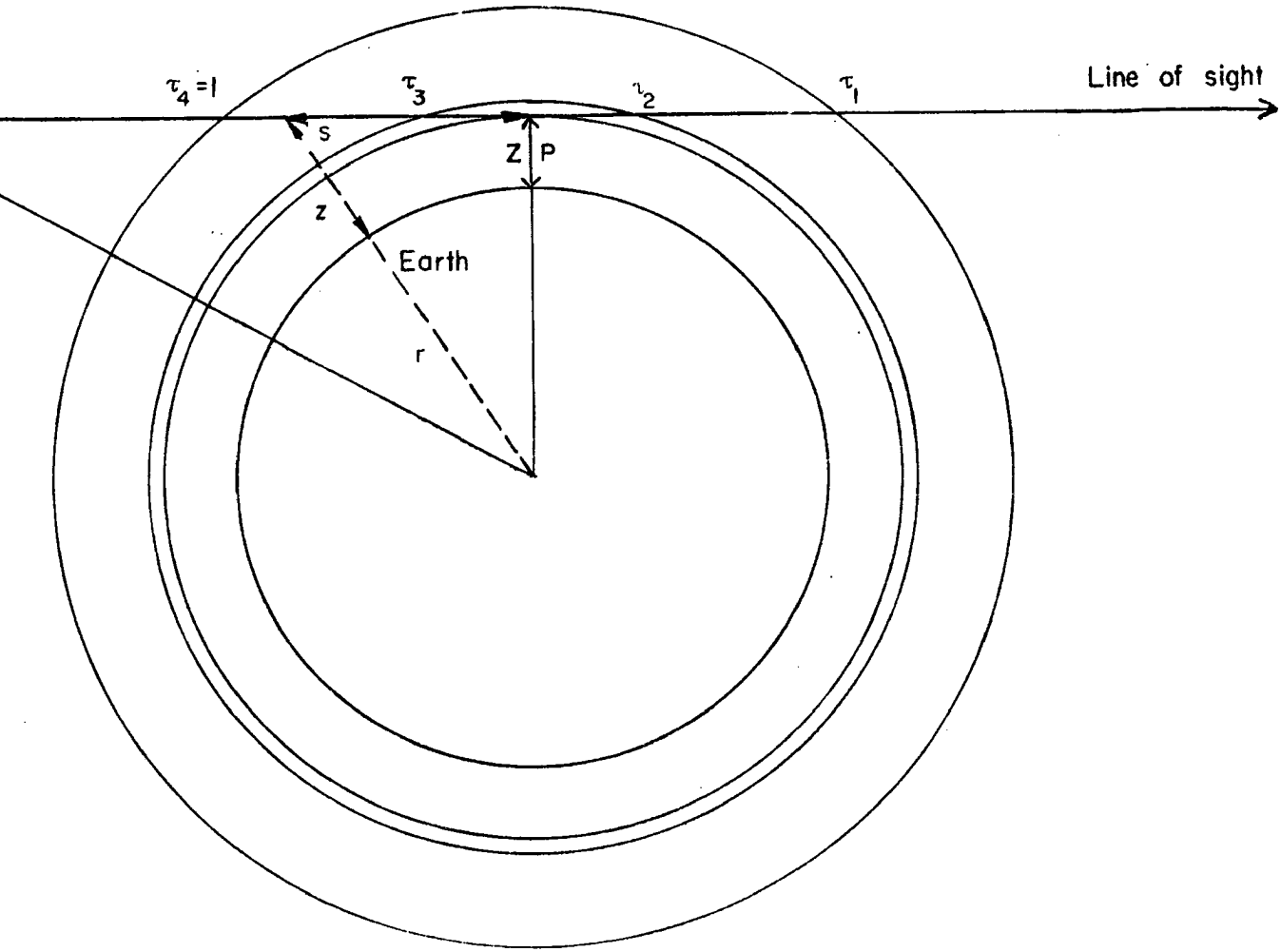


Figure 2.1 Limb geometry.

altitude is called the tangent height and is the minimum altitude of the line of sight from the surface. Total atmospheric pressure is also a unique characteristic of the tangent point and is called tangent pressure. A limb radiance profile is defined as the radiance from different lines of sight as a function of tangent pressure.

For lines of sight with tangent pressures in the stratosphere where clouds, solid boundaries, or radiation sources beyond the atmosphere are not normally present, the first term in equation (2.9) is zero which reduces the transfer equation to

$$N = -\int\int J_\nu \frac{\partial \tau_\nu}{\partial s} ds d\nu \ . \qquad (2.10)$$

In the earth's stratosphere thermodynamic equilibrium prevails (Goody, 1964) and, neglecting scattering, the source function becomes the Planck function

$$J_\nu = N_{B_\nu} = \frac{D_1 \nu^3}{\exp[\frac{D_2 \nu}{T} - 1]} \qquad (2.11)$$

which is a function of temperature and frequency.

Evaluation of equation (2.10) requires a knowledge of $\frac{\partial \tau_\nu}{\partial s}$ as well as the source function. Transmittance has been reviewed in Appendix A and was described as weakly dependent on temperature, strongly dependent on pressure, and strongly dependent on the amount of absorbing gas. Thus, the meteorological variables of temperature, pressure, and mixing ratio must be specified. Variation of transmittance with wave number must also be known. The mixing ratio of carbon

dioxide was assumed constant throughout the atmosphere for the present study. A mixing ratio value of 314 parts per million was used for the stratosphere. Bolin and Bischof (1970) report small variations in the free atmosphere with the magnitude decreasing into the stratosphere which supports the assumption.

The integration of equation (2.10) along the path can be transformed to an integration over pressure and thus eliminate height from the problem. From Figure 2.1 the distance from the tangent point outward is given by

$$s^2 = (r+z)^2 - (r+Z)^2 = 2r(z-Z) + z^2 - Z^2 \ . \quad (2.12)$$

Differentiation of equation (2.12) with Z and r considered constants for one tangent height yields

$$sds = rdz + zdz \ . \quad (2.13)$$

An approximation is possible here since r>>z. The largest Z involved is limited to the level where thermal emission by $CO_2$ and $H_2O$ is significant. Carbon dioxide emission is important to higher altitudes than water vapor but still has very small emission above 70 km; thus, the second term of equation (2.13) is of the order of 1 per cent or less of the first term and is omitted to yield

$$sds \simeq rdz \ . \quad (2.14)$$

If the atmosphere is considered to be an ideal gas in hydrostatic equilibrium the hydrostatic equation is

$$dp = -\frac{pg}{RT} dz \ . \quad (2.15)$$

Substitution of equation (2.14) into equation (2.15) gives the approximate dependence of path length on pressure as

$$sds \simeq -\frac{rRT}{pg}dp \tag{2.16}$$

which is integrated from the tangent point outward as

$$s^2 \simeq -2rR\int_p^p \frac{T}{pg}dp \ . \tag{2.17}$$

The calculation of transmittance as shown in Appendix A requires effective temperature, effective pressure, and amount of absorber. Effective temperature and pressure have been defined by equation (A.3) for use in $CO_2$ transmittance. Amount of absorber is given by the optical depth of the absorber which is

$$u = \int\frac{\rho_c ds}{\rho_s} = \int\frac{mw_c}{m_c}\frac{p}{p_s}\frac{T_s}{T}ds \ . \tag{2.18}$$

The factor of mass mixing ratio times the ratio of molecular weights is actually the mixing ratio by volume.

For water vapor the optical depth is referred to liquid water with $\rho = 1\ gcm^{-3}$

$$u = \int\rho_h ds = \int\frac{w_h p}{RT}ds \ . \tag{2.19}$$

The Elsasser model does not use the optical depth directly but rather the optical depth corrected for pressure and temperature effects for pressure broadening which is

$$u^* = \int\frac{w_h}{R}\frac{p_s}{T_s}\left(\frac{p}{p_s}\right)^2\left(\frac{T_s}{T}\right)^{3/2}ds \tag{2.20}$$

All elements needed for the evaluation of equation (2.10) are now available and the evaluation is accomplished as follows:

1. The atmosphere is divided into an arbitrary number of layers or shells with T, p, and W specified in each shell.
2. A tangent pressure is chosen.
3. Equation (2.17) is evaluated from the tangent point outward and the length, s, in each shell is stored.
4. Equation (2.18) for $CO_2$ and (2.20) for $H_2O$ are evaluated from the observer (Figure 2.1) along the line of sight and values of u and u* are stored for each shell.
5. Equation (A.3) is evaluated from the observer to each shell for $p_e$ and $T_e$ which are stored.
6. Transmittance is calculated from the observer, $\tau_\nu$ = 1.0, to each shell for each wave number interval and stored.
7. Equation (2.10) is then evaluated in each spectral interval by calculating $N_\nu$ for each shell and differentiating the $\tau_\nu$'s which were stored for each shell.

A radiance profile computed for the 615 $cm^{-1}$ to 715 $cm^{-1}$ spectral interval due to thermal emission of $CO_2$ is shown in Figure 2.2. Computations were made using temperatures and pressures from National Aeronautics and Space Administration et al. (1962) and a $CO_2$ mixing ratio of 314 parts per million

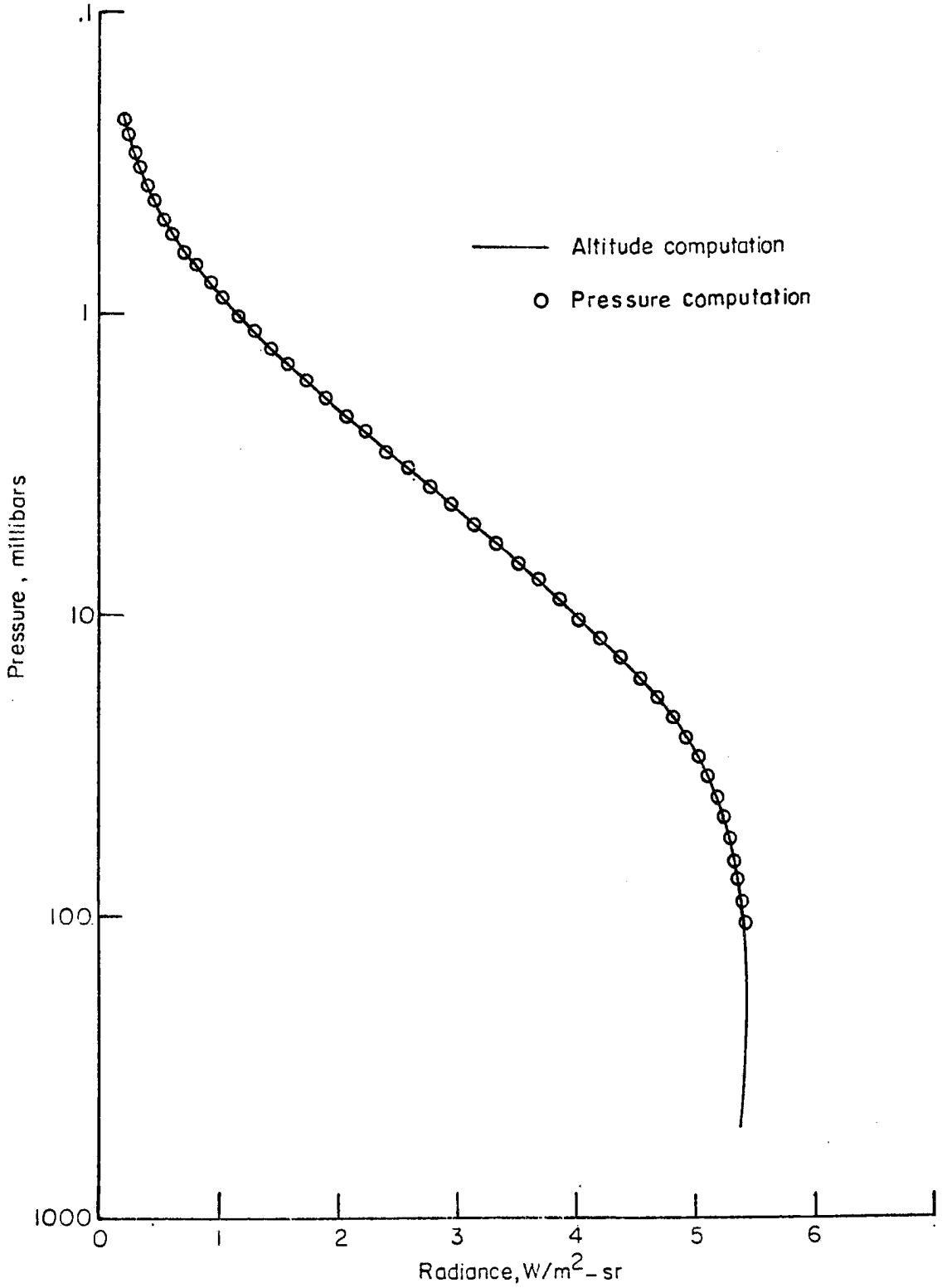


Figure 2.2 Limb radiance profile for 615 $cm^{-1}$ to 715 $cm^{-1}$.

by volume. In Figure 2.2 the effect of the approximation of equation (2.14) is also illustrated as the solid curve was obtained with a height integration using equation (2.12).

A limb radiance profile computed for the 205 $cm^{-1}$ to 295 $cm^{-1}$ spectral interval due to thermal emission of $H_2O$ vapor is shown in Figure 2.3 along with the mass mixing ratio used. Temperatures and pressures are again from National Aeronautics and Space Administration et al. (1962).

Radiance profiles in Figures 2.2 and 2.3 proceed from small radiance at small tangent pressures to a larger radiance plateau at larger tangent pressures. This basic feature is caused by the transmittance. The change in transmittance from the observer to a point completely through the atmosphere is nearly zero for small optical depths at small tangent pressure, and is essentially unity as the gas becomes opaque with large optical depths. If the atmosphere were isothermal the spectral radiance would be

$$N_\nu = -N_{B_\nu} \int \frac{\partial \tau_\nu}{\partial s} ds = -N_{B_\nu} \int d\tau_\nu$$

which indicates the entire shape of the radiance profile would be determined by the changes in transmittance. Changes of temperature and mixing ratio as a function of pressure do produce significant variations from the basic shape of the limb radiance profile.

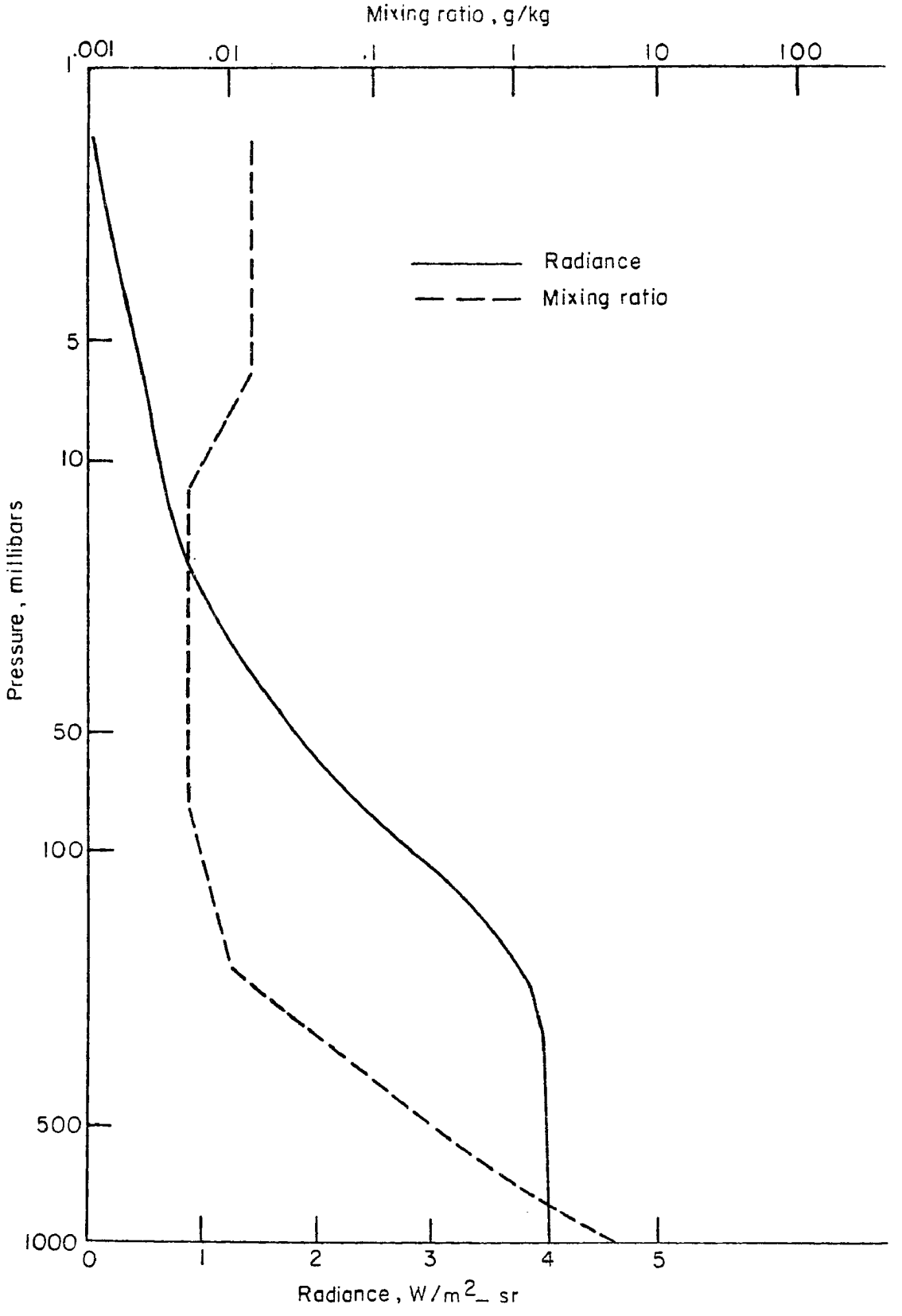


Figure 2.3 Limb radiance profile and water vapor mixing ratio for 205 $cm^{-1}$ to 295 $cm^{-1}$.

# CHAPTER III

## INFERENCE OF TEMPERATURE AND WATER VAPOR

The transfer equation for limb radiance is repeated as

$$N(P) = -\int\int N_{B_\nu}(T)\frac{\partial \tau_\nu}{\partial s}dsd\nu \ . \qquad (3.1)$$

Inference of temperature or water vapor is basically the problem of measuring the integrated value, N(P), and then deducing some characteristic of the integrand which is either T or $H_2O$ mixing ratio. Measurement of the radiance is a straightforward radiometric problem with the primary difficulty associated with construction of an instrument which has a very small optical field of view that approximates a line of sight as in Figure 2.1 and has an acceptable signal to noise ratio. Measurement of the position of the line of sight with respect to the earth is a much more difficult problem. No method is known to measure the pressure of the tangent point. Measurement of the tangent height, Z, has been accomplished in an experiment described by McKee et al. (1968) and Walsh et al. (1968). Unfortunately the cost and complexity of measuring tangent height eliminates its use for routine atmospheric experiments.

Techniques to infer atmospheric temperature from measurements of radiance as a function of tangent height have been developed by McKee et al. (1969a), House and Ohring

(1969), and Burn and Uplinger (1970). Related methods to infer water vapor mixing ratio were proposed by McKee et al. (1969b) and House and Ohring (1969).

Development of a method to infer temperature and water vapor mixing ratio from limb radiance data which does not demand a measurement of tangent height would be useful and is the subject of this section. Primary features of the derivation have been described previously by McKee (1970).

A tangential view of the atmosphere as shown in Figure 2.1 provides very long path lengths in very thin altitude layers near the tangent point. In fact the linear distance through a layer 1 km thick at the tangent point is 225 km. This factor coupled with the rapid decrease of pressure with height produces a distribution of atmospheric mass along the line of sight that is sharply peaked at the tangent point. Figure 3.1 illustrates the mass distribution which in relative units is nearly the same for any tangent pressure. Half the mass is located within a vertical pressure change of about 20 per cent or 1.5 km in height. For a uniformly mixed gas such as $CO_2$ the same distribution will prevail. Equation (3.1) can be rewritten as

$$N(P) = -\int\int N_{B_\nu}(T)\frac{\partial \tau_\nu}{\partial p}dpd\nu \qquad (3.2)$$

where the integration is over pressure along the line of sight. The shape of the kernal of the integral in (3.2) plotted as a function of p is dominated by the factor $\frac{\partial \tau_\nu}{\partial p}$. The factor $\frac{\partial \tau_\nu}{\partial p}$ will have a distribution with pressure

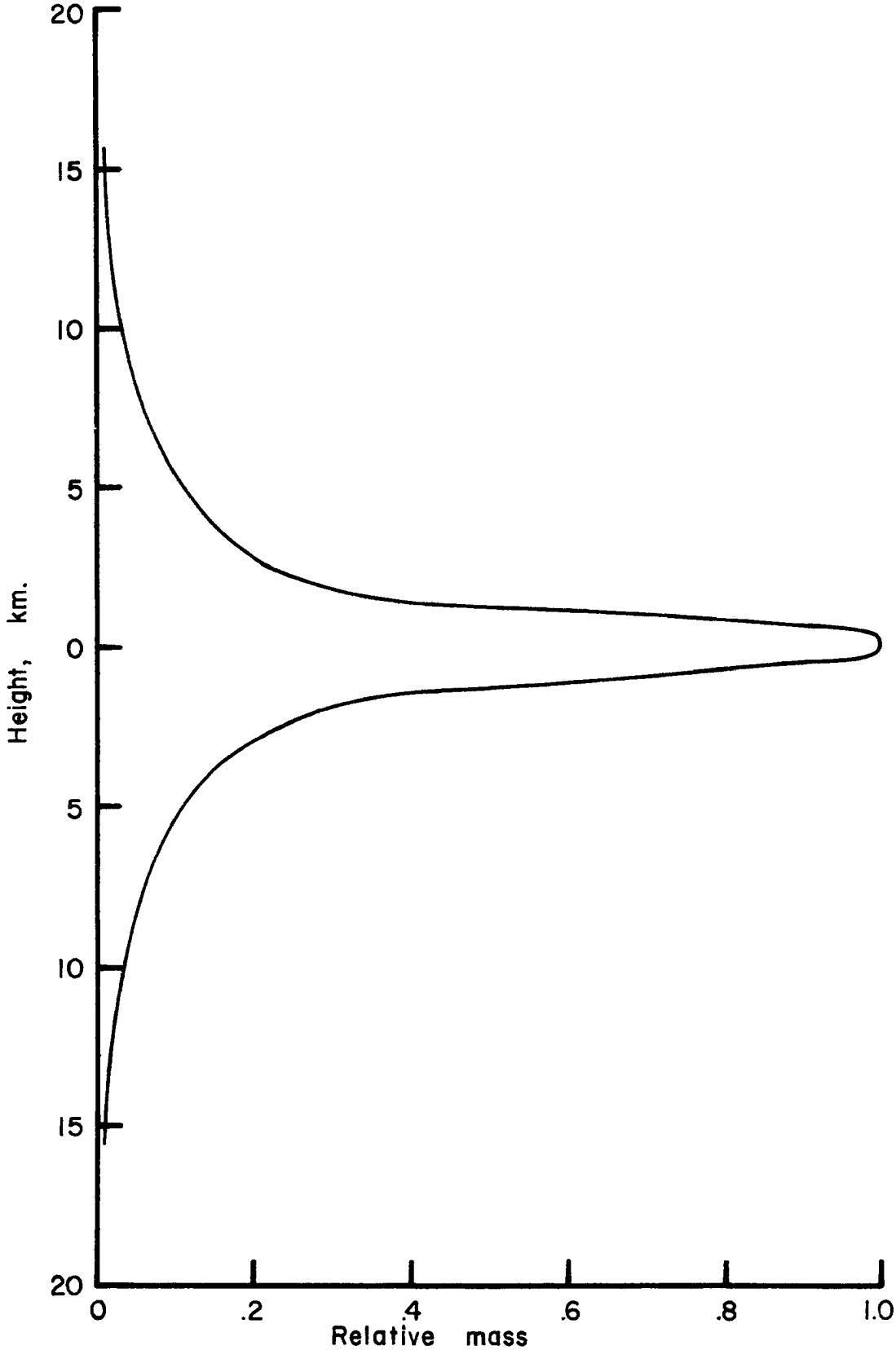


Figure 3.1 Distribution of mass along line of sight.

similar to the mass distribution in Figure 3.1 as long as the gas is semi-transparent due to the strong influence of optical depth on transmittance. As the gas becomes opaque the distribution of $\frac{\partial \tau_\nu}{\partial p}$ will shift toward the observer and broaden considerably.

The primary result of the sharply peaked kernal of equation (3.2) is that a large fraction of the radiance from a particular tangent pressure originates in a rather narrow vertical layer of the atmosphere. Consequently, when the line of sight is moved 20 per cent in tangent pressure, a substantial amount of the radiance will originate in a new layer. This physical fact is the basic element in the concept that a series of radiances from different tangent pressures contain the information necessary to infer atmospheric temperature or water vapor mixing ratio.

Inference of Temperature

The inference of temperature requires three assumptions which have been discussed elsewhere:

(1) Transmittance model

(2) Mixing ratio of $CO_2$ as a function of pressure

(3) Absence of clouds in line of sight

For ease of symbolism equation (3.1) is rewritten as

$$N(P) = -\int_{\nu_l}^{\nu_u} \int_{1}^{\tau_1} N_{B_\nu}(T)\, d\tau_\nu d\nu \qquad (3.3)$$

where the limits on $\tau$ are shown as points along the line of sight in Figure 2.1 and the limits on $\nu$ are merely the lower and upper wave number limits.

The iterative technique to obtain temperature begins at small radiance values and proceeds to larger values. At the first level to be inferred, the theoretical radiance is calculated as

$$N_t(P_o) = -\int_{\nu_l}^{\nu_u}\int_{1}^{\tau_1} N_{B_\nu}(T)\,d\tau_\nu\,d\nu \tag{3.4}$$

where the atmosphere above $P_o$ is assumed to be hydrostatic and have a constant lapse rate with height. Then temperature as a function of pressure is given by

$$T = T_o\left(\frac{p}{p_o}\right)^{-\frac{R\gamma}{g}} . \tag{3.5}$$

Initial values of $T_o$, $P_o$, and $\gamma$ are assumed. From a measured radiance profile, the radiance difference between calculated and measured values is the radiance residuals

$$\Delta N(P_o) = N_m(P_o) - N_t(P_o) . \tag{3.6}$$

At this point it is possible to determine a temperature change, $\Delta T$, and iterate until $\Delta N(P_o)$ is small.

In order to develop an efficient method of determining a $\Delta T$, equation (3.4) is approximated by removing the source function from the integrand and evaluating the source function at an average value of $\nu$ which is $\frac{\nu_l + \nu_u}{2} = \nu_a$ so that

$$N_t(P_o) \simeq -N_{B_{\nu_a}}(T_o) \int_{\nu_l}^{\nu_u} \int_1^{\tau_1} d\tau_\nu d\nu \ . \qquad (3.7)$$

Since $\tau_\nu$ depends only slightly on temperature, an approximation to the change in calculated radiance from equation (3.7) is

$$\frac{\Delta N_t}{\Delta T} \simeq -\frac{\partial N_{B_{\nu_a}}}{\partial T} \int_{\nu_l}^{\nu_u} \int_1^{\tau} d\tau_\nu d\nu \ . \qquad (3.8)$$

From the Planck function of equation (2.11), one obtains

$$\frac{\partial N_{B_\nu}}{\partial T} = \frac{N_{B_\nu}(T)\ D_2\nu}{T^2} \frac{\exp(\frac{D_2\nu}{T})}{\exp(\frac{D_2\nu}{T})-1} \ . \qquad (3.9)$$

For the present problem $D_2$=1.4389 cm°K, $\nu_a$=665 $cm^{-1}$, and 200 °K$\leq$T$\leq$300 °K or $24 \leq \exp\frac{D_2\nu}{T} \leq 118$. Thus to an accuracy of 4 per cent or better the factor $\frac{\exp\frac{D_2\nu}{T}}{\exp\frac{D_2\nu}{T}-1}$ is unity which leaves

$$\frac{\partial N_{B_\nu}}{\partial T} \simeq \frac{N_{B_\nu}(T) D_2\nu}{T^2} \ . \qquad (3.10)$$

Substitution into equation (3.8) with the average wave number values results in

$$\frac{\Delta N}{\Delta T} \simeq -\frac{N_{B_{\nu_a}}(T_o) D_2\nu_a}{T_o^2} \int_{\nu_l}^{\nu_u} \int_1^{\tau_1} d\tau_\nu d\nu \ . \qquad (3.11)$$

Now the substitution of equation (3.11) into equation (3.6) provides an equation for determining $\Delta T$ which is

$$\Delta T \simeq -\frac{[N_m(P_o) - N_t(P_o)]\ T_o^2}{N_{B_{\nu_a}}(T_o) D_2\nu_a \int_{\nu_l}^{\nu_u} \int_1^{\tau_1} d\tau_\nu d\nu} \ . \qquad (3.12)$$

This equation for $\Delta T$ is used to change $T_o$ in the expression for $N_t(P_o)$ until the radiance residual is made small. The values of $P_o$ and $\gamma$ remain unchanged. The calculation then proceeds to the next larger radiance value.

Calculation of a radiance to compare with the measured radiance requires a knowledge of the location of the new line of sight in the atmosphere. A technique to determine the tangent pressure without accurate pointing information is derived below.

The geometry of the limb problem (Figure 2.1) yields a relationship between tangent height and nadir angle as

$$r + Z = (r + z) \sin\theta$$

For one scan the radius, r, and the observer altitude, z, are constant so that the time derivative of the tangent height is

$$\frac{dZ}{dt} = (r+z) \cos\theta \frac{d\theta}{dt} . \qquad (3.13)$$

The vertical scan rate, $\frac{d\theta}{dt}$, is an easily measured quantity in any experiment for limb scanning. Radar tracking or orbit determination allows an accurate evaluation of (r+z). Determination of the value for $\cos\theta$ would appear more difficult. For a satellite at 1000 km altitude the nadir angles for tangent pressures of 100 mb and 1 mb are 60.0528 deg. and 60.55496 deg. respectively. The values of the $\cos\theta$ are 0.499202 and 0.49159 which are different by only 1.324 per cent. Since the atmosphere does not vary greatly in the horizontal or with time, a knowledge of a calculated limb radiance profile for any given spectral interval is

sufficient to use in determining the value of $\cos\theta$. Accuracies better than 1.0 per cent could be achieved by separating the radiance profile into segments. All the elements are now assembled for determining $\frac{dZ}{dt}$ but the change in tangent pressure is the desired quantity. The hydrostatic equation may be expressed in terms of the variables which define the tangent point as

$$dP = \frac{-pg}{RT}\, dZ \ . \tag{3.14}$$

Assuming an average temperature for the layer and integrating, one gets

$$P_i = P_{i-1}\exp[\frac{g\Delta Z}{RT_a}] \tag{3.15}$$

where $\Delta Z$ is merely the thickness of the layer and $P_{i-1}$ is the old tangent pressure and $P_i$ is the new and larger pressure. From equation (3.13)

$$\Delta Z = (r+z)\ \cos\theta\ \frac{d\theta}{dt}\ \Delta t \ . \tag{3.16}$$

Then (3.15) becomes

$$P_i = P_{i-1}\ \exp\ \frac{g(r+z)\ \cos\theta\ \frac{d\theta}{dt}\ \Delta t}{RT_a} \ . \tag{3.17}$$

Equation (3.17) provides the specification of the new tangent pressure needed to calculate a radiance and it also insures that the new layer is in hydrostatic balance.

Equation (3.17) is first used with $P_{i-1} = P_o$ and $T_a = T_o$ to estimate the new pressure $P_i$. A radiance is next computed for the $i^{th}$ layer and the radiance residual is expressed as

$$N(P_i) = N_m(P_i) - N_t(P_i) \ . \tag{3.18}$$

From $\Delta N_i(P_i)$ a $\Delta T_i$ is calculated using the equation

$$\Delta T_i = - \frac{[N_m(P_i) - N_t(P_i)]T_i^2}{D_2 \nu_a N_{\nu_a}(T_i) \int_{\nu_l}^{\nu_u} \int_{\tau_3}^{\tau_4} d\tau_\nu d\nu} \quad . \tag{3.19}$$

Equation (3.19) is similar to but not the same as equation (3.12) used for the starting point. After iterating to find the value of $T_o$ which makes the radiance residual small, equation (3.4) for $N_t(P_i)$ accounted correctly for all the atmosphere above the pressure $P_o$. Consequently, when a new line of sight is considered at $P_i$, only the new layer below $P_o$ is causing a radiance residual. Thus, the limits of the $\tau_\nu$ integration in the denominator of equation (3.19) only include the new layer from $\tau_3$ to $\tau_2$ as shown in Figure 2.1.

Equations (3.18), (3.19), and (3.17) are used in an iterative operation until $\Delta N(P_i)$ is small when a new average temperature has been found and the layer is in hydrostatic balance. The calculation then proceeds to the next radiance value and, thus, works down through the atmosphere layer by layer.

Figure 3.2 illustrates the inference of temperature from a limb radiance profile calculated using the atmosphere of National Aeronautics and Space Administration et al. (1962). The spectral region was 615 $cm^{-1}$ to 715 $cm^{-1}$ and the volume mixing ratio of $CO_2$ was 314 parts per million. Slight errors in temperature at the smallest pressures are due to the assumption of a lapse rate of 4° K $km^{-1}$ when the

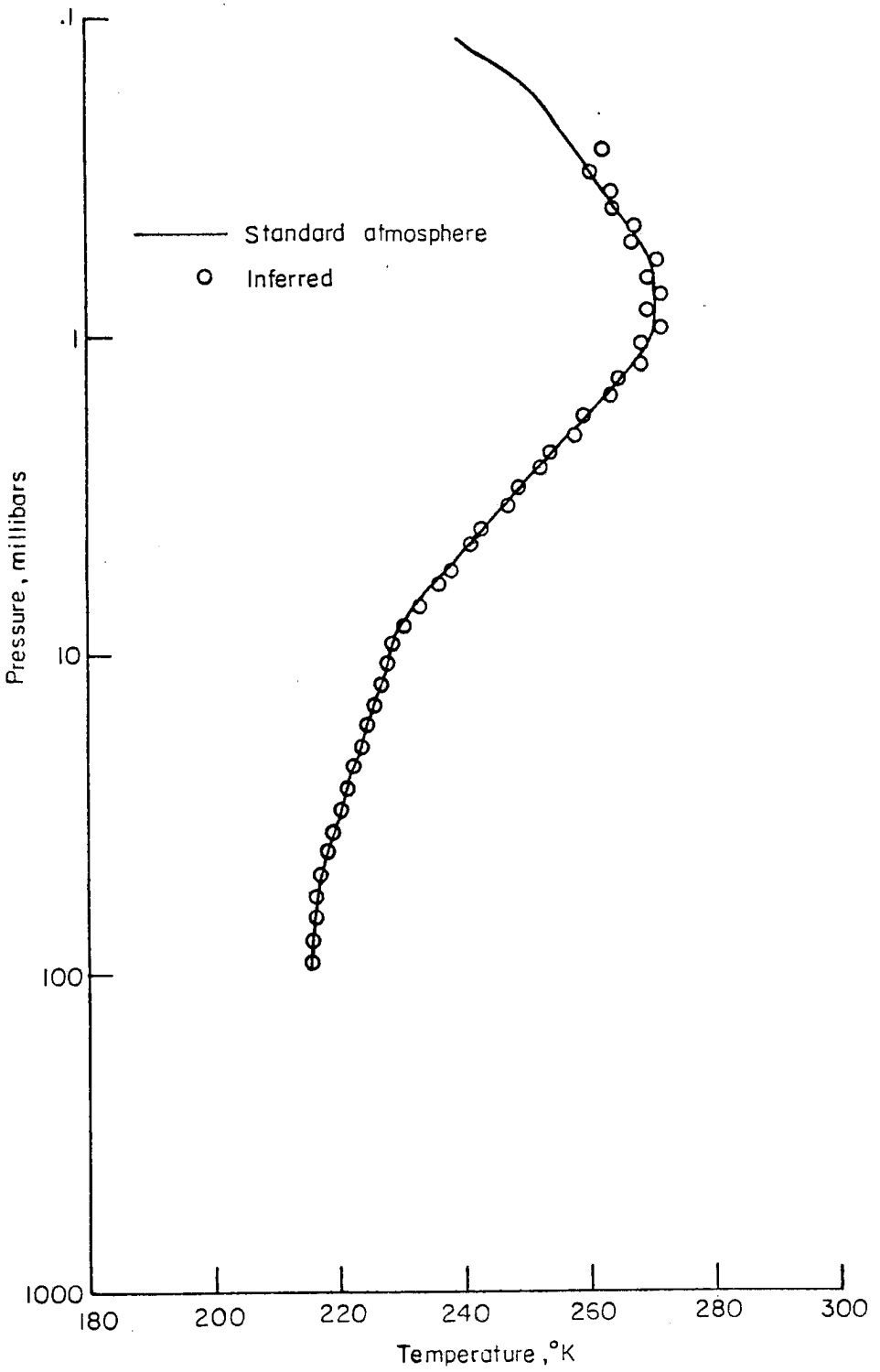


Figure 3.2 Inferred temperature profile.

actual lapse rate is changing from 2° K $km^{-1}$ to 4° K $km^{-1}$. The pressure range of the inference is from 0.3 mb to 100 mb. This example which used essentially an errorless set of radiances appears quite accurate; however, the sensitivity of the inference to various errors in radiance is important. In Figure 3.3 the results of temperature inference are shown after three common types of radiance errors (scale, bias, random noise) have been introduced. The magnitude of each error chosen is not unreasonable considering present radiometric technology even though a random noise of 0.01 W $m^{-2}$ $sr^{-1}$ root mean square would normally require a cooled detector. A good indicator for the magnitude of the temperature errors is that the diameter of the circular symbol in Figure 3.3 is about 2° K. Systematic errors of scale and bias produce a systematic effect on temperature which would be difficult to detect in an actual application. Random noise effects are most noticeable at small radiance values where noise is a larger fraction of radiance and again at large pressures (not too evident in Figure 3.3c) where the fraction of radiance in a new layer is quite small. The inference method does not appear particularly sensitive to the errors assumed here.

An error in the assumed pressure for the first layer, $P_o$, is a different problem since such an error is not dependent on instrument properties. Figure 3.4 shows the effect of a 10 per cent error in initial pressure. This

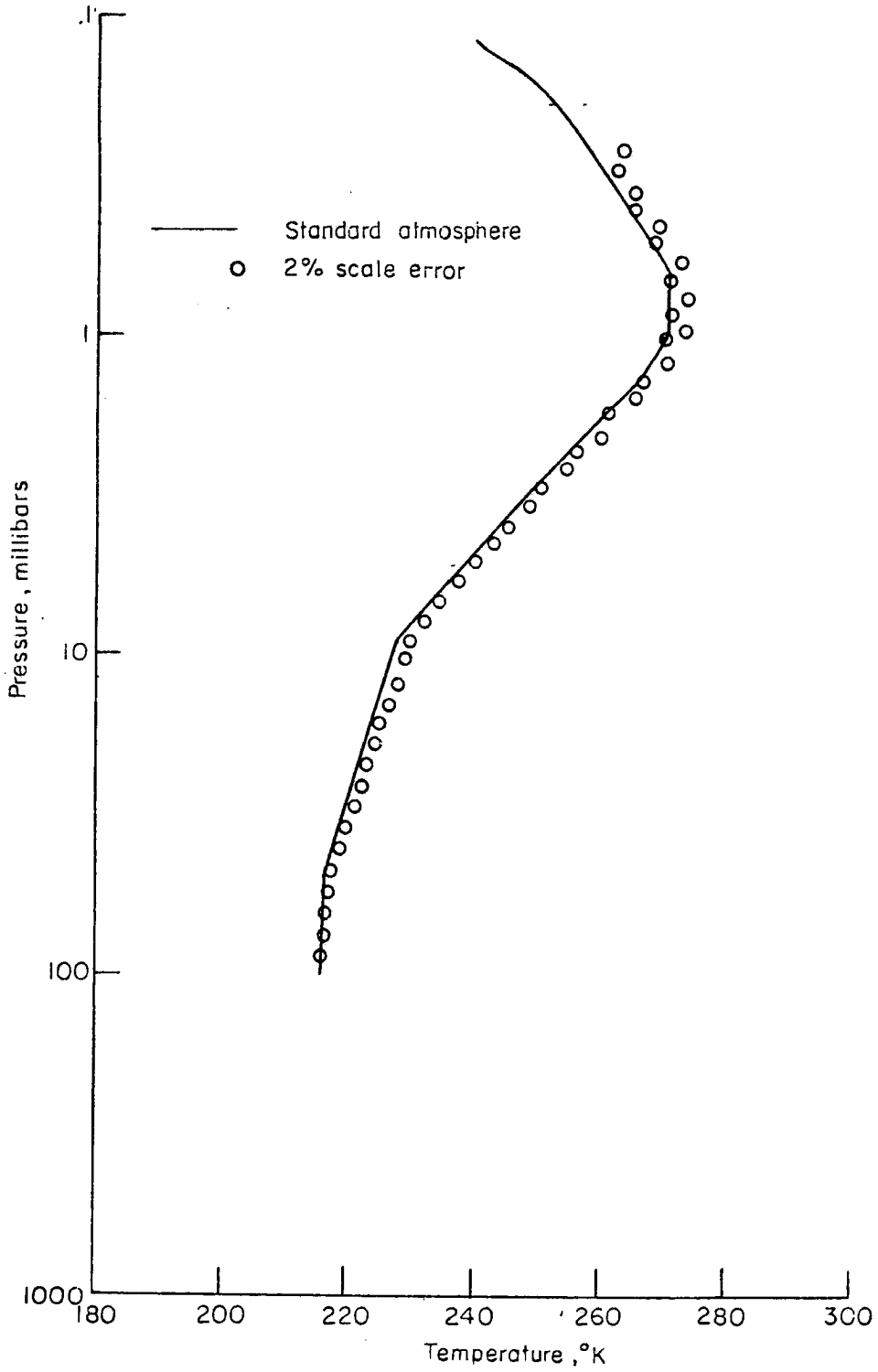


(a) Scale radiance error

Figure 3.3 Inferred temperature profile with radiance error.

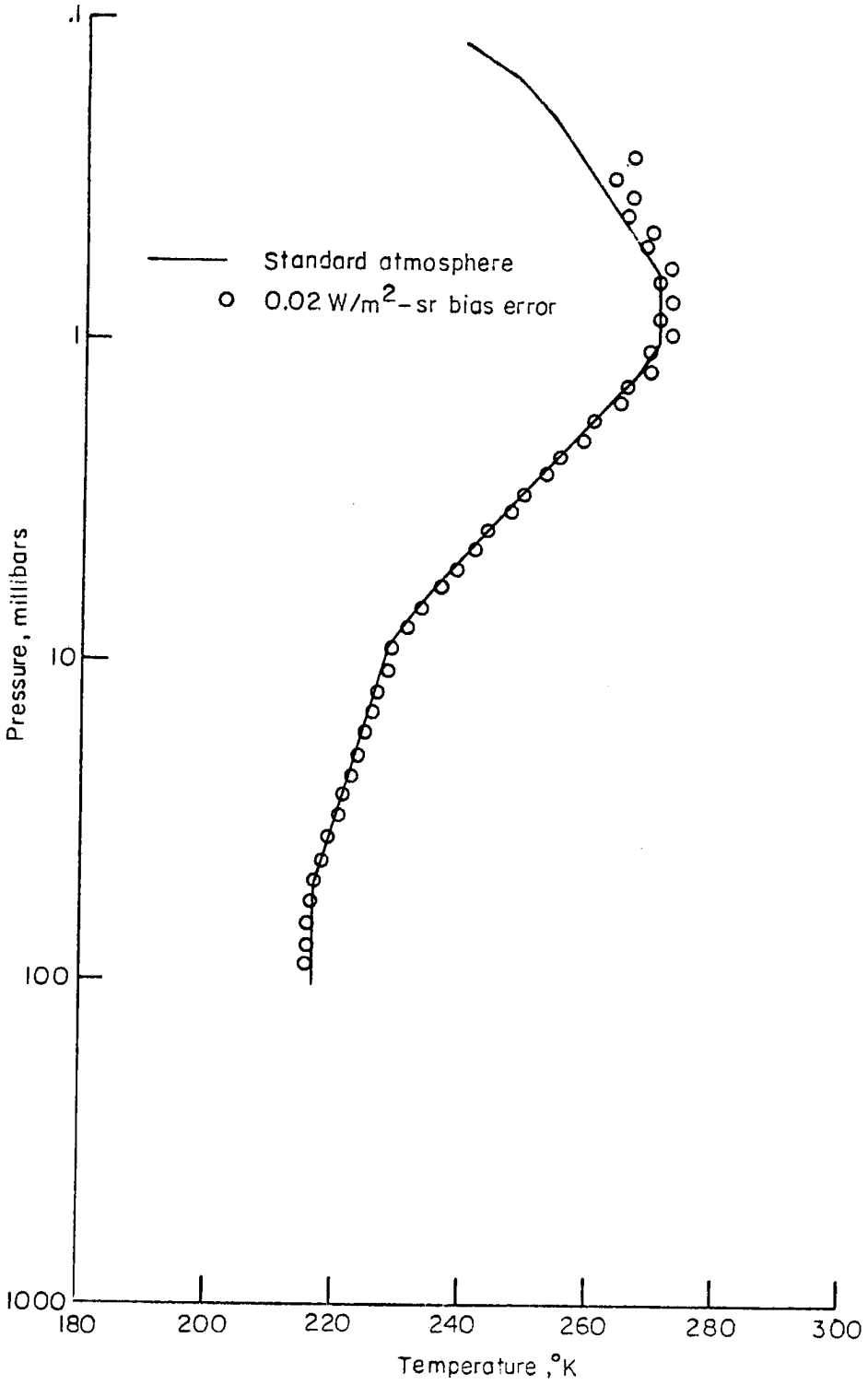


(b) Bias radiance error

Figure 3.3 Continued.

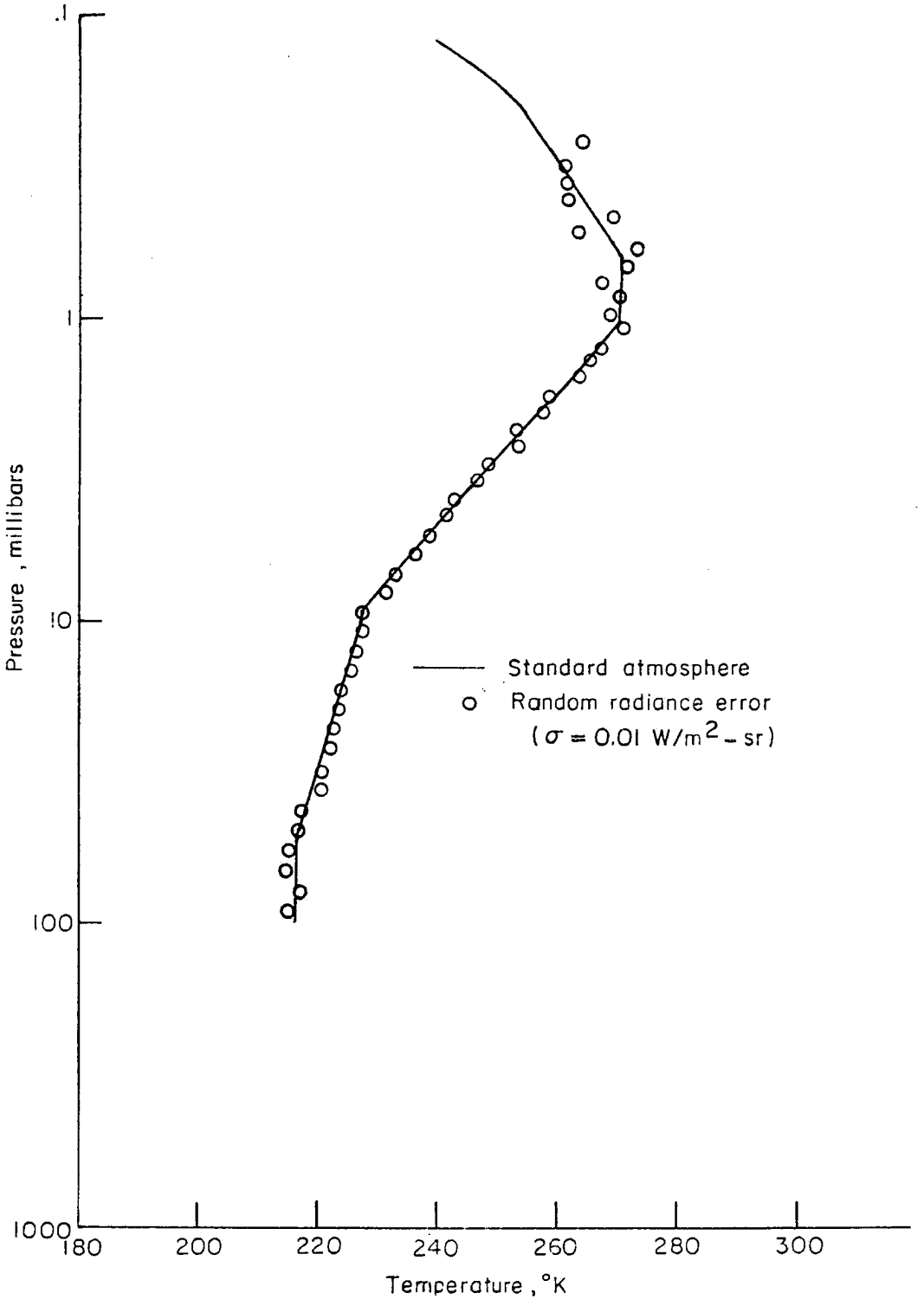


(c) Random radiance error

Figure 3.3 Concluded.

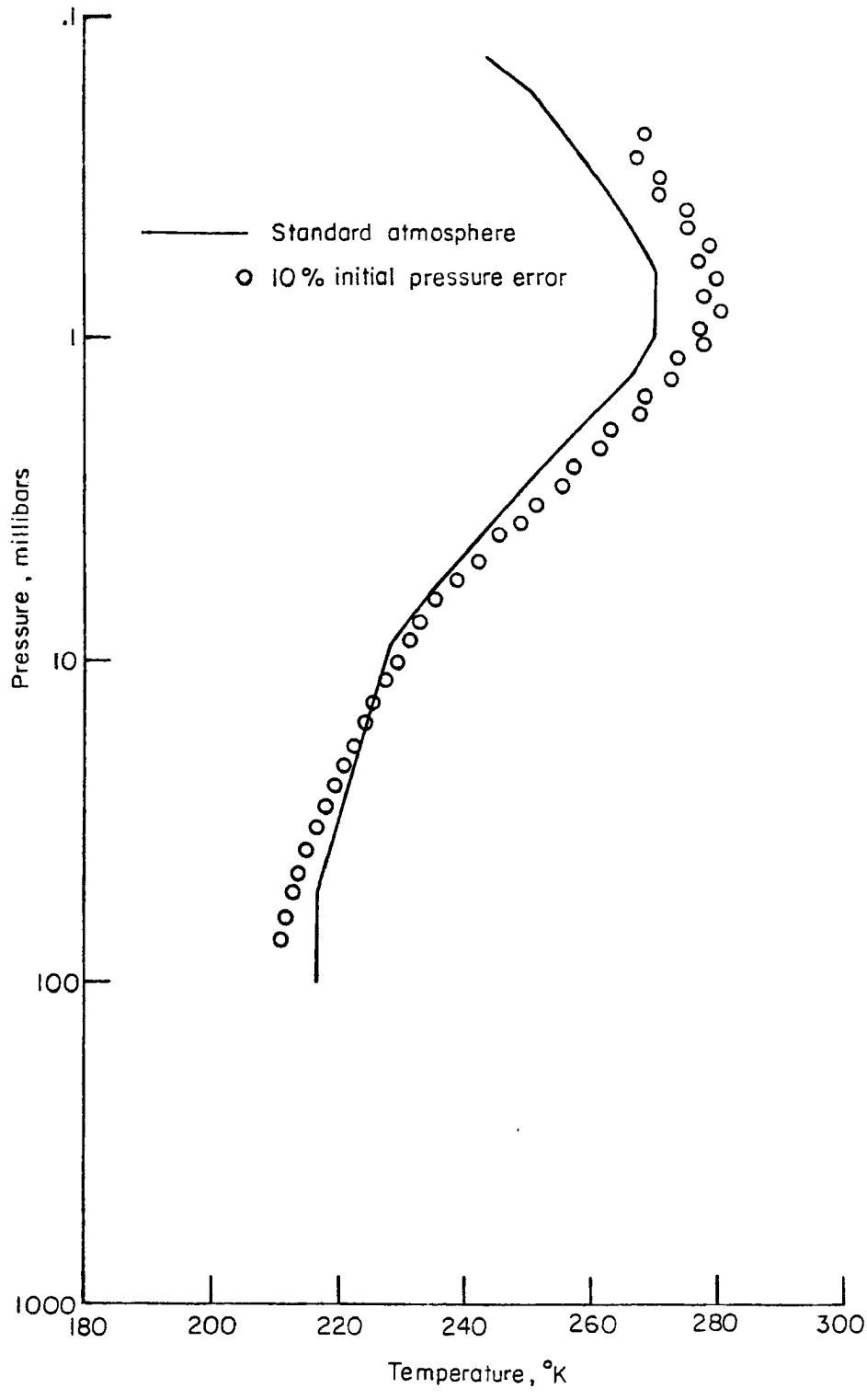


Figure 3.4 Inferred temperature profile with initial pressure error.

error has a much more devastating effect than any of the instrumental type errors.

The initial pressure can be dealt with in several ways. If the pressure is known for any radiance value, the initial pressure could be adjusted until a fit is obtained. A second method is that radiance and radiance slope could be correlated to pressure through use of climatological data. The accuracy of this has not been pursued. A third method, which is used later in this study, is to fit the inferred temperatures and lapse rate to radiosonde data at the lower boundary for pressures of 10 mb and greater. This method should work quite well where radiosonde data are available but can not be used if independent data are not available. A quite different fourth method has been suggested by McKee (1970). Two spectral intervals within the 15μ region could be used and the region of tangent pressure where both spectral intervals give a solution could be compared until the temperatures agree. Thus, the arbitrary constant would be eliminated. This approach has been pursued by Gille and House (1971) and will be used in an experiment planned on a future Nimbus satellite.

Inference of Water Vapor

The inference of water vapor mixing ratio requires several assumptions:

(1) Transmittance model

(2) Temperature as a function of pressure

(3) Tangent pressure of line of sight

(4) Absence of clouds in line of sight

Assumptions (2) and (3) are met by optically aligning the radiometer used in measuring water vapor emission with the radiometer used to gather data for temperature inference. Only on rare occasions will assumption (4) be a poor one and when clouds do occur the inferred relative humidity will greatly exceed 100 per cent. Assumption (1) has been investigated by Whitman (1971) for the spectral interval 315 $cm^{-1}$ to 475 $cm^{-1}$. Three transmittance models from Elsasser (1960), Goody (1964) and Smith (1969) were used with the inference technique of McKee et al. (1969). Results indicate that the absolute magnitude does depend on the model used, and more importantly that at pressures smaller than about 10 mb the shape of the mixing ratio profile as a function of pressure (or height) becomes model dependent.

The iterative technique for inferring water vapor mixing ratio starts at a small radiance value corresponding to a small tangent pressure. A radiance is calculated by equation (3.3) with an assumed mixing ratio, $w_o$, considered constant for all pressures smaller than $P_o$. A radiance residual is then formed as

$$\Delta N(P_o) = N_m(P_o) - N_t(P_o) \ . \qquad (3.20)$$

The mixing ratio is changed and a new radiance is calculated in an iterative manner until $\Delta N(P_o)$ is made small. Mixing ratio is changed by the linear relation

$$\Delta w = w\frac{\Delta N}{N_t} . \tag{3.21}$$

That this linear correction works quite well is apparently due to the fact that transmittance in equation (3.3) for a wide spectral band is a smoothly decreasing function of optical depth, hence mixing ratio; thus, a linear extrapolation for thin atmospheric layers is a reasonable approximation.

The inference proceeds to the next radiance value. A radiance is calculated assuming no change in mixing ratio from the layer above. A new residual is formed as

$$\Delta N(P_i) = N_m(P_i-) - N_t(P_i) . \tag{3.22}$$

The calculated radiance came from equation (3.3) which is expanded as

$$N_t(P_i) = -\int_{\nu_l}^{\nu_u}\int_{\tau_4}^{\tau_3} N_\nu(T)\,d\tau_\nu d\nu - \int_{\nu_l}^{\nu_u}\int_{\tau_3}^{\tau_2} N_\nu(T)\,d\tau_\nu d\nu - \int_{\nu_l}^{\nu_u}\int_{\tau_2}^{\tau_1} N_\nu(T)\,d\tau_\nu d\nu . \tag{3.23}$$

When the mixing ratio is to be changed the only effect will be in the $\tau_\nu$ of the middle integral which involves the new layer. Thus the update of mixing ratio is determined by

$$\Delta w = \frac{w\Delta N}{-\int_{\nu_l}^{\nu_u}\int_{\tau_3}^{\tau_2} N\nu(T)\,d\tau_\nu d\nu} . \tag{3.24}$$

The mixing ratio is changed until $\Delta N(P_i)$ is made small and the inference continues in a like manner layer by layer.

Figure 3.5 illustrates the inference of water vapor mixing ratio from a limb radiance profile. The radiance values were calculated using the same temperature profile noted for temperature inference and the water vapor distribution of Figure 2.3 which is called the reference mixing ratio. The spectral interval used is 205 $cm^{-1}$ to 295 $cm^{-1}$ and tangent pressures ranged from 3 mb to 200 mb. Figure 3.5 illustrates essentially that the calculations of radiance are repeatable. Sensitivity to radiance errors is shown in Figure 3.6 where scale, bias, and random radiance errors were imposed on the calculated radiances. The mixing ratio error due to scale radiance error is largest and increases at large pressures. As noted for temperature inference, the random error chosen is not unreasonable but care would be required to achieve such a measurement. Since an accuracy of 50 per cent in mixing ratio at the drier levels would be an improvement on present knowledge, the sensitivity to errors is not serious at all.

Discussion of Errors

Examples of the effects of errors in radiance have been represented in the preceding sections. Appendix B contains a more extensive investigation of the effects of random radiance errors and the effects of ignoring horizontal temperature gradients in the inference of temperature and the derived quantities of geopotential height, geostrophic wind, and wind shear. A summary of the primary results of Appendix B is included here for continuity.

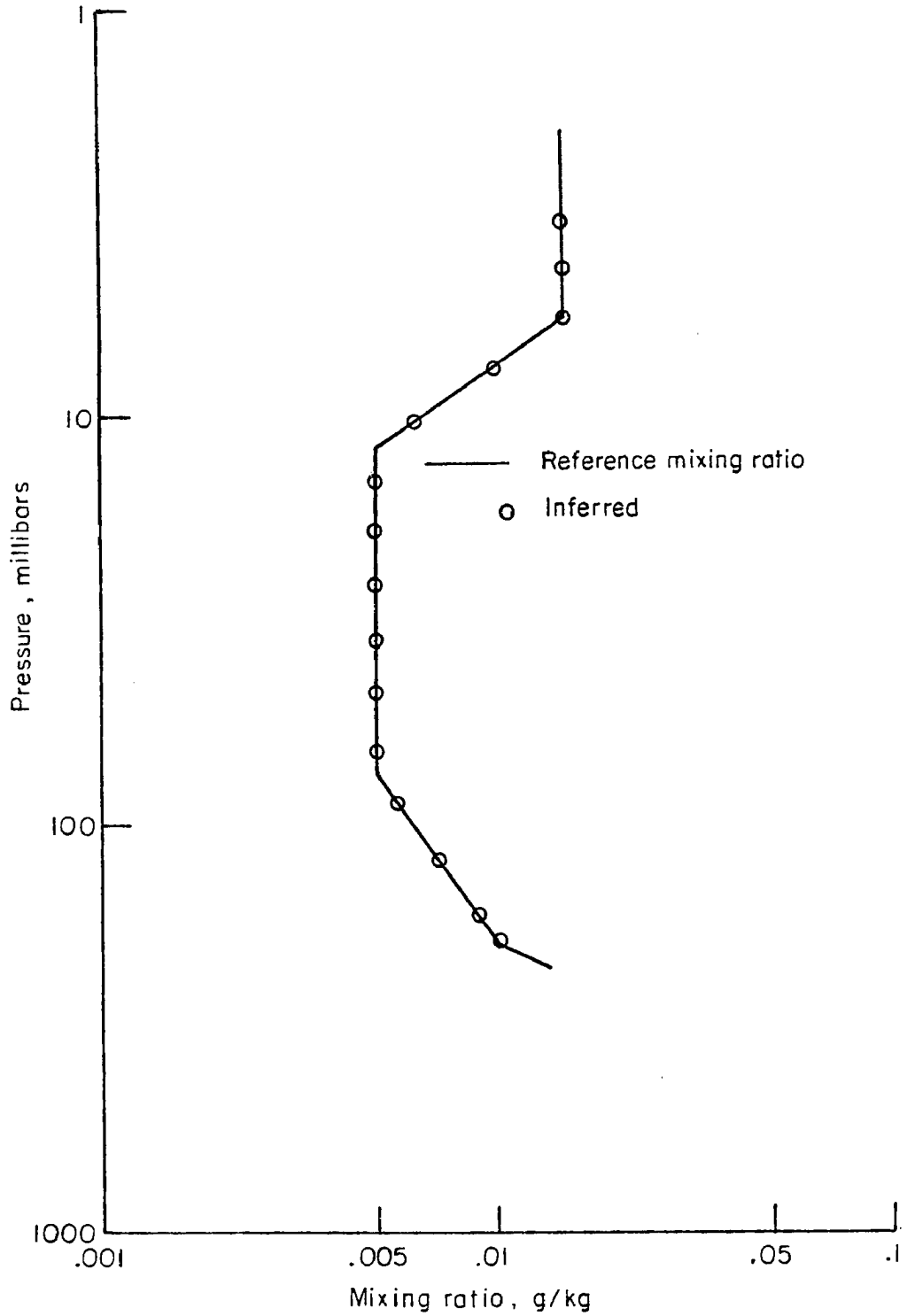


Figure 3.5 Inferred water vapor mixing ratio.

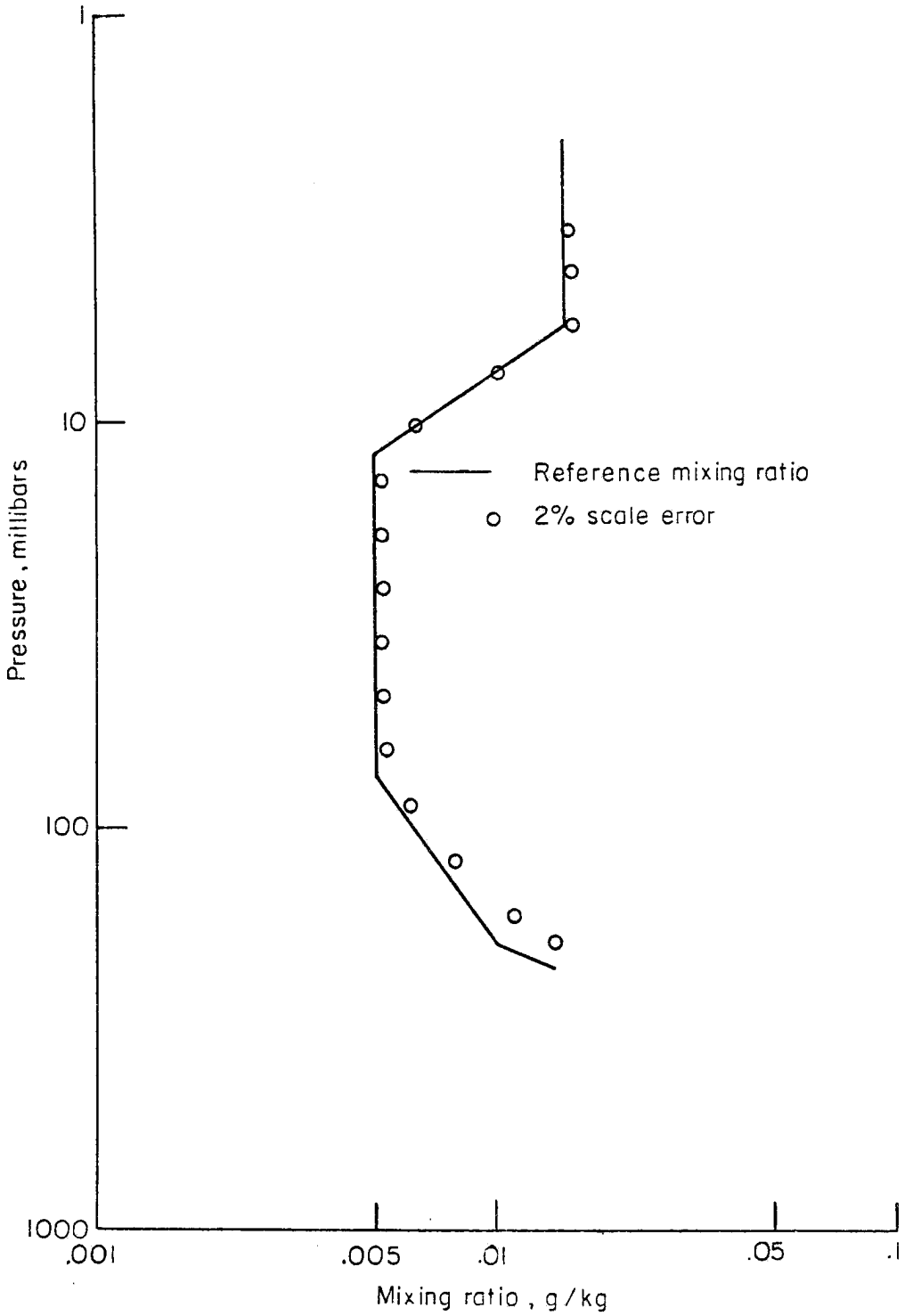


(a) Scale radiance error

Figure 3.6 Inferred water vapor mixing ratio with radiance errors.

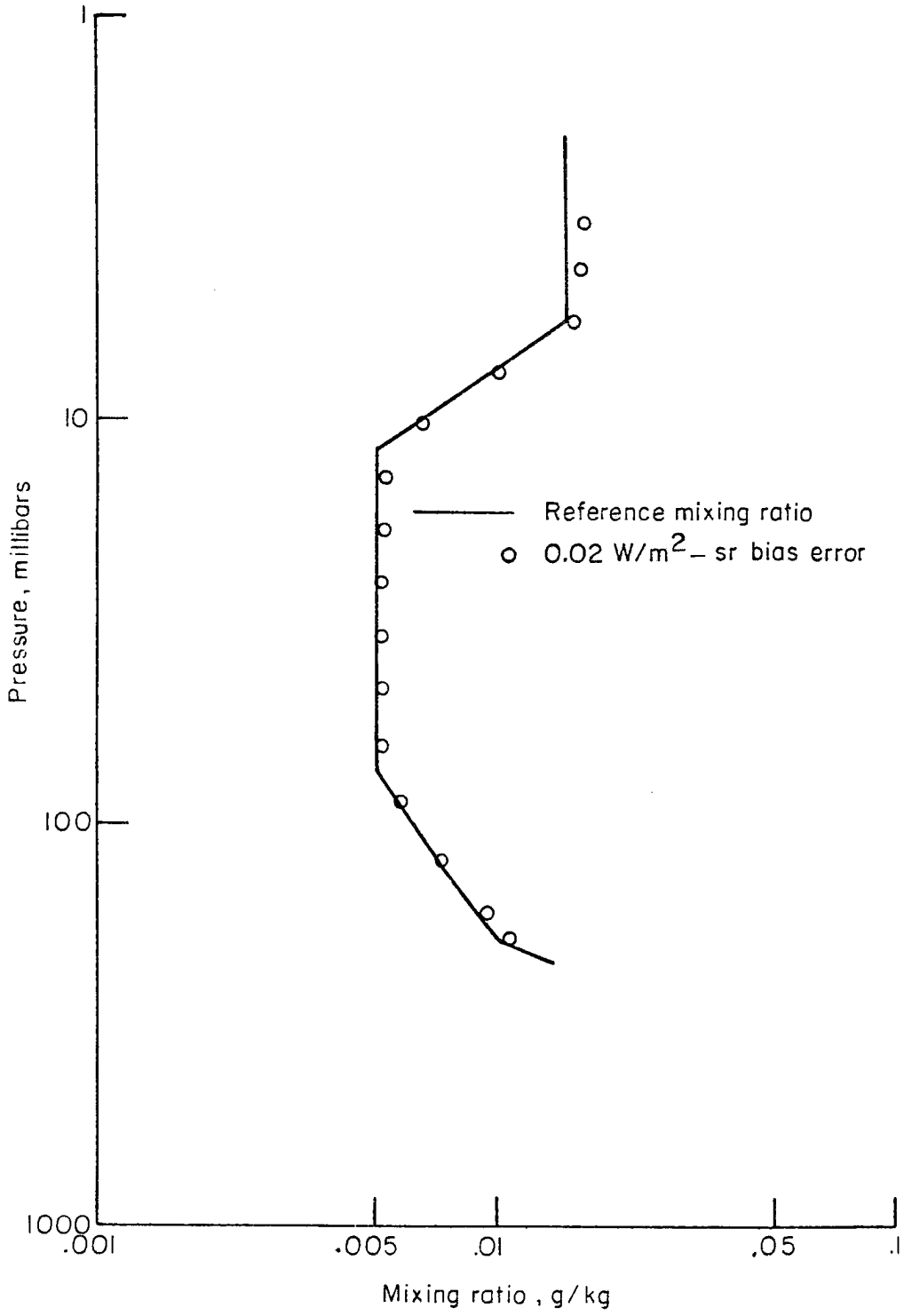


(b) Bias radiance error

Figure 3.6 Continued.

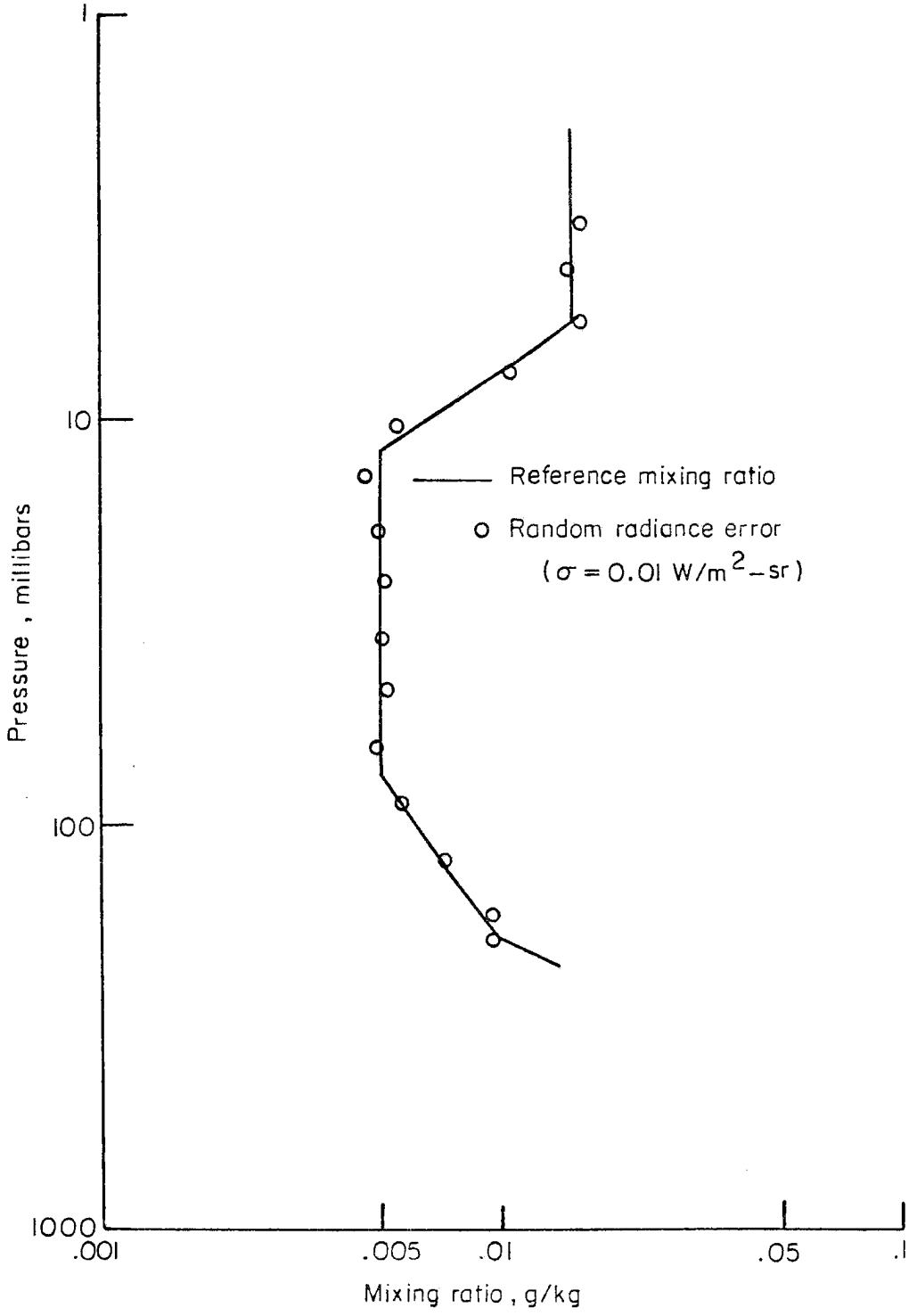


(c) Random radiance error

Figure 3.6 Concluded.

Horizontal temperature gradients of 1.1°K per degree latitude produced temperature errors in the inversion of about 4°K near 3 mb. The lapse rate from 10 mb to 5 mb was increased by the temperature gradients when looking toward colder temperatures. Height errors increased with decreasing pressure due to the constancy of the sign of the temperature error. Geostrophic wind errors were less than 10 per cent of the initial wind and the sign of the error changed with latitude due to the change of horizontal temperature gradients with latitude. Errors in wind shear of nearly 20 per cent occurred for strong wind shear and errors of a factor of two or more occurred for small wind shear.

Random radiance errors may lead to non-random errors in other quantities. The random radiance errors used had a mean of zero and a standard deviation of 0.01 $Wm^{-2}$ $sr^{-1}$. Mean temperature errors for a sounding were usually less than 1°K with temperature errors largest at small pressures, where the radiance error was the largest fraction of the total radiance. Temperature errors were larger again at larger tangent pressure where the atmosphere approaches opacity for the tangential path. Errors in the geostrophic wind usually were less than 10 per cent of the wind. Wind errors increased with decreasing pressure. Errors in the wind shear were often as large as the wind shear itself; this was a result of horizontal temperature differences being of the same magnitude as temperature errors caused by the radiance errors.

The errors in wind and wind shear due to random radiance errors and horizontal temperature gradients indicate that useful wind data can be inferred but wind shear data is questionable.

# CHAPTER IV

## INFERENCE OF TEMPERATURE FROM EXPERIMENTAL RADIANCE DATA

Several measurements of limb radiance profiles have been made in the past few years by Walker et al. (1966), McKee et al. (1968), Whitman et al. (1968), Girard (1970) and Walker (1971). All of these experiments included measurements in the 15μ region of $CO_2$ emission. However, only the measurements of Walker (1971) used a radiometer with sufficient signal to noise ratio to provide radiance data suitable for an inference application. This chapter describes the experimental limb radiance profiles, the meteorological data available near the time and location of the radiance measurements, the inference of temperature from the limb radiance data, and the comparison of inferred temperature with the meteorological data.

### Experimental Radiance Data

An infrared radiometer was included in the instrumentation on an Aerobee rocket launched from White Sands Missile Range, New Mexico at approximately 0530 GMT on February 7, 1970. Apogee for the probe was 145 km. The payload was erected to near the local vertical and was spinning about the vertical axis while an oscillating mirror in the

radiometer scanned the instrument line of sight up and down across the earth's limb. Limb crossings of the line of sight are contained in a circle around the sub-vehicle point. Geographical locations of seven actual limb crossings are illustrated in Figure 4.1. For a fixed rocket vehicle altitude, which is nearly the condition during one scan, the tangent point changes location for different lines of sight and the arrows in Figure 4.1 indicate the direction of movement. A scan from space to earth causes the tangent point to move away from the observer such as in scan numbers 1, 2, 3 and 7. The end points of each scan in Figure 4.1 mark approximate locations where radiance data were measured. Radiance data from each of these seven scans have been provided prior to publication by Walker (1971). An example of the radiance data from scan number 2 is shown in Figure 4.2. These radiance data were observed with an instrument which had a spectral response defined in Figure 4.3. The spectral interval at the 50 per cent values of $\Phi_\nu$ is about 645 $cm^{-1}$ to 707 $cm^{-1}$ which is only 60 per cent of the width of the interval used for examples in Chapter III. An estimate of the standard deviation of the noise level for the radiance data (points) in Figure 4.2 is 0.027 W $m^{-2}$ $sr^{-1}$. A linear smoothing has been applied to the data to produce the solid line which has an estimated standard deviation due to noise of 0.01 W $m^{-2}$ $sr^{-1}$. Smoothed data has been used in all inversions.

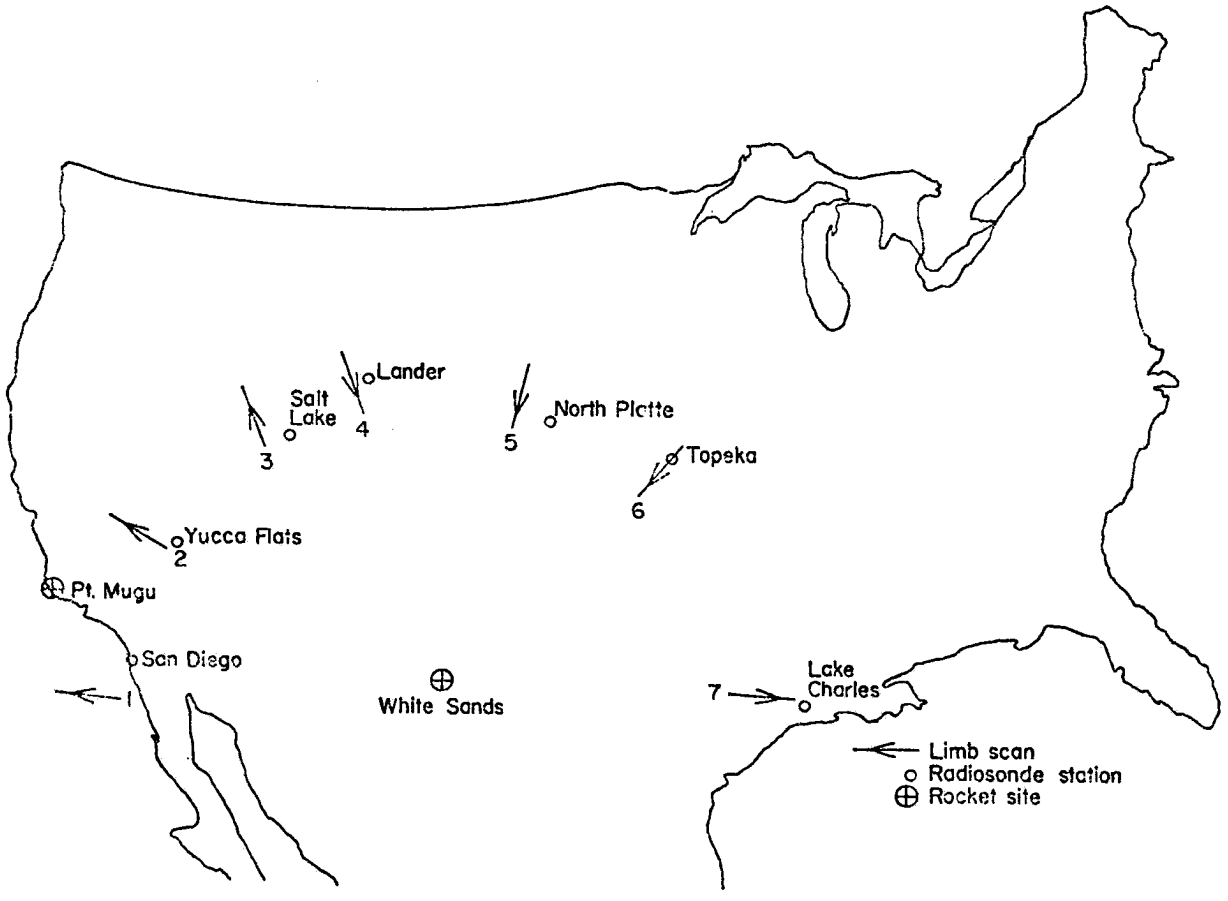


Figure 4.1 Geographic locations of limb radiance scans.

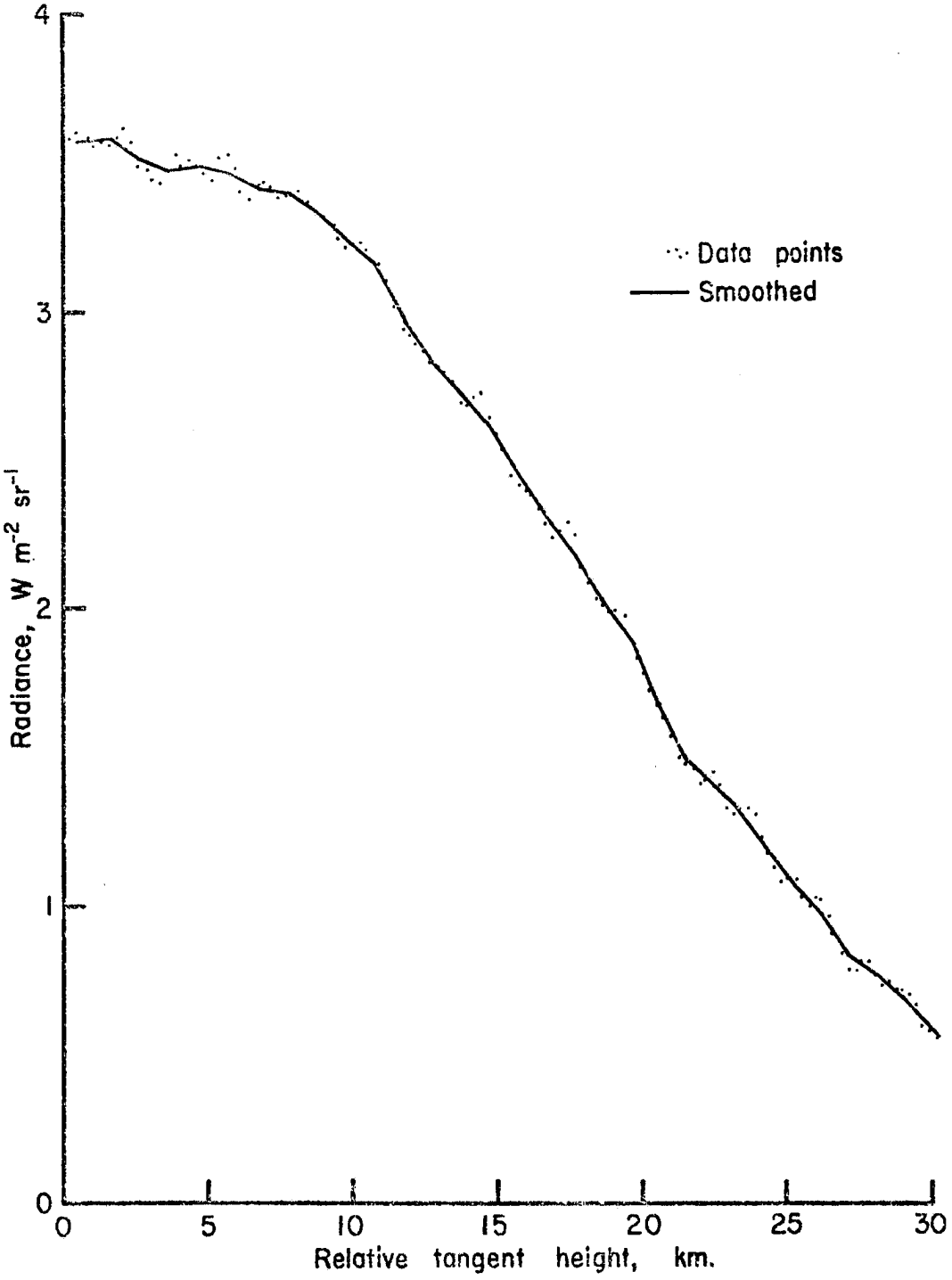


Figure 4.2 Example of radiance data for scan 2.

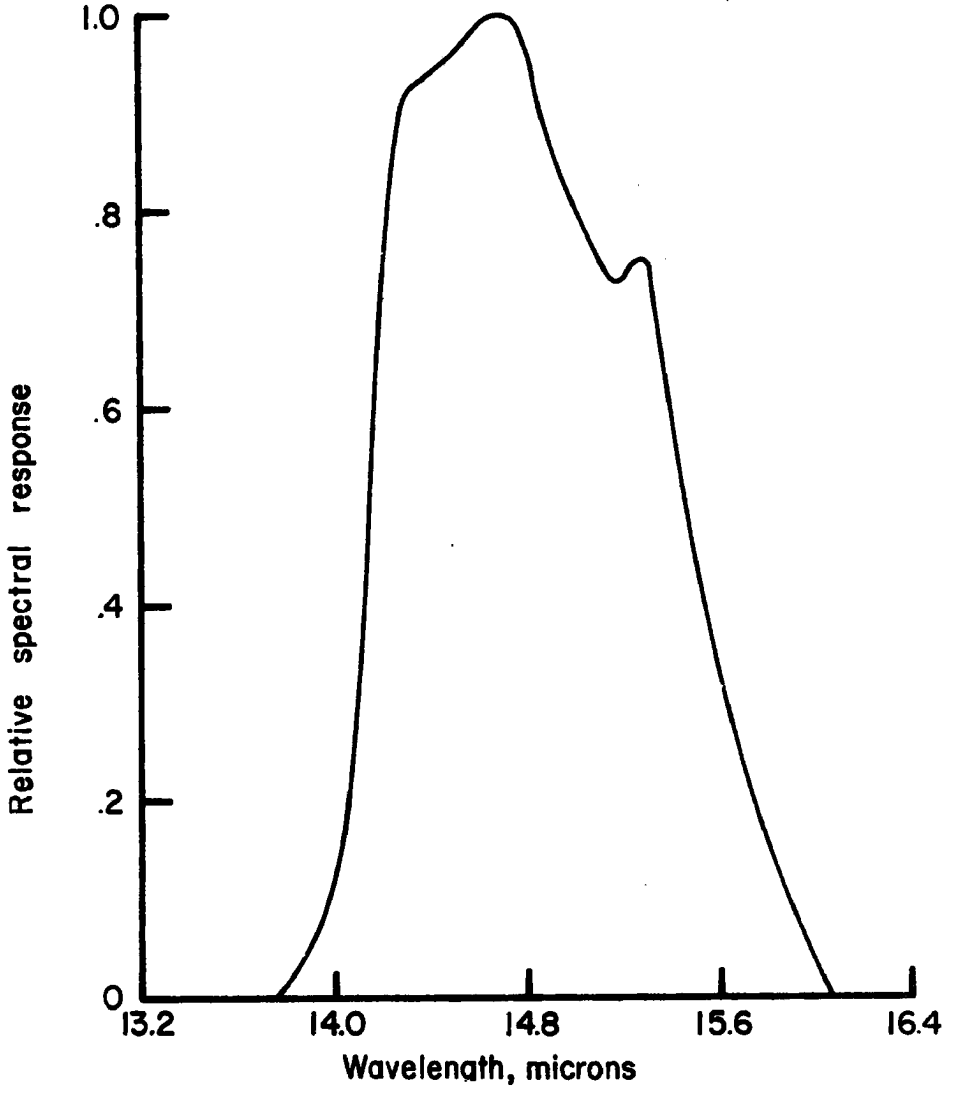


Figure 4.3 Spectral response of radiometer.

Radiance as measured in the experiment and plotted in Figure 4.2 is defined as

$$N_m = \int J_\nu \Phi_\nu d\nu \tag{4.1}$$

where $\Phi_\nu$ is a normalized spectral response of the instrument. The source function, $J_\nu$, is the radiance exiting the top of the atmosphere and is not determined in the experiment. The measured radiance is equal to and derived from the same instrument output voltage as produced by a calibration radiance of

$$N = \int N_\nu(T) \Phi_\nu d\nu \tag{4.2}$$

where $N_\nu(T)$ is the Planck black-body radiance for some temperature.

In the experiment radiance was measured as a function of tangent height. The information needed for the present inference application is the change of tangent height between radiance values which is defined in equation (3.15). Consequently, only the change of tangent height has been used.

Meteorological Data

The meteorological temperature data available for comparison with inferred temperature data include the regular 0000 Z and 1200 Z soundings taken at each station shown in Figure 4.1 and a few rocket soundings. Data from the 500 mb analysis in the troposphere show a long wave or semipermanent trough in the eastern half of the United States which did not change appreciably from 1200 Z on February 6, 1970

to 1200 Z on February 7, 1970. This long wave trough is apparent in the analysis at 100 mb, 50 mb, 30 mb, and 10 mb also. The 50 mb and 10 mb analyses from National Oceanic and Atmospheric Administration (1970) are shown in Figure 4.4. At 50 mb the normal horizontal temperature gradient in the troposphere with colder temperatures to the north has been replaced with warmer temperatures to the north. By 10 mb the gradient with colder temperatures to the north has been reestablished and should continue to the stratopause. Geographical location of the seven limb scans are also depicted on the 50 mb and 10 mb analyses.

Radiosonde data at 0000 Z on February 7, 1970 were taken 5.5 hours prior to the radiance measurements and the 1200 Z data were taken 6.5 hours after the radiance measurements. Only small temperature differences were observed between the two radiosonde measurements and no significant advection of temperature is expected from the analysis. Consequently, the radiosonde data were considered to represent the atmosphere from 50 mb to 10 mb at the time of the radiance measurements. The radiosonde stations used to provide the temperature as a function of pressure up to 10 mb for each limb scan are given in Table 4.1.

Rocketsonde data reported by World Data Center A (1970) have been obtained for Pt. Mugu, California and White Sands, New Mexico for the times nearest to that of the radiance measurements. Pt. Mugu is geographically closest to the location of the radiance measurements. In the time period

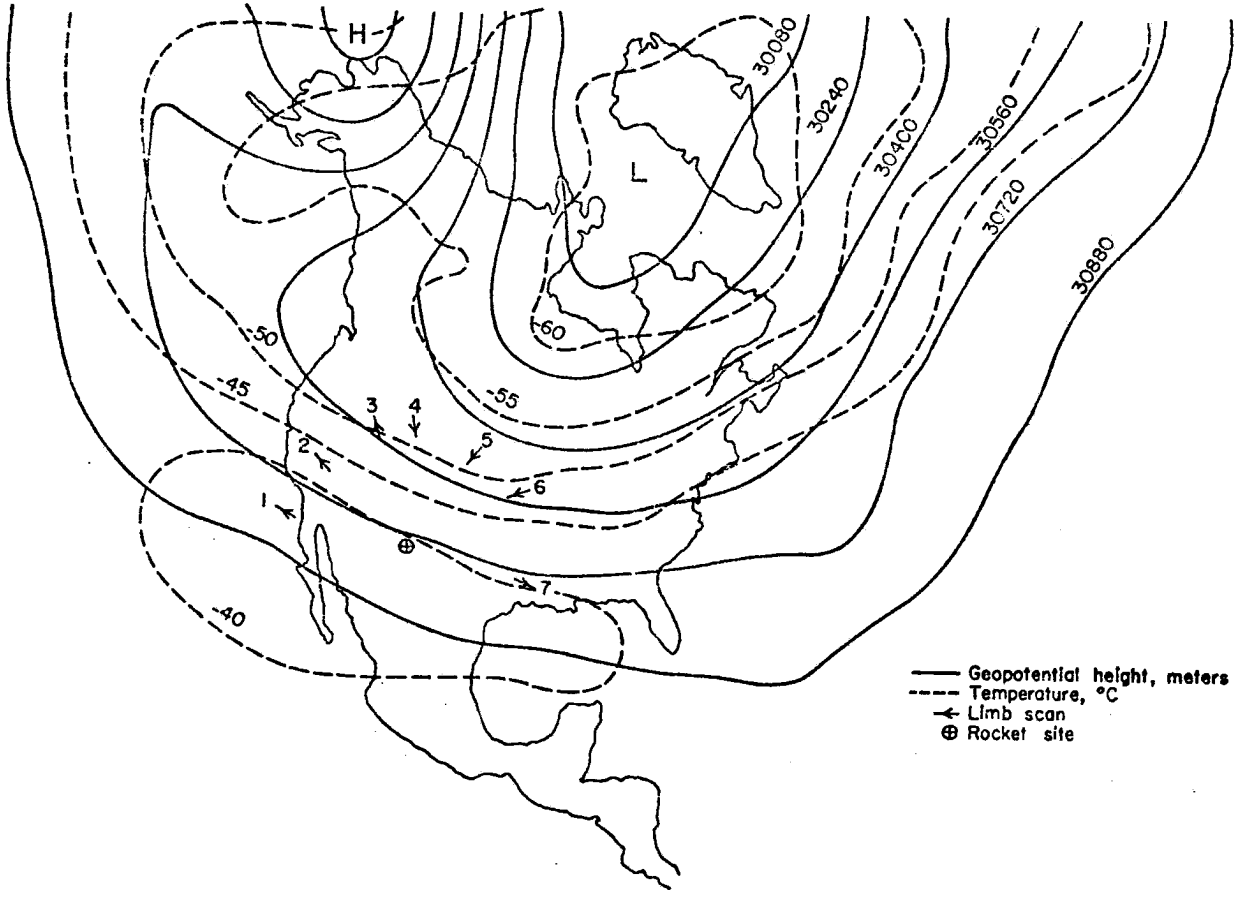


(a) 10mb

Figure 4.4 Stratospheric analysis for February 7, 1970.

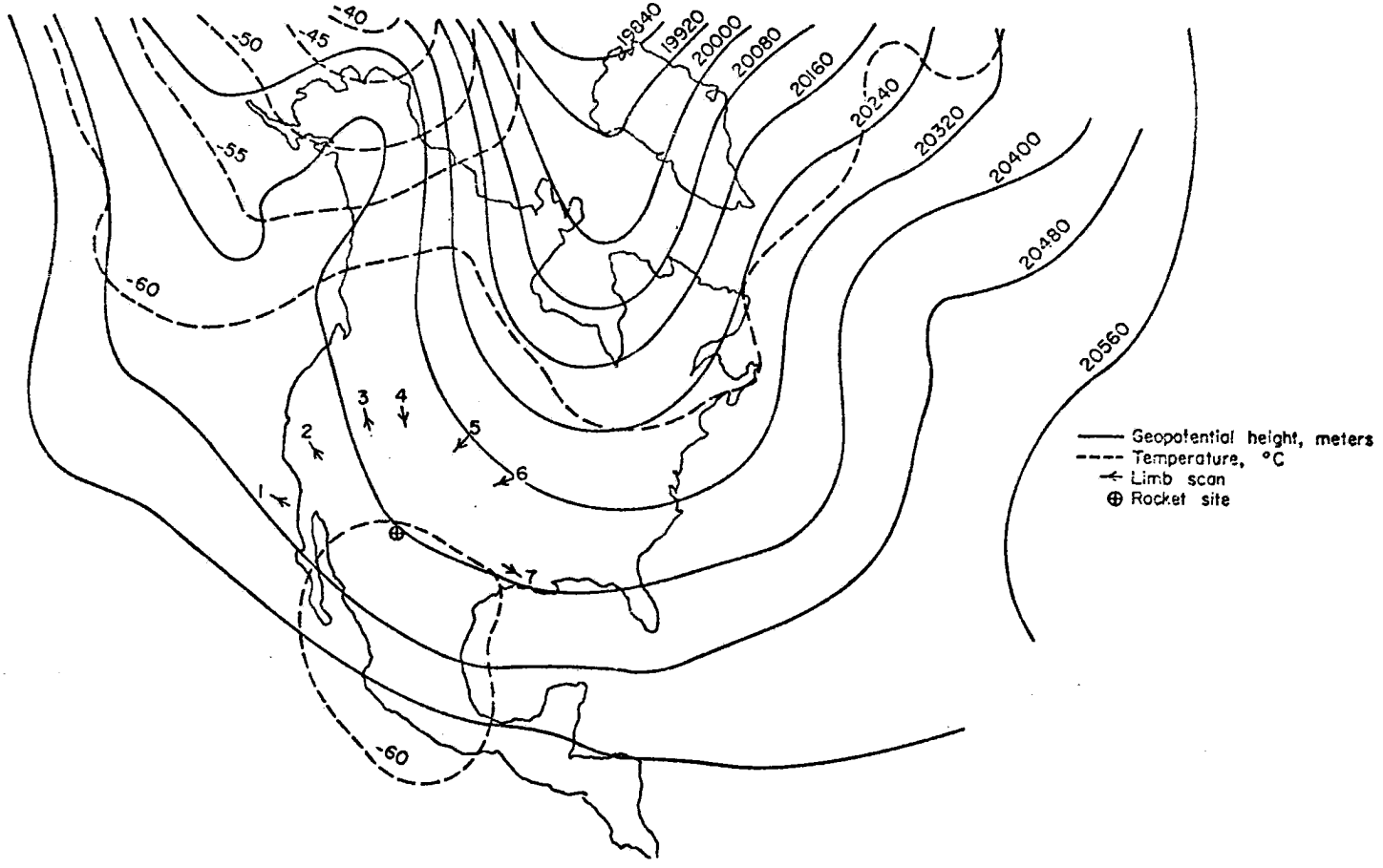


(b) 50mb

Figure 4.4 Concluded.

Table 4.1. Radiosonde stations used with limb radiance scans.

| Scan | Radiosonde Station |
|---|---|
| 1 | San Diago, California |
| 2 | Yucca Flats, Nevada |
| 3 | Salt Lake City, Utah |
| 4 | Lander, Wyoming |
| 5 | North Platte, Nebraska |
| 6 | Topeka, Kansas |
| 7 | Lake Charles, Louisiana |

of February 5, 1970 to February 11, 1970 only two soundings were made which measured temperature. The soundings were at 2106 Z on February 5, 1970 and 2202 Z on February 11, 1970. These are both daytime soundings. Diurnal changes from the time of these soundings to the time of the radiance measurements should occur but the magnitude and phase are not well known. General similarity of the two rocket soundings indicate no large changes have taken place in the atmosphere in the intervening period. A series of rocketsondes were launched at White Sands on February 9, 1970 with five soundings taken between 1706 Z and 2030 Z. An earlier sounding was taken on February 6 at 1900 Z. Again all measurements were taken in the daytime. Variations in measured temperature on February 9 are greater than the change from February 6 to February 9.

Inference of Temperature
from Measured Radiance

The theoretical model developed in Chapter III used a measured radiance in a given spectral interval. Measured radiances provided by Walker (1971) are defined in equation (4.1) which is different from that defined in equation (3.3). Either the measured radiance data or the theoretical technique of inference must be modified in order to use the data. Modification of the inference technique is the easier of the two choices and is described next.

All terms involving measured radiance used in forming radiance errors such as equation (3.6) remain unchanged. The specification of theoretical radiance in equation (3.3) is changed to

$$N_t(P) = -\int\int N_\nu(T)\Phi_\nu d\tau_\nu d\nu \qquad (4.3)$$

which renders $N_t(P)$ consistent with the definition of $N_m$ in equation (4.1). For monochromatic radiance the source function in the definition of $N_m$ in equation (4.1) is actually

$$J_\nu = -\int N_{B_\nu}(T)\, d\tau_\nu \; . \qquad (4.4)$$

As a result of these modified definitions of measured and calculated radiance, the radiance error formed from equations (3.6) for the initial layer and (3.18) for subsequent layers remains unchanged. However the temperature change used in the iteration for the initial layer, equation (3.12), and for subsequent layers, equation (3.19), must be changed to

$$\Delta T_o = - \frac{[N_m(P_o) - N_t(P_o)]T_o^2}{D_2 \nu_a N_{B_{\nu_a}}(T_o) \int_{\nu_l}^{\nu_u} \int_{\tau_1}^{} \Phi_\nu d\tau_\nu d\nu} \qquad (4.5)$$

and

$$\Delta T_i = - \frac{[N_m(P_i) - N_t(P_i)]T_i^2}{D_2 \nu_a N_{B_{\nu_a}}(T_i) \int_{\nu_l}^{\nu_u} \int_{\tau_3}^{\tau_4} \Phi_\nu d\tau_\nu d\nu} . \qquad (4.6)$$

With these definitions the inference of temperature proceeds as described in Chapter III.

The derivation of the inference technique left the tangent pressure of the initial level an arbitrary constant. One of the methods suggested for determining the initial pressure was to match the inferred temperature structure with the radiosonde measurements at the lower boundary. In the present example radiosonde data were available close in space and time for each limb scan so they were used to determine the initial pressure. Both temperature and lapse rate from 10 mb to about 40 mb were used to define the best fit at the lower boundary.

Sensitivity of the inference technique to radiance errors for the experimental radiance data is shown in Figure 4.5. A radiance error of 0.01 W $m^{-2}$ $sr^{-1}$ introduced in the tangent layer caused the temperature error shown. At 0.6 mb where the atmosphere is quite transparent and radiances are small the error was 3.4° K. At larger pressures the radiance increases and the sensitivity decreases to less than

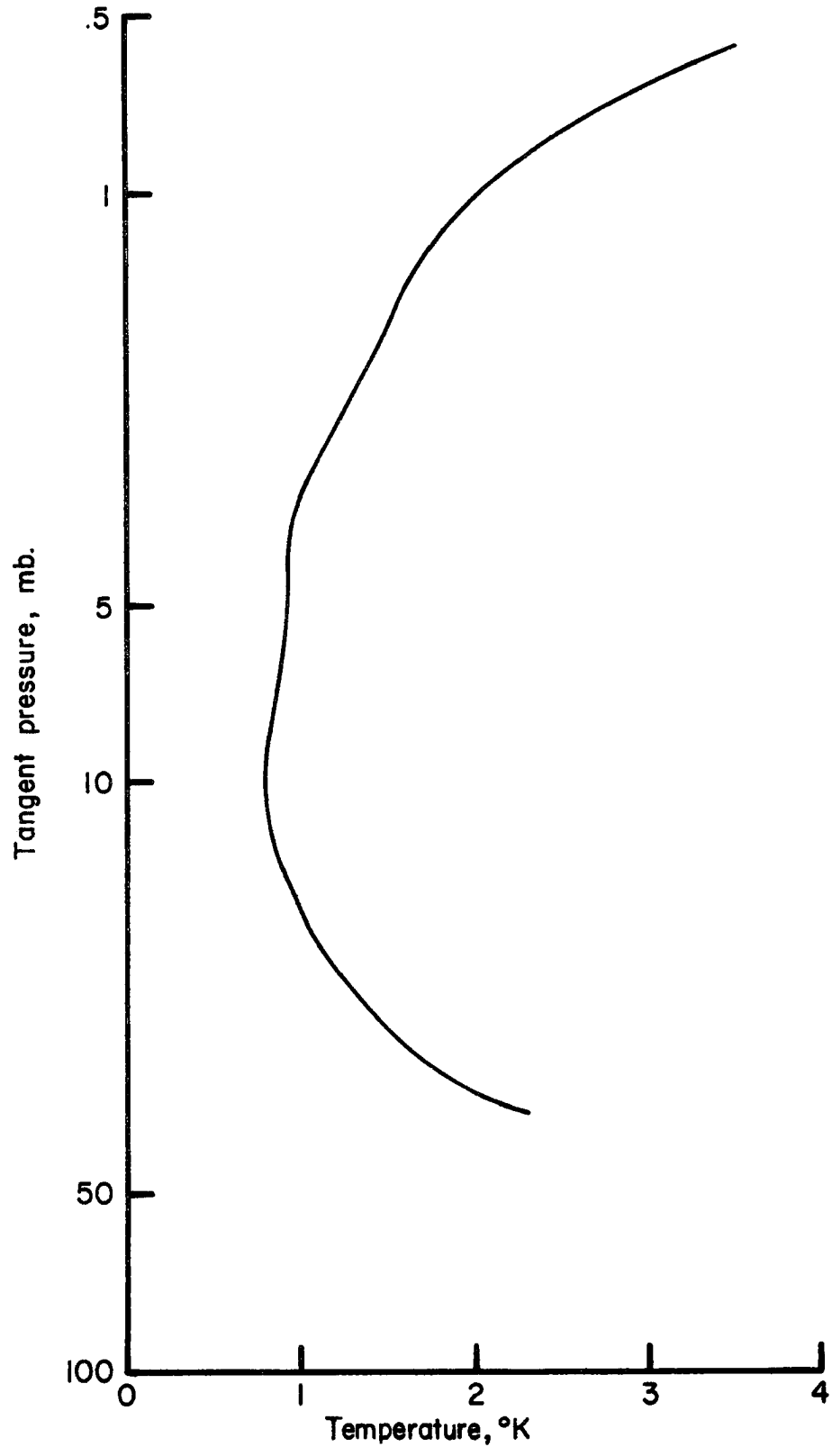


Figure 4.5 Temperature error for a radiance error of 0.01 W $m^{-2}$ $sr^{-1}$.

1° K. For tangent pressures larger than 17 mb the atmosphere tends toward opacity and the error again becomes larger than 1° K. Since the estimated standard deviation of the noise of the experimental data is 0.01 W $m^{-2}$ $sr^{-1}$, 67 per cent of the radiance values should have an error less than 0.01 W $m^{-2}$ $sr^{-1}$.

## Discussion of Inferred Temperature Structure

The temperature structure inferred from the seven limb radiance scans shown in Figure 4.1 are shown in Figure 4.6. Results of choosing the initial pressure for the inference so that the temperature structure matches the radiosonde data of the lower boundary are illustrated. Inferred temperatures are warmer than radiosonde temperatures at 10 mb but agree within the noise in the inferred data by 30 mb. Muench (1971) has shown radiosonde temperature measurements tend to have a systematic error which increases with height above 25 km causing observed temperatures to be too low. Figure 4.6 indicates the discrepancy between inferred and radiosonde temperatures are of the same nature as Muench (1971) has described. Horizontal temperature gradients examined in Appendix B tend to produce a larger lapse rate at 10 mb also; however, the temperature gradients evident in Figure 4.4 are not large enough to account for all of the difference noted in Figure 4.6.

Much of the detailed structure evident in the inferred temperatures is due to the random radiance noise of the

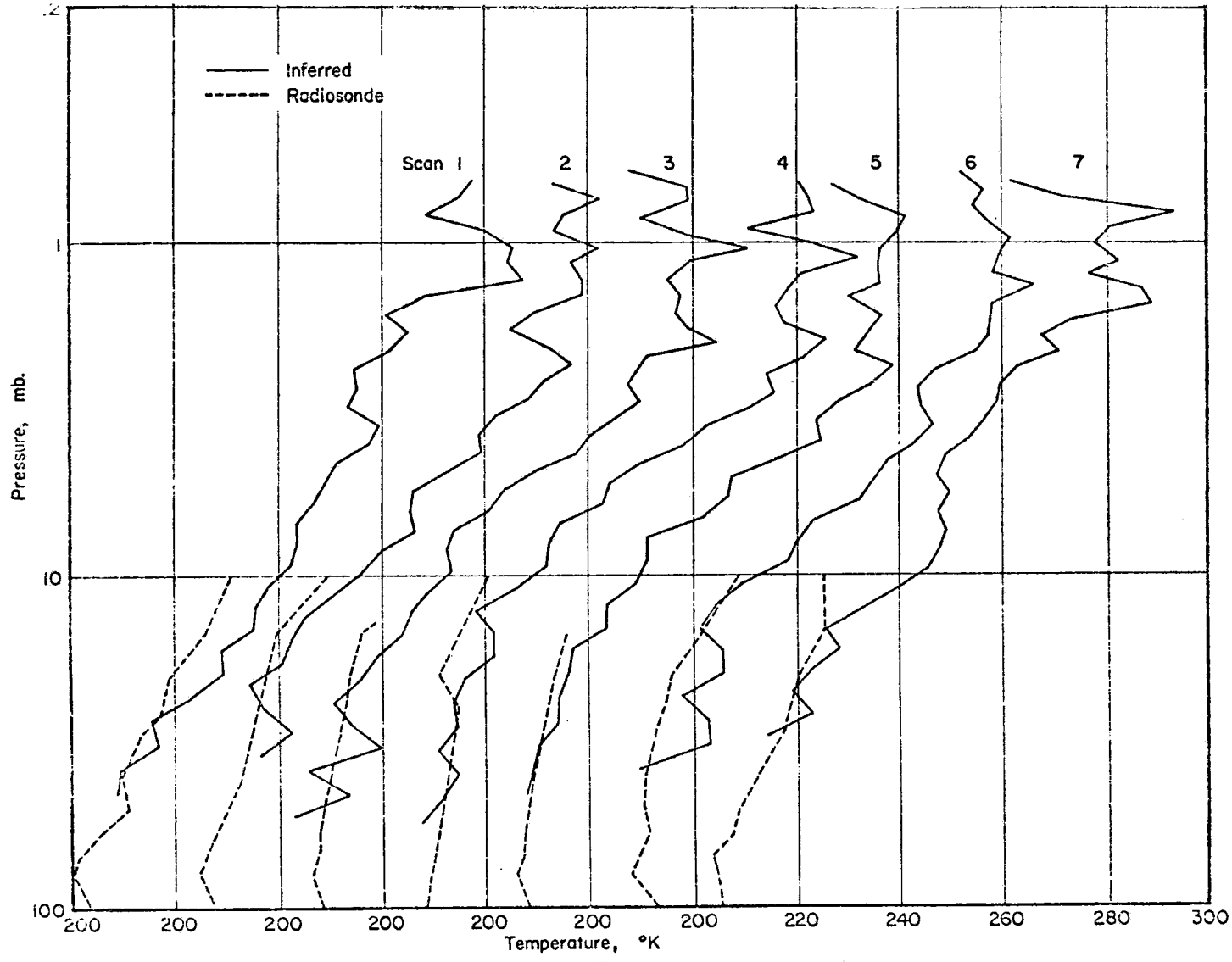


Figure 4.6 Inferred temperature structure.

measuring instrument. Separation of actual temperature structure from effects of random radiance noise can not be accomplished with just one inferred temperature profile. Comparison of two of the inferred temperature profiles which are close together geographically affords an opportunity to separate structure from noise since noise is not repeatable. Figure 4.7 shows a direct comparison of temperature from scans 3 and 4 which are about 400 km apart. The vertical temperature structure from 0.8 mb to 3 mb is nearly identical and is considered real. Thirteen radiance values were used between these pressures and the probability of random errors being so similar is extremely small. In fact the probability that the two random errors would have the same sign thirteen times in a row is $(1/2)^{13}$. The structure at pressures larger than 10 mb appears to be due to random noise as very little correlation is evident. The large decrease in temperature near 1 mb amounts to 20° K and has a lapse rate of 11° K $km^{-1}$ which is just slightly greater than dry adiabatic. Detailed structure in Figure 4.7 indicates a vertical resolution of about 2 km for the inferred data.

In Figure 4.6 the lapse rates from 10 mb to 2 mb are quite similar for scans 2, 3, 4, 5 and 6 but scans 1 and 7 are noticeably different. Examination of the 10 mb analysis in Figure 4.4 reveals scans 1 and 7 are in similar locations relative to the large trough but are quite different than scans 3 and 4. Temperatures from scans 1 and 7 are compared in Figure 4.8. Temperatures and lapse rate are similar

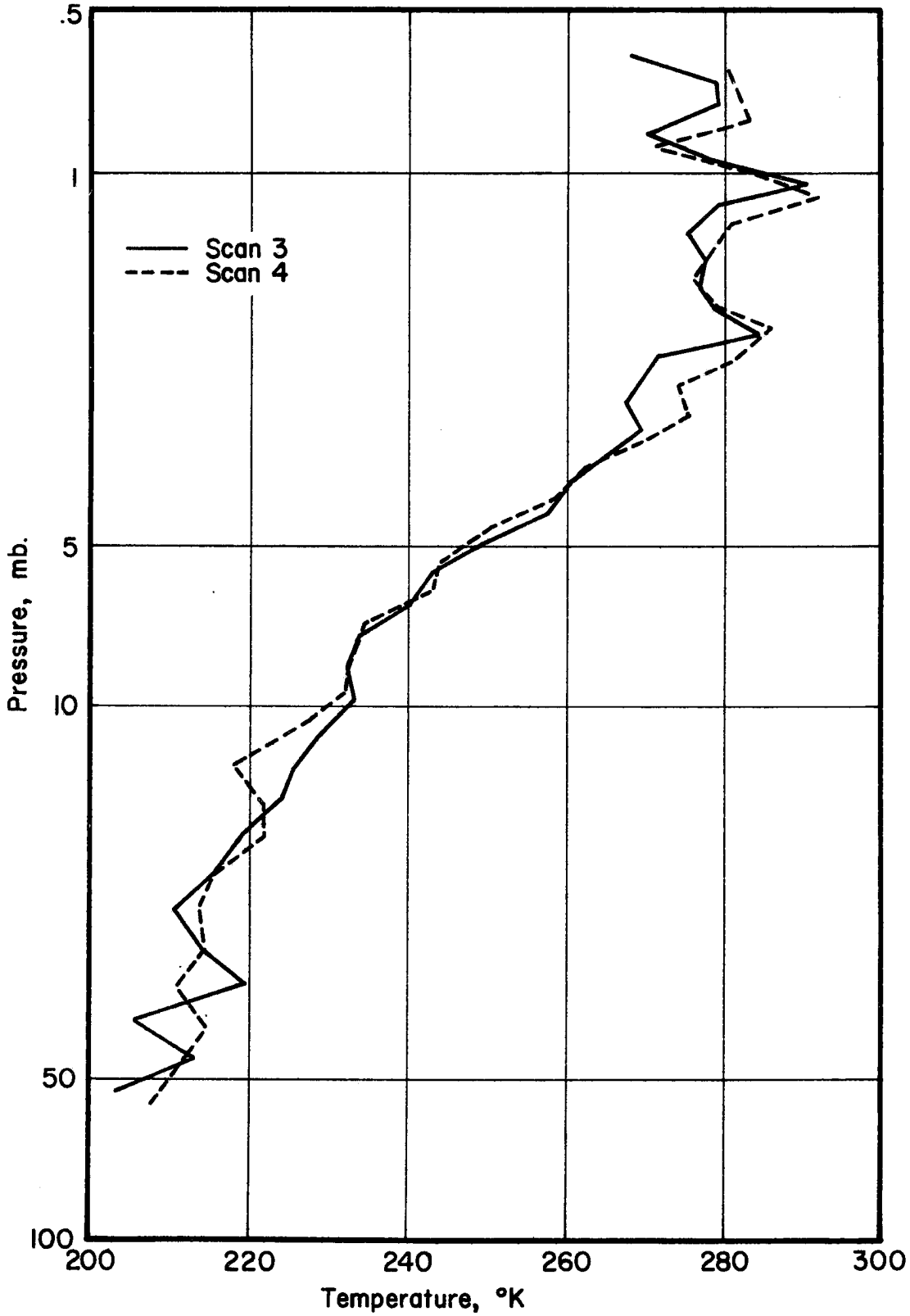


Figure 4.7 Comparison of temperature from scans 3 and 4.

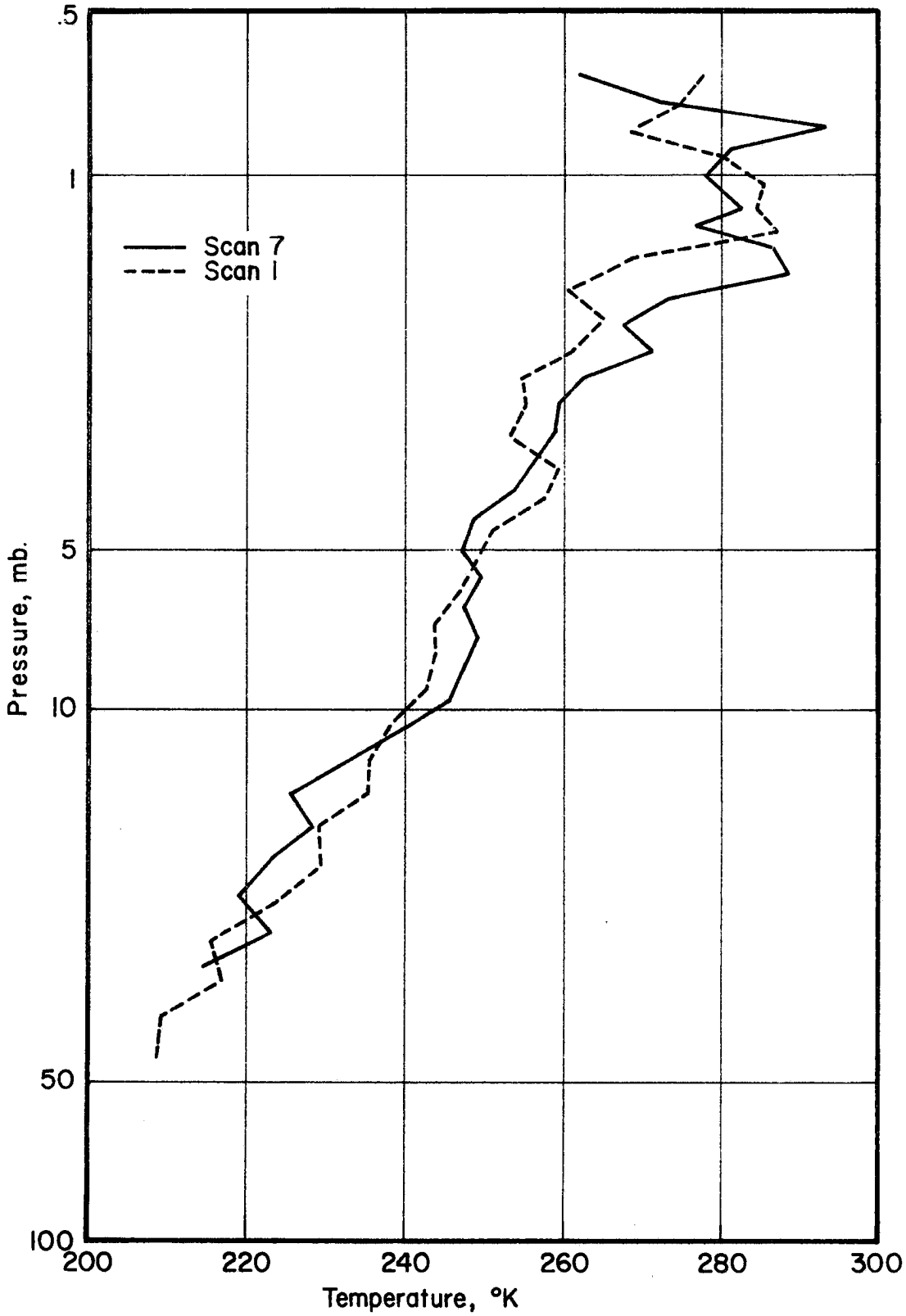


Figure 4.8 Comparison of temperature from scans 1 and 7.

throughout the profile. Temperature of scans 1 and 7 at 10 mb are the warmest of all scans which is consistant with the 10 mb analysis of Figure 4.4.

Scans 1 and 2 are located with the rocket site at Pt. Mugu, California between them. Two soundings on February 5 are compared with temperatures from scans 1 and 2 in Figure 4.9. Differences between the two rocket soundings which are six days apart in time are not significantly smaller than the differences between the rocket determined temperatures and the inferred temperatures. The inferred profiles certainly appear reasonable for locations on either side of the rocket data as the rocket data are between the inferred temperatures at most pressures. Diurnal temperature change is not evident even though the rocket data are near mid-day and the inferred data at night. Diurnal change should be the largest in the vicinity of 1 mb but a summary of diurnal effects by Gille (1968) indicates considerable uncertainty about the local time of temperature maximum which varied from noon to early evening for theory and from noon to near midnight for observations. Rocket data from White Sands, New Mexico also have an average lapse rate from 10 mb to 2 mb more like scans 1 and 7 than the others. One of the four White Sands soundings has a distinct warm bulge at pressures a little smaller than 10 mb similar to that of scan 7.

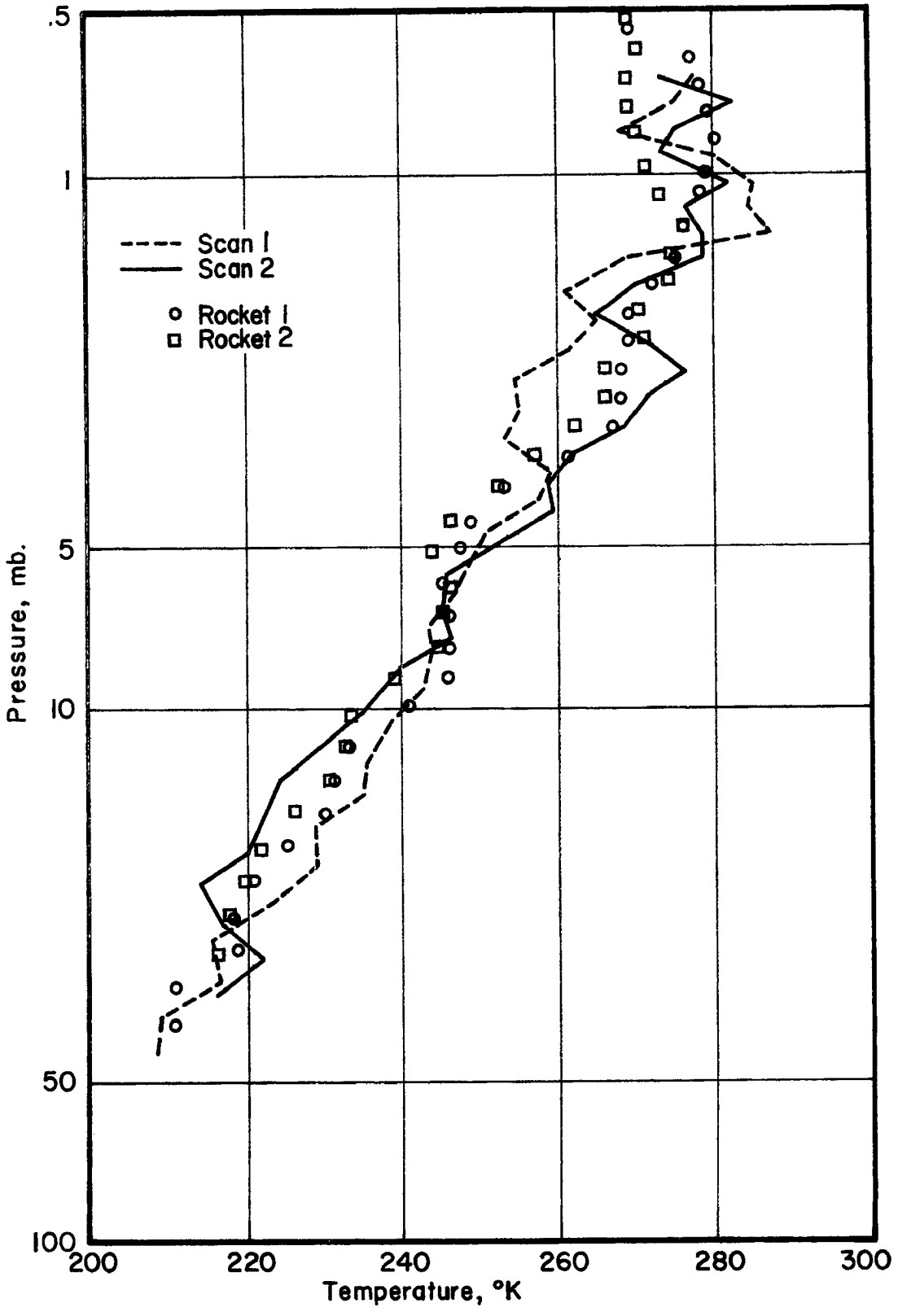


Figure 4.9 Comparison of inferred temperature with rocket data.

# CHAPTER V

## CONCLUDING REMARKS

Techniques have been developed to infer stratospheric temperature and water vapor mixing ratio structure from limb radiance profiles. These techniques have eliminated the need for precise orientation information and only require the easily obtained vertical scan rate of the optical line of sight. Application of the technique is feasible for any atmosphere where clouds do not interfere. Examples of the sensitivity of the inferred temperatures to realistic bias, scale, and random radiance errors for the 615 $cm^{-1}$ to 715 $cm^{-1}$ spectral interval of $CO_2$ emission indicate the technique is not seriously affected by such errors in the pressure range of 1 mb to 100 mb. Examples of the sensitivity of the inferred water vapor mixing ratios to realistic bias, scale, and random radiance errors for the 205 $cm^{-1}$ to 295 $cm^{-1}$ spectral interval of water vapor emission indicate the technique should be useful for determining mixing ratio from 3 mb to at least 100 mb.

The technique to infer stratospheric temperature was applied to a set of seven limb radiance profiles measured in a winter atmosphere in February for a spectral interval of 645 $cm^{-1}$ to 707 $cm^{-1}$. Inferred temperature structure is

similar to available rocket sounding data. Horizontal variation of temperature at the 10 mb and 30 mb surfaces agree with radiosonde data; however the inferred temperatures and lapse rates have systematically warmer temperature at 10 mb and slightly more increase of temperature from 30 mb to 10 mb than do radiosonde data. Two of the inferred temperature profiles provide an excellent example in which two measurements are sufficiently alike to separate real vertical temperature structure from effects of random radiance noise. Vertical resolution is about 2 km and the largest lapse rate noted is near dry adiabatic.

Examples of the effects of the propagation of errors due to horizontal temperature gradients and random radiance errors in the 615 $cm^{-1}$ to 715 $cm^{-1}$ spectral interval on inferred temperature, geopotential height, geostrophic wind, and wind shear were given (Appendix B). Horizontal temperature gradients of 1.1° K $deg.^{-1}$ produced temperature errors in the inversion of about 4° K near 3 mb. The lapse rate from 10 mb to 5 mb was increased by the temperature gradients. Height errors increased with decreasing pressure due to the constancy of the sign of the temperature error. Wind errors were less than 10 per cent of the initial wind and the sign of the error changed with latitude due to the change of horizontal temperature gradients with latitude. Errors in wind shear up to near 20 per cent occurred for strong wind shear with errors of a factor of two or more for small wind shear.

Random radiance errors may lead to non-random errors in other quantities. The random radiance errors used had a mean equal to zero and standard deviation of 0.01 W $m^{-2}$ $sr^{-1}$. Mean temperature errors were less than 1° K with temperature errors largest at small pressures, where the radiance error was the largest fraction of the actual radiance. Temperature errors were larger again at large pressures, where the atmosphere approaches opacity in the 615 $cm^{-1}$ to 715 $cm^{-1}$ interval. Errors in the geostrophic wind field were usually less than 10 per cent. Wind errors increased with decreasing pressure. Errors in the wind shear were often as large as the wind shear itself; this was a result of horizontal temperature differences being of the same magnitude as temperature errors caused by the radiance errors.

The errors in wind and wind shear indicate that useful wind data can be inferred but wind shear data is questionable.

# LITERATURE CITED

## LITERATURE CITED


Bates, Jerry C., David S. Hansen, Fred B. House, Robert O'B. Carpenter and John C. Gille, 1967: The synthesis of 15 infrared horizon radiance profiles from meteorological data inputs. *NASA CR-724.*

Beyers, N. J. and B. T. Miers, 1965: Diurnal temperature change in the atmosphere between 30 and 60 km over White Sands Missile Range. *Journal of the Atmospheric Sciences,* 22, 3, 262-266.

Bolin, Bert and Walter Bischof, 1970: Variations of the $CO_2$ content of the atmosphere in the northern hemisphere. *Tellus,* 22, 4, 431-442.

Burch, D. E., E. B. Singleton and D. Williams, 1962a: Absorption line broadening in the infrared. *Applied Optics,* 1, 3, 359-363.

_____, D. A. Gryrnak and D. Williams, 1962b: Total absorptance of carbon dioxide in the infrared. *Applied Optics,* 1, 6, 759-765.

Burn, J. W., W. G. Uplinger and P. P. Morris, 1967: Earth limb radiance profiles for the 15-micron carbon dioxide band--data computed by month for every 10 degrees of latitude in the northern hemisphere. LMSC-677318, Locheed Missiles and Space Co.

_____, and W. G. Uplinger, 1970: The determination of atmospheric temperature profiles from planetary limb radiance profiles. *NASA CR-1513.*

Chahine, Moustafa T., 1968: Determination of the temperature profile in an atmosphere from its outgoing radiance. *Journal of the Optical Society of America,* 58, 1634-1637.

Conrath, Barney J., 1969: On the estimation of relative humidity profiles from medium-resolution spectra obtained from a satellite. *Journal of Geophysical Research,* 74, 3347-3361.

Curtis, A. R., 1952: Discussion of a statistical model for water vapor absorption. *Quarterly Journal of the Royal Meteorological Society,* 78, 638-640.

Davis, Richard E., 1969: A limb radiance calculation approach for model atmospheres containing horizontal gradients of temperature and pressure. *NASA-TN-D-5495.*

Drayson, S. Roland, 1966: Atmospheric transmission in the $CO_2$ bands between 12 and 18. *Applied Optics,* 5, 385-391.

Elsasser, W. M., 1942: *Heat Transfer by Infrared Radiation in the Atmosphere.* Harvard Meteorological Studies, No. 6, Cambridge, Harvard University Press.

_____, and M. F. Culbertson, 1960: Atmospheric radiation tables. *Meteorological Monographs,* Vol. 4, No. 23, 1-43.

Environmental Science Services Administration, National Aeronautics and Space Administration and U. S. Air Force, 1966: U. S. standard atmosphere supplements. U. S. Government Printing Office, Washington, D.C.

Gille, J. C., 1968: On the possibility of estimating diurnal temperature variation at the stratopause from horizon radiance profiles. *Journal of Geophysical Research,* 73, 6, 1863-1868.

_____, and Frederick House, 1971: On the inversion of limb radiance measurements: I. Temperature and thickness. *Journal of the Atmospheric Sciences,* 28, 7.

Girard, A., 1970: Profils experimentaux de l'horizon. *Applied Optics,* 9, 4, 903-912.

Godson, W. L., 1953: The evaluation of infrared radiative fluxes due to atmospheric water vapor. *Quarterly Journal of the Royal Meteorological Society,* 78, 165-169.

Goody, R. M., 1952: A statistical model for water vapor absorption. *Quarterly Journal of the Royal Meteorological Society,* 78, 165-169.

_____, 1964: *Atmospheric Radiation.* Oxford University Press, London.

Gordon, H. R. and T. K. McCubbin, 1965: The 15-micron bands of $C^{12}O_2^{16}$. *Journal of Molecular Spectroscopy,* 18, 73-82.

Haltiner, George J. and Frank L. Martin, 1957: *Dynamical and Physical Meteorology.* McGraw-Hill Book Company, New York, New York.

Hanel, R. A., W. R. Bandeen and B. J. Conrath, 1963: The infrared horizon of the planet earth. *Journal of the Atmospheric Sciences*, 20, 2, 73-86.

Houghton, J. T. and S. D. Smith, 1970: Remote sounding of atmospheric temperature from satellites, I. Introduction. *Proceedings of the Royal Society of London*, A., 320, 23-33.

House, Frederick B. and G. Ohring, 1969: Inference of stratospheric temperature and moisture profiles from observations of the infrared horizon. *NASA CR-1419*.

Howard, J. N., D. E. Burch and Dudley Williams, 1956: Infrared transmission of synthetic atmospheres. *Journal of the Optical Society of America*
I. Instrumentation, 186-190,
II. Absorption by carbon dioxide, 237-241,
III. Absorption by water vapor, 242-245,
IV. Application of theoretical band models, 334-338,
V. Absorption laws for overlapping bands, 452-455.

Kaplan, L. D., 1959: Inference of atmospheric structure from remote radiation measurements. *Journal of the Optical Society of America*, 49, 10, 1004-1007.

King, Jean I. F., 1963: Meteorological inferences from satellite radiometry. *Journal of the Atmospheric Sciences*, 20, 245-250.

_____, 1964: Inversion by slabs of varying thickness. *Journal of the Atmospheric Sciences*, 21, 324-326.

Kondratiev, K. Y. and K. E. Yakusherskaya, 1963: Angular distribution of the outgoing thermal radiation in the different regions of the spectrum. First International Symposium on Rocket and Satellite Meteorology, H. Wexler and J. E. Caskey, Jr., eds., John Wiley & Sons, Inc., pp. 254-277.

Kuhn, P. M. and S. K. Cox, 1967: Radiometric inference of stratospheric water vapor. *Journal of Applied Meteorology*, 6, 1, 142-149.

Kunde, Virgil G., 1967: Theoretical computations of the outgoing infrared radiance from a planetary atmosphere. *NASA-TN-D-4045*.

Lindzen, R. S., 1967: Thermally driven diurnal tide in the atmosphere. *Quarterly Journal of the Royal Meteorological Society*, 93, 18-42.

Madden, Robert P., 1961: A high resolution study of $CO_2$ absorption spectra between 15 and 18 microns. *Journal of Chemical Physics*, 35, 6, 2083-2097.

Manabe, Syukuro and Barrie G. Hunt, 1968: Experiments with a stratospheric general circulation model: I. Radiative and dynamic aspects. *Monthly Weather Review*, 96, 8, 477-502.

Mastenbrook, H. J., 1968: Water vapor distribution in the stratosphere and high troposphere. *Journal of the Atmospheric Sciences*, 25, 2, 299-341.

McKee, Thomas B., Ruth I. Whitman and Richard E. Davis, 1968: Infrared horizon profiles for summer conditions from project scanner. *NASA-TN-D-4741*.

_____, _____ and Jules J. Lambiotte, 1969a: A technique to infer atmospheric temperature from horizon radiance profiles. *NASA-TN-D-5068*.

_____, _____ and _____, 1969b: A technique to infer atmospheric water vapor mixing ratio from measured horizon radiance profiles. *NASA-TN-D-5252*.

_____, 1970: Inference of temperature and water vapor structure in the stratosphere from limb radiance profiles. *NASA-TM-X-1943*.

Muench, H. Stuart, 1971: Temperature measurements in the 30 to 40 kilometer region. *Monthly Weather Review*, 99, 9, 158-161.

Murcray, D. G., T. G. Kyle and W. J. Williams, 1969: Distribution of water vapor in the stratosphere as derived from setting sun absorption data. *Journal of Geophysical Research*, 74, 23, 5369-5373.

National Aeronautics and Space Administration, United States Air Force and United States Weather Bureau, 1962: U.S. standard atmosphere, 1962. U. S. Government Printing Office, Washington, D.C.

National Oceanic and Atmospheric Administration, 1970: Daily series, synoptic weather maps: part II. northern hemispheric data tabulations, February, 1970. National Climatic Center, Asheville, North Carolina.

Neporent, B. S., M. S. Kiscleva, A. G. Makogonenko and V. I. Shlyakhov, 1967: Determination of moisture in the atmosphere from absorption of solar radiation. *Applied Optics*, 6, 11, 1845-1850.

Palmer, C. H., 1957: Long path water vapor spectra with pressure broadening. *Journal of the Optical Society of America*, 47,
I. 20 to 31.7μ, 1024-1027,
II. 29 to 40μ, 1028-1031.

_____, 1960: Experimental transmission functions for the pure rotation band of water vapor. *Journal of the Optical Society of America*, 50, 12, 1232-1242.

Pick, D. R. and J. T. Houghtan, 1969: Measurements of atmospheric infrared emission with a balloon-borne multifilter radiometer. *Quarterly Journal of the Royal Meteorological Society*, 95, 535-543.

Plass, G. N., 1958: Models for spectral band absorption. *Journal of the Optical Society of America*, 48, 690-703.

_____, 1963: Infrared transmission studies, Vol. V: transmittance table for slant paths in the atmosphere. Final Report No. SSD-TDR-62-126, Aeronautical Division, Ford Motor Company.

Prabhakara, C., B. J. Conrath, R. A. Hanel and E. J. Williamson, 1970: Remote sensing of a atmospheric ozone using the 9.6 band. *Journal of the Atmospheric Sciences*, 27, 4, 689-697.

Reichle, Henry George, Jr., 1969: The effect of several infrared transparent broadening gases on the absorption of infrared radiation in the 15 m band of carbon dioxide. University of Michigan Report 05863-17-T.

Reiter, E. R., 1971: Atmospheric transport processes, part 2: chemical tracers. U. S. Atomic Energy Commission, Division of Technical Information.

Rodgers, C. D., 1970: Remote sounding of the atmospheric temperature profile in the presence of cloud. *Quarterly Journal of the Royal Meteorological Society*, 96, October.

Russell, James Madison III, 1970: The measurement of atmospheric ozone using satellite infrared observations in the 9.6 m band. University of Michigan Report 03635-1-T.

Scherhag, Richard, 1952: Die explosionsortigen stratosphärenerwarmungen des spätwinters 1951/1952. *Berichte der Deutchen Wetterdienstes U. S. Zone*, 38, 51-63.

Sissenwine, N., D. D. Grantham and H. A. Salmela, 1968: Mid-latitude humidity to 32km. *Journal of the Atmospheric Sciences*, 25, 6, 1129-1140.

Smith, William L., 1967: An iterative method for deducing tropospheric temperature and moisture profiles from satellite radiation measurements. *Monthly Weather Review*, 95, 363-369.

_____, 1970: Iterative solution of the radiative transfer equation for the temperature and absorping gas profile of an atmosphere. *Applied Optics*, 9, 9, 1993-1999.

Stull, V. R., P. J. Wyatt and G. N. Plass, 1962: Infrared transmission studies, Vol. III: the infrared absorption of carbon dioxide. Report No. SSD-TDR-62-127, Aeronautical Division, Ford Motor Company.

_____, _____ and _____, 1964: The infrared transmittance of carbon dioxide. *Applied Optics*, 3, 2, 243-254.

Stauffer, Fredric R. and Thomas E. Walsh, 1966: Transmittance of water vapor-14 to 20 microns. *Journal of the Optical Society of America*, 56, 401-405.

Twomey, S., 1966: Indirect measurements of atmospheric temperature profiles from satellites: I. mathematical aspects of the inversion problem. *Monthly Weather Review*, 94, 351-361.

Walker, R. G., C. V. Cunniff and A. P. D'agati, 1966: Measurement of the infrared horizon of the earth. AFCRL-66-631, Environmental Research Paper No. 223, Air Force Cambridge Research Laboratories, L. G. Hanscomb Field, Bedford, Mass.

_____, 1971: Private communication.

Walsh, T. M., Jean C. Keating and Dwayne E. Hinton, 1968: Attitude determination of spin-stabilized project scanner spacecraft. *NASA-TN-D-4740*.

Wark, D. Q., J. Alishouse and G. Yamamoto, 1964: Variation of the infrared spectral radiance near the limb of the earth. *Applied Optics*, 3, 2, 221-227.

_____ and H. E. Fleming, 1966: Indirect measurements of atmospheric temperature profiles from satellites: I. Introduction. *Monthly Weather Review*, 94, 351-361.

_____, 1970: SIRS: An experiment to measure the free air temperature from a satellite. *Applied Optics*, 9, 8, 1761-1766.

Webb, Willis L., 1966: *Structure of the Stratosphere and Mesosphere*. Academic Press, New York.

_____, ed., 1969: *Stratospheric Circulation*. Academic Press, New York.

Whitman, Ruth I., Thomas B. McKee and Richard E. Davis, 1968: Infrared horizon profiles for winter conditions from project scanner. *NASA-TN-D-4905*.

_____, 1971: Effects of three transmission models in the rotational water vapor band on radiance calculations and constituent inferences. *NASA-TN-D-6112*.

Wolk, M., 1967: Strength of pressure-broadened $CO_2$ at 15 microns by digital integration of spectra. *Journal of Quantitative Spectroscopy and Radiative Transfer*, 7, 1, 1-5.

World Data Center A, 1971: Data report high altitude meteorological data, Vol. 7, No. 2, National Weather Records Center, Asheville, North Carolina.

Wyatt, Philip J., V. Robert Stull and Gilbert N. Plass, 1962: Quasi-random model of band absorption. *Journal of the Optical Society of America*, 52, 1209-1217.

Yamamoto, G. and M. Tanaka, 1967: Estimation of water vapor distribution in the atmosphere from satellite measurements. *Application Satellites*, Michal Lunc ed., Gordon and Breach, Inc., New York.

# APPENDIX A

# APPENDIX A

## TRANSMITTANCE OF CARBON DIOXIDE AND WATER VAPOR

Inference of any atmospheric property from measured emitted radiation depends critically on the ability to calculate the transmittance in the spectral region of interest given the distribution of temperature, pressure, and mixing ratio of the gas. The major assumption made in calculating limb radiance profiles (Chapter II) and inference of temperature and water vapor (Chapter III) is that the change of transmittance along a specified path in the atmosphere is known or can be calculated accurately. Because of the critical nature of transmittance determination, a descriptive review follows of the applicable experimental and theoretical work concerning the vibration-rotation bands of $CO_2$ in the 15μ region and the rotational bands of $H_2O$ vapor (not liquid water) at wave lengths longer than 20μ. The present need to calculate transmittance for tangential views of the stratosphere involves long path lengths at low pressure. This condition is never obtainable in experimental measurements; thus an analytical model is immediately necessary.

### Experimental Measurements

The vibration-rotation bands of $CO_2$ in the 15μ extend over the range of about 12μ (833.333 $cm^{-1}$) to 18μ (555.556 $cm^{-1}$). The band center for the fundamental band of $C^{12}\ O^{16}\ O^{16}$ is at 667.379 $cm^{-1}$ (Gordon and McCubbin,

1965) which is 14.984μ. Fourteen other overtone and combination bands are in the region and have an integrated intensity of about 10 per cent of the fundamental band. Several isotopic species of $CO_2$ are present in the atmosphere and their relative amounts were given by Goody (1964) as $C^{12}\ O^{16}\ O^{16}$ (98.420%), $C^{13}\ O^{16}\ O^{16}$ (1.108%), $C^{12}\ O^{16}\ O^{18}$ (0.408%) and $C^{12}\ O^{16}\ O^{17}$ (0.065%). Transmittance (or absorption) of $CO_2$ is dependent on the amount of $CO_2$, total pressure and the temperature. Experimental measurements of absorption are usually made with $CO_2$ mixed with a second gas such as $N_2$. Corrections are necessary when application is made to the atmosphere for two reasons. Partial pressures of $CO_2$ used are not usually in agreement with the mixing ratio of $CO_2$ in the atmosphere, and pressure broadening of individual spectral lines is different for gases such as $O_2$ and $N_2$ compared to $CO_2$ with itself. Effects of different broadening agents have been investigated by Burch et al. (1962a) and Reichle (1969).

Low resolution measurements of total absorption as a function of $CO_2$ amount and pressure were reported by Howard et al. (1956) and Burch et al. (1962b). Figure A.1 taken from Burch et al. (1962b) shows an example of the low resolution data. High resolution spectral data were obtained by Madden (1961) from 15μ to 18μ. Total intensity of all bands in the 15μ region is probably best represented by Wolk (1967).

Transmittance of water vapor has been reported by Palmer (1957) for the spectral region 20μ (500 $cm^{-1}$) to

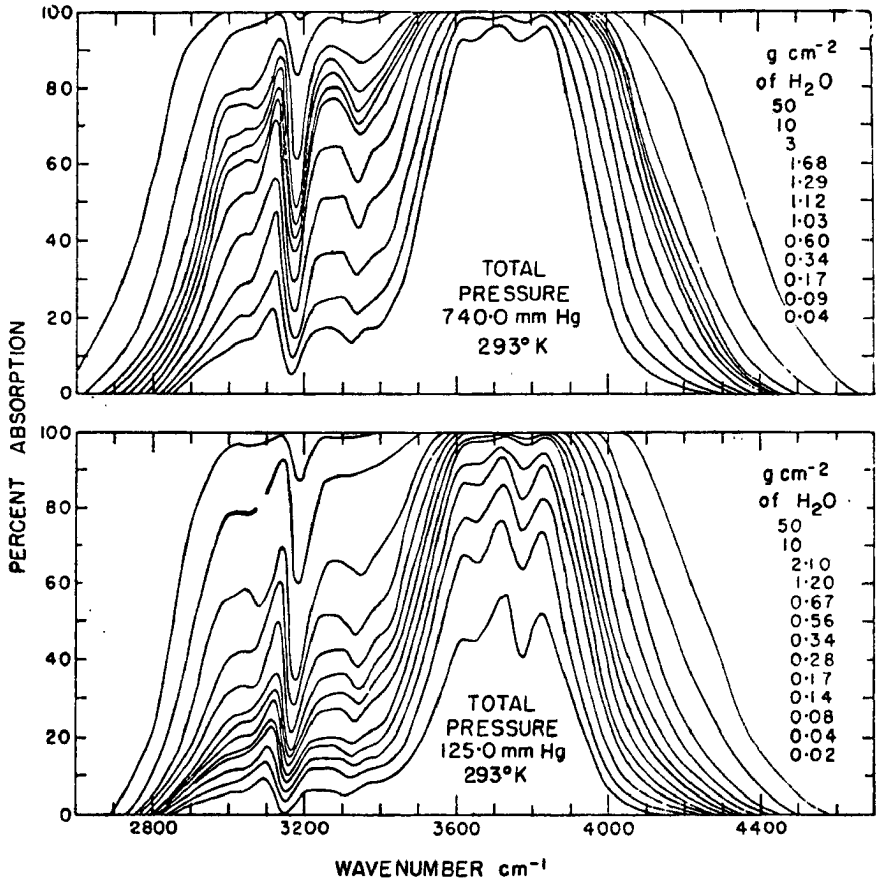


Figure A.1 Low resolution spectra of 15μ $CO_2$ bands from Burch et al. (1962b).

31.7μ (315.46) with a resolution of 3 $cm^{-1}$ to 4 $cm^{-1}$ and for the region 29μ (344.83) to 40μ (250 $cm^{-1}$) with a resolution of 5 $cm^{-1}$ to 8 $cm^{-1}$ (Figure A.2). Stauffer and Walsh (1966) made measurements in spectral intervals 55 $cm^{-1}$ wide from 495 $cm^{-1}$ to 715 $cm^{-1}$.

Theoretical Models

Exact theoretical calculations of transmittance of $CO_2$ and $H_2O$ are possible if all line positions, strengths, shapes, and widths are known. Even with such information the computing time on large digital computers for an integration across the spectrum for a given gas mixing ratio, pressure, and temperature is lengthy and often not feasible in many applications. Because of the lack of necessary information for many years and the computer difficulties, several approaches (band models) have been developed to calculate transmittance in the atmosphere. Examples of some of the important steps taken in model development and included in the present discussion are Lorentz and Doppler line shapes, the Elsasser model, the Goody statistical model, the quasi-random model, and direct line by line calculations.

The shape of an individual spectral line is an important factor for transmittance calculations. The pressure broadened line shape often called the Lorentz line was (Goody, 1964)

$$k_\nu = \frac{\alpha}{\pi[(\nu-\bar{\nu})^2 + \alpha^2]} \qquad (A.1)$$

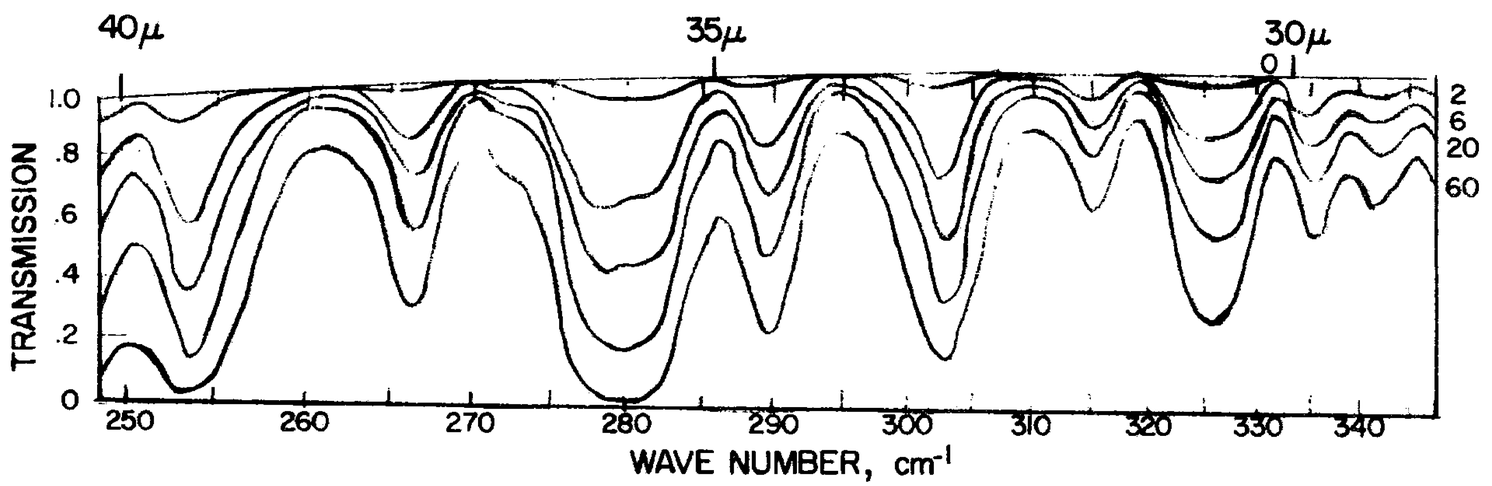


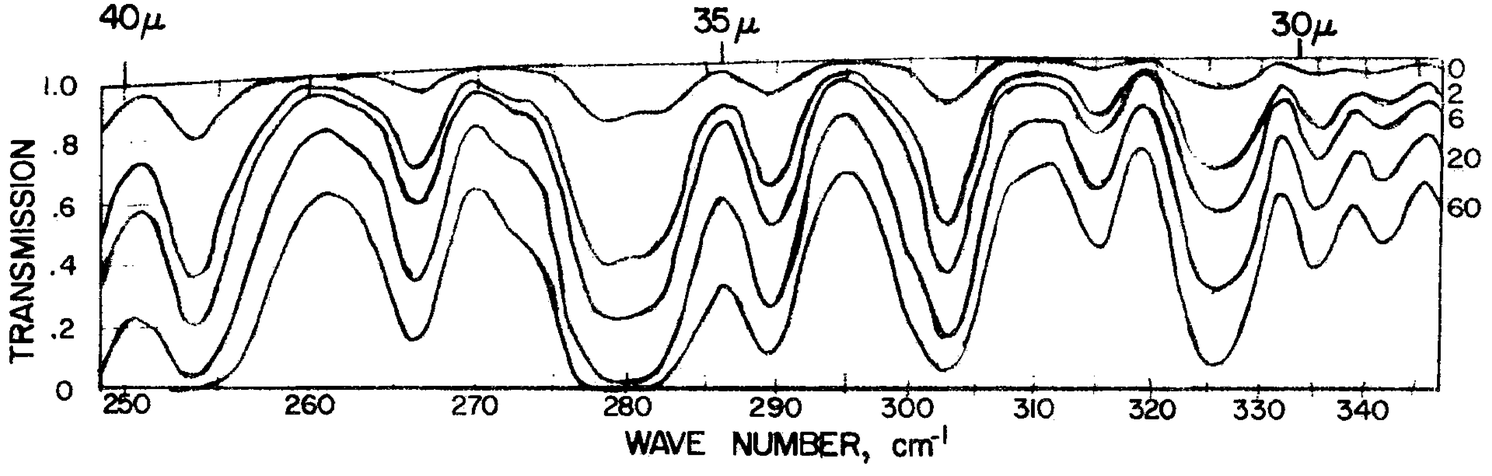


Figure A.2 Spectra of water vapor rotation bands from Palmer (1957) with 6 gm water vapor (upper) and 12 gm water vapor (lower) and nitrogen partial pressure in cm Hg.

where the half-width is directly proportional to pressure and inversely proportional to the square root of the temperature. This pressure broadening is caused by the collisions between molecules. Natural broadening due to uncertainty of the energy of a given molecule in a given energy state has the same form as equation (A.1), but the half-width is much less and essentially negligible for atmospheric problems.

A second type of line broadening important in atmospheric studies is Doppler broadening which is due to the velocity of the radiating molecules toward or away from the direction of interest. The Doppler line shape is (Goody, 1964)

$$k_\nu = \frac{1}{\alpha_D \sqrt{\pi}} \exp - \left(\frac{\nu-\bar{\nu}}{\alpha_D}\right)^2 \qquad (A.2)$$

where the half-width is proportional to the square root of temperature. A comparison of the two line shapes is given in Figure A.3 from Goody (1964) for lines of equal intensity and half-width. The primary difference is the large absorption of the Doppler line in the center of the interval followed by a very sharp decrease with frequency away from the center. Since the half-width of the Lorentz line is linearly dependent on pressure, the Doppler line becomes more important at higher attitudes. This results in a situation in which the Doppler line is more important in determining absorption near the line center and the Lorentz line more important far from the line center.

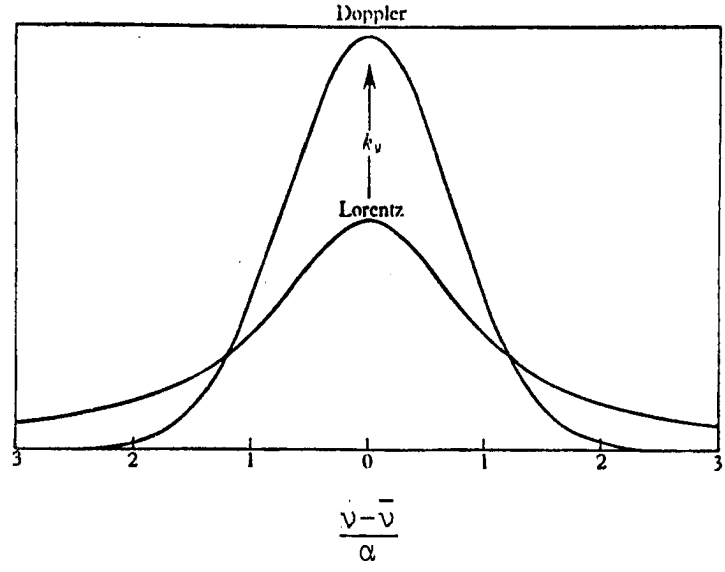


Figure A.3 Doppler and Lorentz line shapes for similar intensities and line widths from Goody (1964).

Transmittance values over a wider spectral region encompassing many lines, a band, or several bands is required for many atmospheric problems. The Elsasser model (Elsasser, 1942) assumes an infinite array of lines of equal intensity spaced at equal intervals of frequency. Absorption for this model has been solved for the Lorentz, pressure-broadened line and results in an integral expression which must be evaluated numerically.

The Goody statistical model assumes a given number of lines of unequal intensity distributed randomly in a specified spectral interval (Goody, 1952). Absorption for lines of equal half-width but an exponential intensity distribution yield results similar to the Elsasser model for small amounts of gas with no overlapping of lines. Elsasser and Culbertson (1960) have used the Goody statistical model to argue that transmittance is approximately a function of one parameter which varies only with wavelength multiplied by another parameter which is a function of the amount of absorber modified for pressure and temperature effects. Elsasser and Culbertson (1960) then determined a wavelength dependent parameter, the generalized absorption coefficient, for the 15μ $CO_2$ region and the rotational water bands.

Plass (1958) has compared the Elsasser and Goody statistical models. For small amounts of absorber with little or no overlap of lines the models agree quite well. For considerable overlap and large amounts of absorber the uniformly

spaced lines (Elsasser) yield a more rapid approach to complete absorption than the randomly spaced lines.

A quasi-random model has been developed by Wyatt et al. (1962). This model divides the spectral interval of interest into an arbitrary number of smaller intervals of width $\delta$. Positions of the individual lines within each $\delta$ are random but the number of lines in each $\delta$ are specified. Absorption from each $\delta$ interval contributes to all other $\delta$ intervals. Absorption in each $\delta$ interval is calculated using the statistical model and an analytic expression for spectral line shape. The line shape used is the Benedict modification of the Lorentz line which has a frequency dependent exponential factor multiplying the Lorentz shape to produce a more rapid decrease of absorption with distance from the line center. Stull et al. (1962) have used the quasi-random model to calculate transmittance for the 15$\mu$ region of $CO_2$ over a wide range of pressure and absorber amounts. A brief description is given in Stull et al. (1964).

Calculation of transmittance by direct integration across a spectral interval is possible as mentioned previously when line widths, shape, position, and intensity are known for each line. Drayson (1966) and Kunde (1967) have performed such a computation for the 15$\mu$ region of $CO_2$. This technique is not really a model but is instead an exceptionally detailed and theoretically sound computation. No such computation has yet been reported for rotational water vapor bands.

Slant Path Transmittance

All of the experimental measurements of transmittance have been for conditions of constant pressure and temperature throughout the gas. Applications to the earth's atmosphere which involve radiation from various heights necessarily have large pressure variations and lesser temperature variations along the path. The Elsasser, statistical, and quasi-random models require an equivalent pressure and temperature for a path in order to calculate transmittance. The Curtis (1952)-Godson (1953) approximation for effective pressure and temperature has been used extensively. Effective pressure and temperature are defined by

$$p_e = \frac{\int p\,du}{\int du} \text{ and } T_e = \frac{\int T\,du}{\int du} . \qquad (A.3)$$

These quantities are mass weighted averages over the path. Drayson (1966) has computed transmittance by the direct integration method with and without using the Curtis-Godson approximation for carbon dioxide to illustrate the effect. For a path with pressure variation from 10 mb to 100 mb the maximum error was about 3 per cent in transmittance which occurs for intermediate values of the product of line strength and absorber amount. Errors approach zero for very small or large values of the product.

Models Used in the Present Study

The present study makes use of the model which Bates et al. (1967) have developed to calculate limb radiance for the 15μ region of $CO_2$. Transmittance is determined from

calculated transmittances of Stull et al. (1962) and Plass (1963). Spectral resolution of transmittance is 5 $cm^{-1}$. Both sources were necessary for an ample range of absorber amounts and pressures encountered with long path lengths in the stratosphere. To save computer time the tabulated transmittances were curve fitted over the desired range of optical path and pressures. The form of the curve fit is

$$\tau_\nu = \exp\{ - \exp[C_o+C_1x+C_2x^2+C_3x^3+(A_1+B_1 \ln up_e)(T-273) + (A_2+B_2 \ln up_e)(T-273)^2]\} . \quad (A.4)$$

Equation A.4 provides an extrapolation of transmittance as a function of temperature from 200° K to 150° K since the data sources did not cover the range even though temperatures less than 200° K are not uncommon in the stratosphere. The Curtis-Godson approximation is used for effective pressure and temperature.

Doppler broadening must be included in $CO_2$ transmittance since the Doppler and Lorentz half-widths are equal at about 33 km altitude at 15μ. Bates et al. (1967) have used a mixed line shape often denoted the Voigt line to determine the transmittance variation from the Lorentz line and then developed a correction factor which is a multiplication correction to the transmittance from a Lorentz line.

Transmittance for the rotational water vapor bands are used directly from Elsasser and Culbertson (1960). Effective

pressure and temperature are obtained with the Curtis-Godson approximation.

Transmittance of Two Gases

The 15μ region is dominated by $CO_2$ absorption; however $H_2O$ and $O_3$ contribute to the total absorption. For molecules that do not interact the transmittance for a mixture is the product of the separate transmittances

$$\tau_{c,h} = \tau_c \cdot \tau_h \ . \qquad (A.5)$$

Goody (1964) comments that this multiplicative property works quite well and it is fortunate that $CO_2$ and $H_2O$ molecules collide predominately with $N_2$ instead of with each other. Water vapor absorption is strongest at the long wavelength side of 15μ and is due to the rotational bands. Ozone absorption is due to bands near 14μ. Bates et al. (1967) have investigated the effects of $H_2O$ and $O_3$ on the transmittance for the spectral range 600 $cm^{-1}$ to 725 $cm^{-1}$. For paths through the atmosphere characterized by tangent heights (Figure 2.1) of 20 km and greater the $H_2O$ effect is negligible. Ozone produces a noticeable change of transmittance in the 700 $cm^{-1}$ to 725 $cm^{-1}$ interval of between 10 per cent and 20 per cent, but the total effect of both $O_3$ and $H_2O$ when integrated from 600 $cm^{-1}$ to 725 $cm^{-1}$ is only a maximum of 2 per cent. Consequently, the effects of $O_3$ and $H_2O$ in the 15μ region are ignored in the present investigation.

# APPENDIX B

# APPENDIX B

## PROPAGATION OF ERRORS DUE TO HORIZONTAL TEMPERATURE GRADIENTS AND RANDOM RADIANCE ERRORS

The preceding chapters have dealt with the problem of remotely determining the stratospheric temperature structure. Although description of structure is possible with suitable measurements in time and space, further understanding of atmospheric processes will require the use of inferred temperature information to calculate other important quantities. For large scale flow features in the stratosphere the geostrophic wind and thermal wind can be calculated from the inferred temperature data. Once these wind and wind shear quantities are available, transport of heat, kinetic energy, and angular momentum could be investigated. Time changes in the wind field and temperature field could also be useful.

In the derivation of the temperature inference technique in Chapter III the atmosphere was assumed to be spherically symmetric. Horizontal temperature gradients are thus eliminated from the technique even though normally present in the atmosphere. The effects of horizontal temperature gradients on inferred temperature, geopotential height, geostrophic wind, and wind shear have been investigated for an atmospheric structure typical of winter with rather strong horizontal temperature gradients. An initial state described below was assumed. Limb radiance profiles were calculated with and without horizontal temperature gradients included.

These radiance profiles were kindly provided by Davis (1971) based on computation technique reported by Davis (1969). Both sets of limb radiance profiles were used to infer temperature structure, height, wind, and wind shear. Differences were considered as errors due to the effects of horizontal temperature gradients.

The sensitivity of the inferred temperatures to bias, scale, and random radiance errors was illustrated in Chapter III. Bias and scale errors should be controlled to a level which causes no real difficulty. Random radiance errors should be investigated further since calculations of wind and wind shear depend on horizontal derivatives.

Random errors in radiance will not necessarily produce random errors in derived quantities. It is not evident from the example in Chapter III just how random radiance errors will propagate through the temperature inference and hydrostatic integration into the horizontal wind and wind shear. Examples of the effects of random radiance errors on temperature, height, wind, and wind shear were generated in the following manner. An initial atmospheric structure was chosen. Limb radiance profiles were calculated for a series of locations. The radiances were perturbed by adding random radiances with a mean of zero and a specified standard deviation. Both the original and perturbed radiances were used to infer temperature. Each set of temperatures were used to compute height hydrostatically. Horizontal derivatives of

the heights were used to compute wind and horizontal derivatives of temperature were used to compute wind shear.

Initial State

The initial atmospheric state chosen for the error propagation examples was a strong low pressure system centered at the north pole. The structure was an arbitrary one but is similar to a mid-winter condition with strong winds. Figures B.1 and B.2 show cross-sections of temperature and height fields from 30N to 80N. All cross-sections at constant longitude would be identical since this initial state was symmetric about the north pole. Atmospheres from 10 mb to 0.05 mb at 30N, 40N, 50N, 60N, 70N, and 80N were used to define the initial state. Horizontal temperature gradients for the initial state are presented in Table B.1 which indicates the strongest gradients are at 60N.

The spectral interval used to calculate limb radiances for the error examples was 615 $cm^{-1}$ to 715 $cm^{-1}$ and the mixing ratio of $CO_2$ was 314 parts per million by volume. Average transmittance for tangent pressures larger than 10 mb was less than 0.5. As the average transmittance approaches zero (opacity) the temperature errors due to radiance errors are increasingly dependent on the spectral interval chosen. Consequently, the error examples do not extend to tangent pressures greater than 10 mb which is near 30 km altitude.

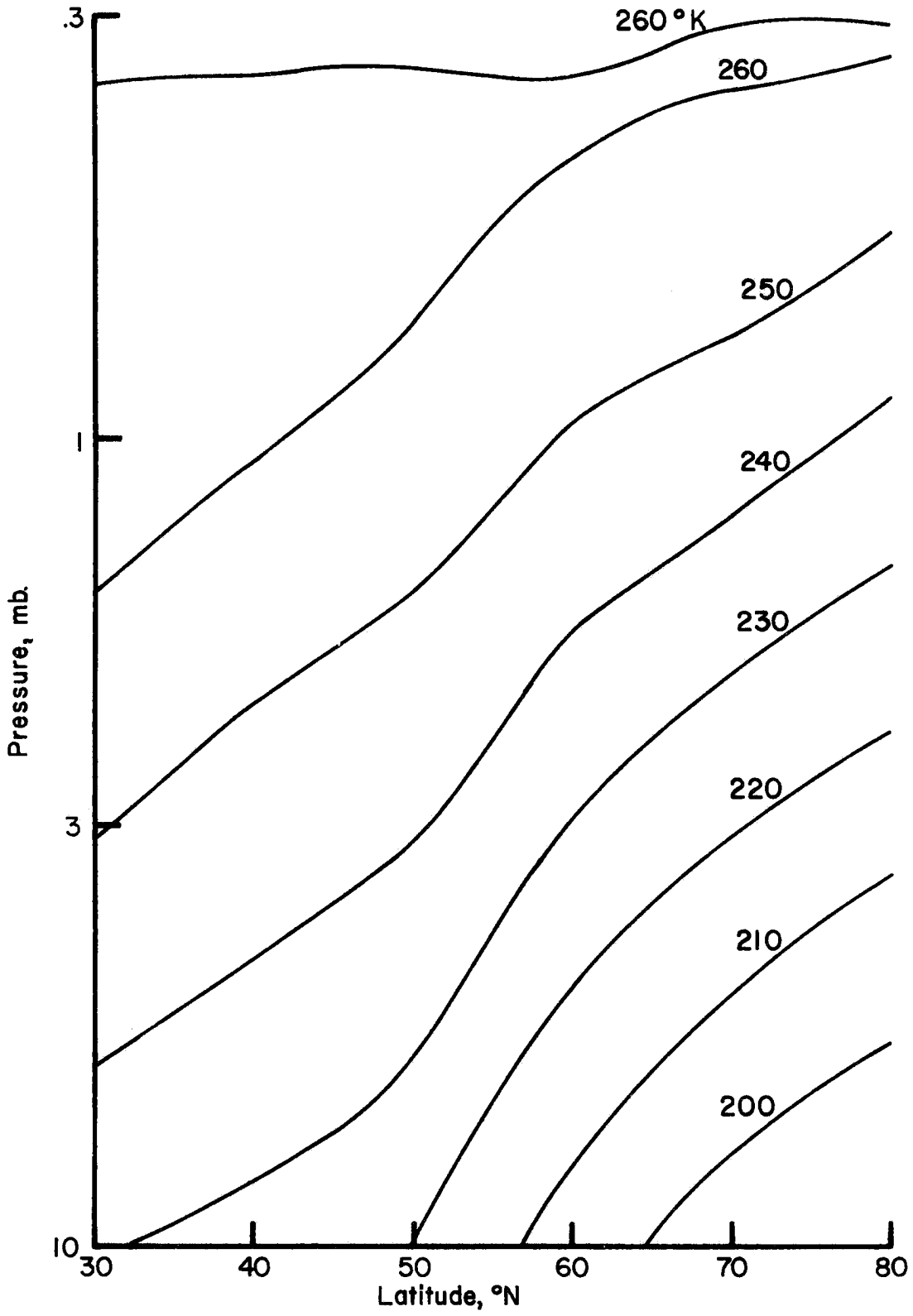


Figure B.1 Initial state temperature field.

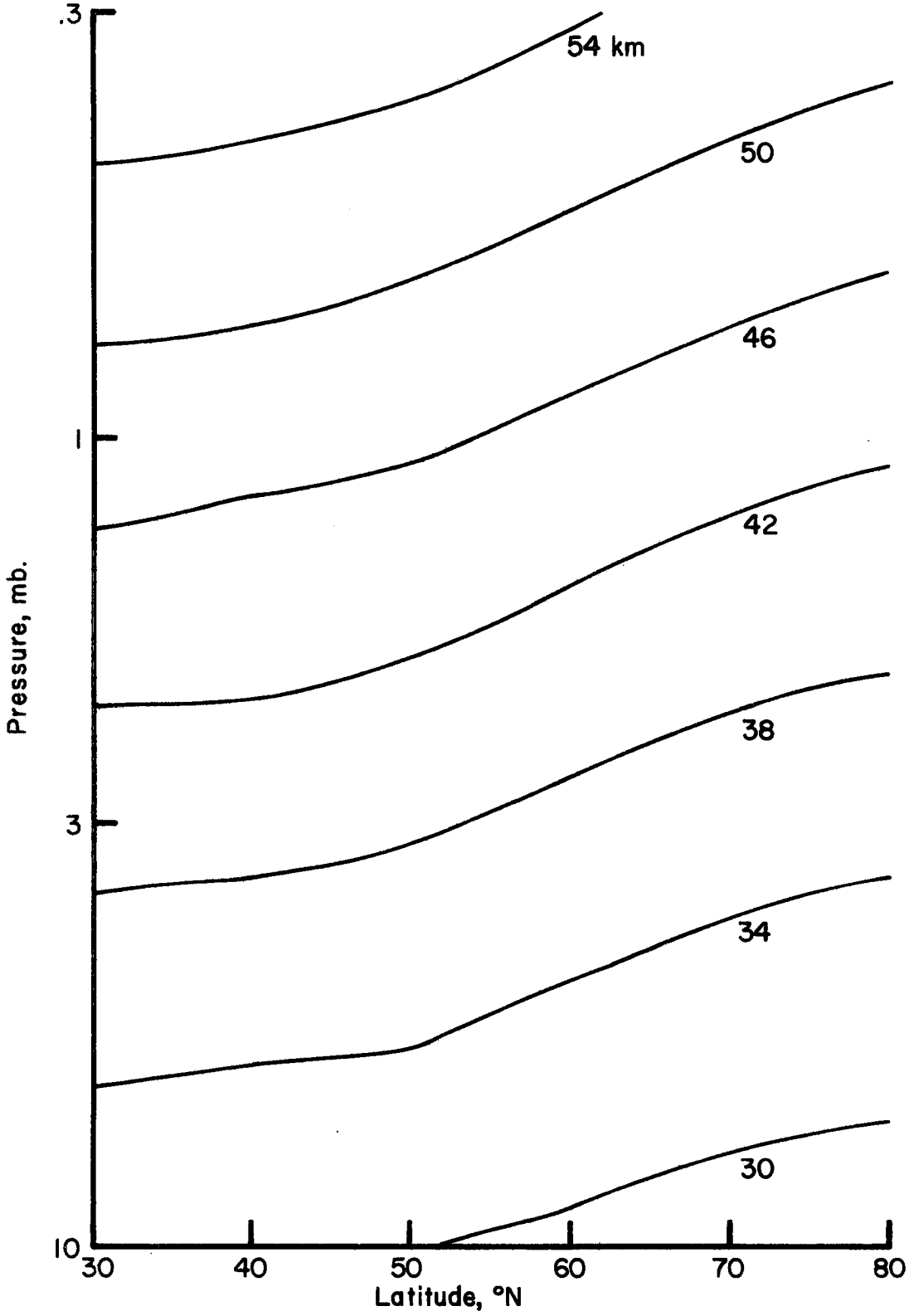


Figure B.2 Initial state height field.

Table B.1. Initial state temperature gradients.

| Pressure mb | Temperature Gradients °K deg. latitude$^{-1}$ | | | | | |
|---|---|---|---|---|---|---|
| | 30N | 40N | 50N | 60N | 70N | 80N |
| 10 | .5 | .5 | .5 | 1.5 | 1.1 | .7 |
| 9 | .4 | .4 | .6 | 1.4 | 1.1 | .7 |
| 8 | .5 | .5 | .5 | 1.4 | 1.1 | .7 |
| 7 | .5 | .5 | .5 | 1.4 | 1.0 | .7 |
| 6 | .5 | .5 | .5 | 1.3 | 1.0 | .7 |
| 5 | .5 | .5 | .5 | 1.3 | .9 | .7 |
| 4 | .5 | .5 | .5 | 1.2 | .8 | .9 |
| 3 | .5 | .5 | .5 | 1.1 | .7 | .7 |
| 2 | .6 | .6 | .4 | .9 | .7 | .7 |
| 1 | .5 | .5 | .5 | .6 | .4 | .7 |
| .8 | .2 | .2 | .4 | .6 | .4 | .6 |
| .6 | .1 | .1 | .1 | .4 | .3 | .6 |
| .4 | 0 | 0 | 0 | 0 | .1 | .1 |
| .2 | -.1 | -.1 | -.1 | 0 | -.1 | 0 |
| .1 | -.2 | -.2 | -.2 | -.2 | -.2 | -.1 |
| .05 | -.2 | -.2 | -.2 | -.2 | -.2 | -.1 |
| .01 | -.2 | -.2 | -.2 | -.2 | -.2 | -.1 |

Inferred Temperature Structure

The errors in the inferred temperature structure due to using an inference technique which doesn't account for temperature gradients are given in Table B.2. Errors are given for twenty pressure levels for each latitude. Each inference of temperature resulted in a unique set of corresponding pressures. In order to make a comparison of the results the temperatures were interpolated to a common set of pressures. The entry at 10 mb is actually an extrapolation due to inference of warmer temperatures. The interpolation was actually a smoothing process, but the pressure level spacing was small enough that the smoothing has had a small effect. The temperature inference was done for an instrument looking to the north which means the emitting gas from the tangent point toward the observer was warmer than that at the tangent point for tangent pressure of 10 mb to less than 1 mb and was colder at the smallest pressures. Temperature errors were positive for most of the pressure range with a few negative values at the small pressure. The average temperature errors given in Table B.2 range from 1.3° K to 2.4° K. The largest temperature errors were about 4° K associated with a 1.1° K deg.$^{-1}$ gradient near 3 mb. Sensitivity to the gradients was not uniform with tangent pressure as larger gradients such as 1.4° K deg.$^{-1}$ at about 7 mb produce only a 2° K error. The decrease in error was due to the fact that as the percentage of total radiance contributed by the tangent layer decreases the warmer temperatures at

Table B.2. Temperature errors due to horizontal temperature gradients.

| Pressure mb | Temperature Error °K | | | | | |
|---|---|---|---|---|---|---|
| | 30N | 40N | 50N | 60N | 70N | 80N |
| 10.0000 | 1.0 | 1.0 | 1.0 | 1.0 | 1.0 | 1.0 |
| 8.1873 | .8 | 1.1 | 1.3 | 1.0 | .6 | .8 |
| 6.7032 | 1.2 | 1.2 | 1.3 | 2.2 | 1.4 | 1.3 |
| 5.4881 | 1.4 | 1.4 | 1.4 | 3.0 | 2.0 | 1.5 |
| 4.4933 | 1.7 | 1.6 | 1.6 | 3.5 | 2.2 | 2.5 |
| 3.6788 | 2.0 | 1.7 | 1.7 | 3.7 | 2.4 | 2.8 |
| 3.0120 | 2.0 | 2.2 | 1.9 | 4.3 | 2.3 | 2.7 |
| 2.4660 | 2.3 | 2.6 | 1.7 | 3.8 | 2.7 | 3.0 |
| 2.0190 | 2.5 | 2.5 | 2.2 | 3.5 | 2.9 | 3.3 |
| 1.6530 | 2.6 | 2.6 | 1.9 | 3.4 | 2.8 | 3.5 |
| 1.3534 | 2.4 | 2.3 | 2.1 | 3.2 | 2.4 | 3.6 |
| 1.1080 | 2.3 | 2.3 | 2.3 | 3.4 | 2.0 | 3.5 |
| 1.0026 | 2.2 | 2.3 | 2.4 | 2.9 | 2.2 | 3.4 |
| .9072 | 1.6 | 2.1 | 2.4 | 2.8 | 2.3 | 3.1 |
| .7427 | 1.1 | 1.0 | 1.6 | 2.6 | 1.7 | 2.5 |
| .6081 | .7 | .6 | .8 | 2.0 | 1.6 | 3.0 |
| .4979 | 0.0 | .3 | .6 | 1.7 | 1.4 | 2.1 |
| .4076 | - .2 | .1 | - .1 | 0.0 | .6 | .6 |
| .3337 | - .5 | - .8 | .1 | - .2 | .3 | - .6 |
| .3020 | - .6 | - .5 | - .3 | - .2 | - .1 | - .7 |
| Mean | 1.3 | 1.4 | 1.4 | 2.4 | 1.7 | 2.1 |

smaller pressures were accounting for the radiance error to a larger extent. Consequently, the increase of temperature with height from 10 mb to 5 mb was made to appear larger than actual. The magnitude of the change of lapse rate would depend on the temperature gradients, the spectral interval, and the tangent pressure.

A summary of the inferred temperature structure with random radiance errors is given in Table B.3 and B.4. Table B.3 gives the temperature error from the initial state due to a random radiance error of mean equal to zero and a standard deviation of 0.01 W $m^{-2}$ $sr^{-1}$. Means for the temperature errors were all less than 1° K. Standard deviations were strongly affected by extreme points as was evident at 80N where the single largest error of 11.2° K occurred. Table B.4 gives the mean and standard deviation of the temperature errors at each level for latitudes 50N and 60N based on twenty sets of random radiance errors for each latitude. The standard deviations indicate a significant change with tangent pressure. Temperature errors tend to be smaller at larger tangent pressures since the radiance error was a smaller fraction of the total radiance and the radiance from the thin layer at the tangent point was a larger fraction of the total radiance. This tendency would be reversed at yet larger tangent pressures as the atmosphere becomes opaque and the radiance emitted near the tangent point which escapes the top of the atmosphere tends to zero.

Table B.3. Temperature error due to random radiance error of $\sigma$ = .01 W $m^{-2}$ $sr^{-1}$.

| Pressure mb | Temperature Error °K | | | | | |
|---|---|---|---|---|---|---|
| | 30N | 40N | 50N | 60N | 70N | 80N |
| 10.0000 | -1.0 | 0.5 | 0.5 | 1.0 | 0.0 | 0.5 |
| 8.1873 | 0.1 | 0.9 | -0.2 | 1.2 | 0.1 | -0.6 |
| 6.7032 | 0.0 | 0.4 | 0.2 | 1.0 | 0.8 | 0.6 |
| 5.4881 | 0.2 | 0.2 | 0.8 | 1.1 | 1.6 | 0.1 |
| 4.4933 | -0.2 | 1.0 | -0.2 | -0.7 | -1.2 | -0.9 |
| 3.6788 | -0.7 | -0.5 | 0.4 | 1.1 | 0.8 | 1.3 |
| 3.0120 | 0.2 | 1.6 | 1.3 | 1.1 | 0.8 | 1.2 |
| 2.4600 | -0.5 | 1.7 | 0.1 | -0.3 | -1.0 | -0.9 |
| 2.0190 | -0.3 | 0.2 | 0.3 | 0.7 | -0.1 | 1.0 |
| 1.6530 | -0.5 | 1.1 | 0.8 | 0.5 | 0.4 | 1.6 |
| 1.3534 | -0.3 | 1.2 | -0.8 | -0.8 | -1.7 | -1.0 |
| 1.1080 | 2.6 | -0.4 | 1.0 | 1.2 | -0.1 | 0.6 |
| 1.0026 | -3.2 | 0.9 | 1.8 | 1.5 | 0.8 | 1.8 |
| .9072 | -1.0 | 2.0 | 1.7 | -0.5 | 0.1 | 2.3 |
| .7427 | 1.9 | -0.5 | 0.3 | 1.0 | -0.9 | -0.3 |
| .6081 | -1.7 | 1.5 | 0.7 | 1.1 | -0.3 | 0.8 |
| .4979 | 0.2 | 1.0 | 1.6 | 2.8 | -1.5 | 0.3 |
| .4076 | -0.7 | 5.9 | 7.8 | 0.9 | 5.1 | 11.2 |
| .3337 | 0.7 | -3.3 | -1.3 | -0.1 | -3.5 | -1.8 |
| .3020 | 1.5 | 0.9 | 1.7 | 2.2 | 1.3 | 0.3 |
| Mean | -0.14 | 0.82 | 0.93 | 0.80 | 0.08 | 0.91 |
| $\sigma$ | 1.22 | 1.62 | 1.86 | 0.89 | 1.64 | 2.57 |

Table B.4. Mean and standard deviation of temperature errors at 50N and 60N for $\sigma$ = .01 W $m^{-2}$ $sr^{-1}$.

| Pressure mb | 50N | | 60N | |
|---|---|---|---|---|
| | Mean °K | S.D. °K | Mean °K | S.D. °K |
| 10.0000 | .31 | .76 | .09 | 1.08 |
| 8.1873 | .12 | .38 | .07 | .57 |
| 6.7032 | - .05 | .62 | .18 | .58 |
| 5.4881 | - .19 | .58 | .08 | .58 |
| 4.4933 | .17 | .51 | .02 | .55 |
| 3.6788 | .07 | .80 | .36 | .89 |
| 3.0120 | .02 | .58 | - .15 | .94 |
| 2.4660 | - .25 | .87 | .24 | .78 |
| 2.0190 | .04 | .87 | .08 | .90 |
| 1.6530 | .55 | .64 | - .34 | 1.00 |
| 1.3534 | .20 | 1.23 | .05 | 1.87 |
| 1.1080 | - .05 | 1.63 | .18 | 1.36 |
| 1.0026 | - .24 | 1.10 | - .38 | 1.51 |
| .9072 | - .34 | 1.08 | .27 | 1.68 |
| .7427 | .84 | 2.46 | - .14 | 2.10 |
| .6081 | - .45 | 1.94 | - .44 | 2.53 |
| .4979 | - .95 | 2.92 | -1.16 | 2.66 |
| .4076 | - .50 | 2.56 | .75 | 3.75 |
| .3337 | 2.03 | 5.36 | .83 | 3.62 |
| .3020 | 1.13 | 3.62 | .53 | 4.86 |

Table B.5. Height errors due to horizontal temperature gradients.

| Pressure mb | Height Error Meters | | | | | |
|---|---|---|---|---|---|---|
| | 30N | 40N | 50N | 60N | 70N | 80N |
| 10.0000 | 0 | 0 | 0 | 0 | 0 | 0 |
| 8.1873 | 6 | 6 | 7 | 6 | 2 | 4 |
| 6.7032 | 12 | 13 | 15 | 17 | 11 | 12 |
| 5.4881 | 20 | 21 | 22 | 31 | 19 | 21 |
| 4.4933 | 29 | 30 | 32 | 51 | 32 | 33 |
| 3.6788 | 41 | 40 | 42 | 74 | 47 | 50 |
| 3.0120 | 52 | 51 | 53 | 96 | 62 | 64 |
| 2.4660 | 66 | 67 | 64 | 121 | 76 | 82 |
| 2.0190 | 80 | 82 | 76 | 143 | 93 | 101 |
| 1.6530 | 96 | 98 | 88 | 163 | 111 | 120 |
| 1.3534 | 111 | 112 | 99 | 183 | 125 | 142 |
| 1.1080 | 125 | 126 | 113 | 203 | 139 | 164 |
| 1.0026 | 132 | 133 | 120 | 212 | 145 | 174 |
| .9072 | 137 | 140 | 127 | 221 | 152 | 183 |
| .7427 | 145 | 149 | 140 | 237 | 164 | 202 |
| .6081 | 150 | 153 | 146 | 251 | 174 | 222 |
| .4979 | 152 | 156 | 150 | 262 | 182 | 236 |
| .4076 | 152 | 157 | 151 | 268 | 188 | 245 |
| .3337 | 149 | 156 | 151 | 267 | 191 | 245 |
| .3020 | 148 | 155 | 151 | 266 | 191 | 243 |
| Mean | 90 | 92 | 87 | 154 | 105 | 127 |

Inferred Height Structure

The errors in geopotential height due to horizontal temperature gradients are shown in Table B.5. Height was calculated by integration of the hydrostatic equation starting at 10 mb where the heights were assumed to be known. All height errors were positive with the largest height errors at 60N resulting from the largest temperature errors at 60N. Height errors increased as the pressure decreased because the temperature errors were of the same sign with the exception of the last two layers.

The errors in the height field due to random radiance errors are shown in Table B.6. Examination of Table B.6 reveals that height errors at one latitude may be all positive, all negative, or a mixture. The cases of all errors being of the same sign were caused by a few successive temperature errors of one sign which through the integration forced the height errors to get large enough that other errors could change the amplitude of the height error but not its sign. The random nature of the radiance error has been completely removed in the height errors.

Inferred Geostrophic Wind

Symmetry of the initial state caused the north-south component of the geostrophic wind to be zero. The east-west component, u, with the convergence of the meridians accounted for is (Haltner and Martin, 1957)

$$\frac{u^2 \tan\phi}{r} + fu + g\frac{\partial z}{\partial y} = o \qquad \text{(B.1)}$$

Table B.6. Height error due to random radiance error of $\sigma = .01$ W $m^{-2}$ $sr^{-1}$.

| Pressure mb | Height Error Meters | | | | | |
|---|---|---|---|---|---|---|
| | 30N | 40N | 50N | 60N | 70N | 80N |
| 10.0000 | 0 | 0 | 0 | 0 | 0 | 0 |
| 8.1873 | - 5 | 3 | 0 | 7 | 1 | 0 |
| 6.7032 | - 4 | 6 | 2 | 13 | 4 | - 1 |
| 5.4881 | - 3 | 10 | 3 | 17 | 11 | - 2 |
| 4.4933 | - 3 | 13 | 6 | 17 | 9 | - 2 |
| 3.6788 | - 6 | 16 | 5 | 18 | 8 | 0 |
| 3.0120 | - 8 | 17 | 10 | 25 | 13 | 7 |
| 2.4660 | - 6 | 28 | 16 | 26 | 12 | 6 |
| 2.0190 | - 8 | 35 | 15 | 27 | 8 | 6 |
| 1.6530 | - 11 | 39 | 19 | 31 | 9 | 12 |
| 1.3534 | - 11 | 47 | 20 | 29 | 4 | 13 |
| 1.1080 | - 10 | 47 | 20 | 29 | - 3 | 11 |
| 1.0026 | - 12 | 48 | 24 | 33 | 2 | 14 |
| .9072 | - 16 | 52 | 29 | 34 | - 1 | 19 |
| .7427 | - 4 | 61 | 30 | 33 | - 9 | 20 |
| .6081 | - 16 | 68 | 33 | 39 | - 12 | 22 |
| .4979 | - 20 | 75 | 39 | 48 | - 16 | 27 |
| .4076 | - 26 | 108 | 77 | 81 | 4 | 53 |
| .3337 | - 26 | 106 | 85 | 79 | - 2 | 67 |
| .3020 | - 23 | 104 | 87 | 80 | - 8 | 66 |
| Mean | - 12 | 42 | 26 | 33 | 2 | 17 |
| $\sigma$ | 7.8 | 33.6 | 26.4 | 22.3 | 8.0 | 20.8 |

where the last two terms are usually used for geostrophic wind. Strong winds and consideration of latitudes to 80N where $\tan\phi = 5.67$ demanded the inclusion of the first term. and the north-south distance into equation (B.1) leads to a computing equation for the geostrophic wind

$$u = \Omega r \cos\phi\{-1 + [1 - \frac{g}{\Omega^2 r^2 \sin\phi \cos\phi} \frac{\partial z}{\partial \phi}]^{1/2}\} \qquad (B.2)$$

The wind field associated with the initial atmospheric state is shown in Figure B.3 and Table B.7. A strong stratospheric jet stream was centered between 50N and 60N with maximum winds of near 100 m $sec^{-1}$ in the vicinity of the stratopause which was as high as the present example extended.

Wind errors due to the horizontal temperature gradients are shown in Table B.8. All wind errors were less than 10 per cent of the initial winds which indicates the method is useful for diagnostic studies of the wind field. The increase of temperature error from 50N to 60N produced a negative wind error for 50-60N. From 60N to 70N the temperature error decreases and the wind error changed sign to entirely positive. This effect of oscillating sign of wind error was a direct result of the temperature gradients and inference of temperature.

The errors introduced into the calculated winds due to random radiance errors are given in Table B.9. The most apparent feature of the table is the change in sign of the error from one column to the next. The reason for these changes lies in the height field which in turn depended on

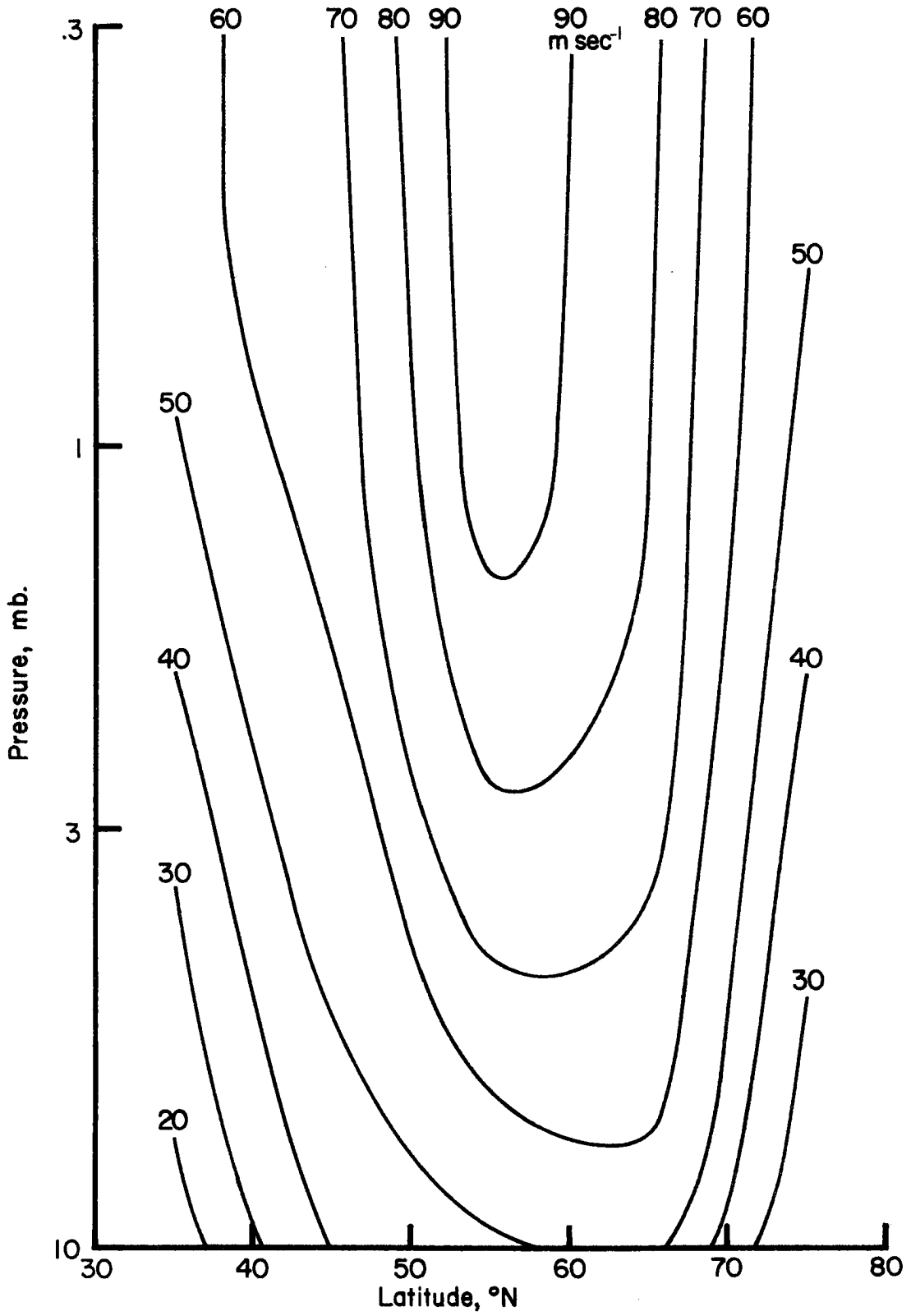


Figure B.3 Initial state wind field.

Table B.7. Wind of initial state.

| Pressure mb | Wind m $sec^{-1}$ | | | | |
|---|---|---|---|---|---|
| | 30-40N | 40-50N | 50-60N | 60-70N | 70-80N |
| 10.0000 | 16.1 | 42.2 | 48.7 | 54.7 | 22.3 |
| 8.1873 | 18.8 | 45.0 | 54.2 | 57.9 | 24.0 |
| 6.7032 | 21.6 | 47.4 | 59.6 | 61.3 | 25.9 |
| 5.4881 | 24.4 | 49.5 | 64.5 | 64.4 | 28.2 |
| 4.4933 | 27.2 | 51.7 | 69.3 | 67.1 | 30.5 |
| 3.6788 | 29.9 | 53.8 | 73.7 | 69.6 | 32.8 |
| 3.0120 | 32.9 | 55.6 | 77.9 | 71.9 | 34.9 |
| 2.4660 | 36.0 | 57.5 | 81.6 | 74.0 | 37.1 |
| 2.0190 | 39.2 | 59.2 | 85.0 | 76.0 | 39.1 |
| 1.6530 | 42.5 | 60.9 | 88.0 | 78.0 | 41.0 |
| 1.3534 | 45.7 | 62.5 | 90.8 | 79.5 | 43.0 |
| 1.1080 | 48.5 | 64.5 | 93.2 | 80.9 | 44.9 |
| 1.0026 | 49.5 | 65.4 | 94.4 | 81.4 | 45.8 |
| .9072 | 50.2 | 66.4 | 95.4 | 82.0 | 46.7 |
| .7427 | 51.8 | 67.7 | 97.3 | 83.0 | 48.4 |
| .6081 | 53.7 | 67.9 | 99.0 | 83.9 | 50.0 |
| .4979 | 54.4 | 68.1 | 100.2 | 84.6 | 51.3 |
| .4076 | 54.5 | 68.2 | 100.8 | 84.9 | 52.1 |
| .3337 | 54.3 | 68.1 | 101.0 | 84.9 | 52.4 |
| .3020 | 54.4 | 68.0 | 100.9 | 84.8 | 52.4 |

Table B.8. Wind errors due to horizontal temperature gradients

| Pressure mb | Wind Error m $sec^{-1}$ | | | | |
|---|---|---|---|---|---|
| | 30-40N | 40-50N | 50-60N | 60-70N | 70-80N |
| 10.0000 | 0.0 | 0.0 | 0.0 | 0.0 | 0.0 |
| 8.1873 | 0.0 | - .1 | 0.0 | .2 | - .1 |
| 6.7032 | - .1 | - .2 | - .1 | .3 | 0.0 |
| 5.4881 | - .1 | - .1 | - .5 | .6 | - .1 |
| 4.4933 | - .1 | - .2 | -1.1 | .9 | - .1 |
| 3.6788 | .1 | - .2 | -1.8 | 1.3 | - .1 |
| 3.0120 | .1 | - .1 | -2.4 | 1.6 | - .1 |
| 2.4660 | - .1 | .2 | -3.1 | 2.1 | - .3 |
| 2.0190 | - .2 | .4 | -3.7 | 2.4 | - .4 |
| 1.6530 | - .2 | .7 | -4.1 | 2.5 | - .4 |
| 1.3534 | - .1 | .9 | -4.5 | 2.6 | - .8 |
| 1.1080 | - .1 | .9 | -4.8 | 2.9 | -1.1 |
| 1.0026 | - .1 | .9 | -5.0 | 3.1 | -1.3 |
| .9072 | - .2 | .9 | -5.0 | 3.2 | -1.4 |
| .7427 | - .4 | .6 | -5.2 | 3.3 | -1.7 |
| .6081 | - .3 | .5 | -5.5 | 3.5 | -2.1 |
| .4979 | - .6 | .4 | -5.9 | 3.6 | -2.4 |
| .4076 | - .5 | .4 | -6.1 | 3.6 | -2.5 |
| .3337 | - .6 | .4 | -6.1 | 3.5 | -2.3 |
| .3020 | - .6 | .3 | -6.1 | 3.4 | -2.2 |
| Mean | - .2 | .3 | -3.6 | 2.2 | -1.0 |

Table B.9. Wind errors due to random radiance errors of $\sigma$ = .01 W $m^{-2}$ $sr^{-1}$.

| Pressure mb | Wind Error m $sec^{-1}$ | | | | |
|---|---|---|---|---|---|
| | 30-40N | 40-50N | 50-60N | 60-70N | 70-80N |
| 10.0000 | 0.0 | 0.0 | 0.0 | 0.0 | 0.0 |
| 8.1873 | -0.7 | 0.2 | -0.4 | 0.3 | 0.1 |
| 6.7032 | -0.9 | 0.3 | -0.6 | 0.5 | 0.2 |
| 5.4881 | -1.2 | | | | |
| 4.4933 | -1.5 | 0.0 | -0.6 | 0.4 | 0.5 |
| 3.6788 | -2.1 | 0.8 | -0.8 | 0.5 | 0.4 |
| 3.1020 | -2.4 | 0.5 | -0.7 | 0.6 | 0.3 |
| 2.4660 | -3.2 | 0.9 | -0.6 | 0.7 | 0.3 |
| 2.0190 | -4.0 | 1.4 | -0.7 | 0.9 | 0.1 |
| 1.6530 | -4.6 | 1.4 | -0.7 | 1.0 | -0.2 |
| 1.3534 | -5.3 | 1.9 | -0.5 | 1.2 | -0.4 |
| 1.1080 | -5.2 | 1.9 | -0.5 | 1.5 | -0.6 |
| 1.0026 | -5.5 | 1.7 | -0.5 | 1.6 | -0.7 |
| .9072 | -6.1 | 1.6 | -0.3 | 1.6 | -0.9 |
| .7427 | -7.3 | 2.2 | -0.1 | 1.9 | -1.3 |
| .6081 | -7.4 | 2.4 | -0.3 | 2.3 | -1.5 |
| .4979 | -8.4 | 2.5 | -0.5 | 2.9 | -1.9 |
| .4076 | -11.9 | 2.1 | -0.2 | 3.4 | -2.1 |
| .3337 | -11.8 | 1.5 | 0.4 | 3.6 | -2.2 |
| .3020 | -11.3 | 1.2 | 0.4 | 4.0 | -3.2 |
| Mean | -5.0 | 1.3 | -0.4 | 1.5 | -0.7 |
| $\sigma$ | 3.6 | 0.7 | 0.3 | 1.2 | 1.1 |

the hydrostatic integration of the temperature errors. Smallest wind errors occurred in the latitude interval with the largest winds, 50-60N, and the interval with the largest errors, 30-40N, had the next to smallest winds. Neither of these features could be anticipated and are not believed to be a general result. Errors larger than 10 per cent of the wind occurred only at small pressures for 30-40N where the largest percentage error was 18.5 per cent. Table B.10 gives the mean and standard deviation of the wind errors at each level for 50-60N based on twenty sets of random radiance errors. As indicated by the standard deviation the wind errors tended to increase as pressure decreased. This tendency was caused by the fact that the temperature errors were larger at smaller pressures coupled with the cumulative effect of the hydrostatic integration. Consequently, the result should be expected in most applications. Values of the mean wind error were small which indicate the inference of the wind should be adequate for diagnostic studies.

Inferred Wind Shear

Vertical wind shear has been derived by differentiation of equation (B.2) with respect to lnp to yield

$$\frac{\partial u}{\partial \ln p} = \frac{R}{2r\Omega \sin\phi} \frac{\partial T/\partial \phi}{\left[1 - \frac{g}{\Omega^2 r^2 \sin\phi \cos\phi}\left(\frac{\partial z}{\partial \phi}\right)\right]^{1/2}} . \qquad \text{(B.3)}$$

The wind shear of the initial wind is presented in Table B.11 and the errors in wind shear due to horizontal temperature gradients in Table B.12. The spacing of lnp in the

Table 10. Mean and standard deviation of wind errors 50-60N and $\sigma$ = .01 W $m^{-2}$ $sr^{-1}$.

| Pressure mb | Mean $m\ sec^{-1}$ | S.D. $m\ sec^{-1}$ |
|---|---|---|
| 10.0000 | 0 | 0 |
| 8.1873 | .03 | .31 |
| 6.7032 | - .04 | .41 |
| 5.4881 | - .05 | .48 |
| 4.4933 | 0 | .43 |
| 3.6788 | 0 | .47 |
| 3.0120 | - .05 | .60 |
| 2.4660 | - .05 | .76 |
| 2.0190 | - .13 | 1.03 |
| 1.6530 | - .06 | 1.16 |
| 1.3534 | .18 | 1.26 |
| 1.1080 | .05 | 1.41 |
| 1.0026 | .01 | 1.46 |
| .9072 | - .03 | 1.51 |
| .7427 | .05 | 1.66 |
| .6081 | .17 | 2.15 |
| .4979 | .34 | 2.47 |
| .4076 | .51 | 2.78 |
| .3337 | .50 | 3.47 |
| .3020 | .60 | 4.06 |

Table B.11. Wind shear of initial state.

| Pressure mb | Wind Shear m $sec^{-1}$ | | | | |
|---|---|---|---|---|---|
| | 30-40N | 40-50N | 50-60N | 60-70N | 70-80N |
| 10.0000 | -14.7 | -15.4 | -25.4 | -16.7 | - 7.7 |
| 8.1873 | -14.0 | -12.6 | -27.7 | -16.5 | - 8.7 |
| 6.7032 | -13.7 | -11.2 | -25.6 | -16.0 | -11.6 |
| 5.4881 | -14.0 | -10.7 | -24.3 | -14.7 | -11.0 |
| 4.4933 | -13.6 | -10.4 | -23.1 | -13.2 | -11.0 |
| 3.6788 | -14.6 | - 9.8 | -21.6 | -11.9 | -11.7 |
| 3.0120 | -15.2 | - 9.4 | -20.0 | -10.6 | -11.2 |
| 2.4660 | -15.8 | - 9.1 | -17.5 | -10.6 | -10.0 |
| 2.0190 | -16.2 | - 8.8 | -15.7 | -10.1 | - 9.8 |
| 1.6530 | -16.7 | - 7.6 | -14.7 | - 8.4 | -10.2 |
| 1.3534 | -15.1 | - 9.5 | -12.7 | - 7.3 | - 9.5 |
| 1.1080 | -13.3 | - 9.7 | -11.9 | - 5.9 | - 9.3 |
| 1.0026 | - 7.5 | - 9.8 | -10.5 | - 6.2 | - 9.0 |
| .9072 | - 5.4 | - 9.1 | - 9.9 | - 5.8 | - 8.8 |
| .7427 | -10.62 | - 3.9 | - 9.4 | - 4.5 | - 8.5 |
| .6081 | - 7.97 | .6 | - 7.2 | - 4.0 | - 7.3 |
| .4979 | - .9 | - 1.3 | - 4.3 | - 2.7 | - 5.5 |
| .4076 | - .2 | .3 | - 1.8 | - .8 | - 2.4 |
| .3337 | 1.6 | .4 | - .2 | 1.0 | - .4 |
| .3020 | - 2.6 | 1.7 | .9 | .3 | - .2 |

Table B.12. Wind shear error due to horizontal temperature gradients.

| Pressure mb | Wind Shear Error m $sec^{-1}$ | | | | |
|---|---|---|---|---|---|
| | 30-40N | 40-50N | 50-60N | 60-70N | 70-80N |
| 10.0000 | 0.0 | 0.0 | 0.0 | 0.0 | 0.0 |
| 8.1873 | .8 | .6 | - .6 | - .6 | .3 |
| 6.7032 | - .1 | .2 | 1.7 | -1.2 | - .1 |
| 5.4881 | 0.0 | - .1 | 2.8 | -1.5 | - .7 |
| 4.4933 | - .2 | 0.0 | 3.1 | -1.8 | .3 |
| 3.6788 | - .8 | .1 | 3.2 | -1.8 | .6 |
| 3.0120 | .7 | - .8 | 3.8 | -2.7 | .5 |
| 2.4660 | .9 | -1.9 | 3.3 | -1.6 | .4 |
| 2.0190 | - .1 | - .8 | 2.1 | - .7 | .4 |
| 1.6530 | - .1 | -1.6 | 2.3 | - .7 | .9 |
| 1.3534 | - .3 | - .3 | 1.6 | -1.0 | 1.6 |
| 1.1080 | .1 | 0.0 | 1.6 | -1.9 | 2.0 |
| 1.0026 | .2 | .2 | .7 | -1.0 | 1.5 |
| .9072 | 1.4 | .6 | .4 | - .6 | 1.0 |
| .7427 | - .3 | 1.3 | 1.5 | -1.1 | 2.2 |
| .6081 | - .3 | .3 | 1.9 | - .4 | 1.6 |
| .4979 | .9 | .5 | 1.7 | 1 .4 | .9 |
| .4076 | .9 | - .3 | .1 | .7 | 0.0 |
| .3337 | - .9 | 1.8 | - .4 | .6 | -1.1 |
| .3020 | - .3 | .6 | .1 | .2 | - .9 |
| Mean | .2 | 0.0 | 1.5 | - .9 | .6 |

tables is very close to a height difference of 1 km. Wind shear errors depend on the horizontal derivative of temperature of the inferred atmosphere and many changes in sign are apparent. Locations where the initial wind shear was small have errors of the same magnitude as the shear itself. Regions of large initial shear have errors approaching 20 per cent of initial shear.

Errors in wind shear due to random radiance errors are given in Table B.13. Wind shear errors at small pressures were often larger than the original wind shear. In the present example the temperature errors at small pressures were often larger than the horizontal temperature gradient through 10 degrees of latitude which caused the large wind shear errors. At larger pressures the temperature errors were smaller and the horizontal temperature gradients larger which produced wind shear errors considerably smaller than the initial wind shear. Inference of wind shear does not appear attractive with the errors indicated.

Table B.13. Vertical wind shear error for random radiance error of $\sigma = 0.01$ W $m^{-2}$ $sr^{-1}$.

| Pressure mb | Wind Shear Error m $sec^{-1}$ | | | | |
|---|---|---|---|---|---|
| | 30-40N | 40-50N | 50-60N | 60-70N | 70-80N |
| 10.0000 | 4.4 | 0.0 | 0.9 | -1.6 | 0.7 |
| 8.1873 | 2.3 | -2.3 | 2.4 | -1.6 | -1.0 |
| 6.7032 | 1.1 | -0.2 | 1.2 | -0.2 | -0.3 |
| 5.4881 | -0.2 | 1.3 | 0.4 | 0.8 | -2.2 |
| 4.4933 | 3.5 | -2.8 | -0.9 | -0.6 | 0.5 |
| 3.6788 | 0.5 | 1.9 | 1.1 | -0.4 | 0.7 |
| 3.0120 | 3.7 | -0.7 | -0.3 | -0.5 | 0.6 |
| 2.4660 | 6.0 | | | | |
| 2.0190 | 1.3 | -0.3 | 0.5 | -1.0 | 1.4 |
| 1.6530 | 4.0 | -0.5 | -0.6 | -0.1 | 1.6 |
| 1.3534 | 3.8 | -3.9 | -0.2 | -1.2 | 0.8 |
| 1.1080 | -8.2 | 2.9 | 0.2 | -1.7 | 0.9 |
| 1.0026 | 10.8 | 1.9 | -0.4 | -1.0 | 1.2 |
| .9072 | 8.0 | -0.6 | -3.5 | 0.6 | 3.1 |
| .7427 | -6.7 | 1.6 | 1.1 | -2.4 | 0.6 |
| .6081 | 8.4 | -1.7 | 0.7 | -1.9 | 1.4 |
| .4979 | 2.1 | 1.3 | 1.9 | -6.8 | 2.4 |
| .4076 | 17.9 | 3.9 | -10.8 | 5.6 | 7.8 |
| .3337 | -10.8 | 4.0 | 1.9 | -4.6 | 2.2 |
| .3020 | -1.9 | 1.7 | 0.8 | -4.7 | 2.1 |